Two-Phase CFD Simulation of Turbulent Gas-Driven Liquid Film Flows on Heated Walls

Zweiphasige CFD-Simulation turbulenter gas-getriebener Flüssigkeitsfilme auf beheizten Wänden

Zur Erlangung des akademischen Grades Doktor-Ingenieur (Dr.-Ing.)
genehmigte Dissertation von M.Sc. Jagannath Rao Marati

February 2016 — Darmstadt — D 17

TECHNISCHE UNIVERSITÄT DARMSTADT

Technische Thermodynamik

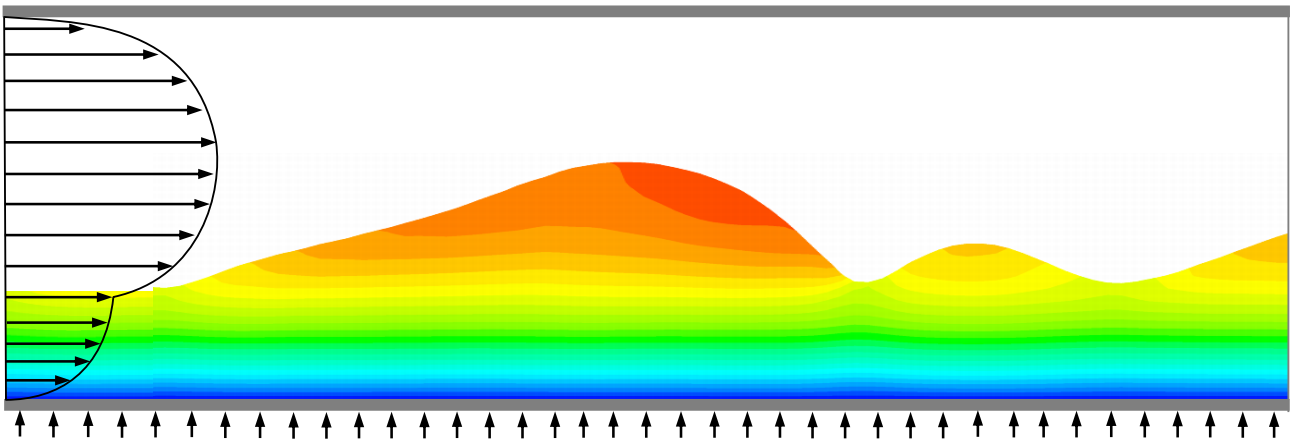

Two-Phase CFD Simulation of Turbulent Gas-Driven Liquid Film Flows on Heated Walls

Zweiphasige CFD-Simulation turbulenter gas-getriebener Flüssigkeitsfilme auf beheizten Wänden

Vom Fachbereich Maschinenbau
an der Technischen Universität Darmstadt
zur
Erlangung des akademischen Grades eines Doktor-Ingenieur (Dr.-Ing.)
genehmigte

D i s s e r t a t i o n

vorgelegt von

M. Sc. Jagannath Rao Marati
aus Medak/Indien

Berichterstatterin:	Apl. Prof. Dr. Sc. Tatiana Gambaryan-Roisman
1. Mitberichterstatter:	Prof. Dr.-Ing. Peter Stephan
2. Mitberichterstatter:	Prof. Dr.-Ing. Cameron Tropea
Tag der Einreichung:	04.08.2015
Tag der mündliche Prüfung:	04.11.2015

Darmstadt 2016

D17

Imagination is more important than knowledge. Knowledge is limited.
Imagination encircles the world.

- Albert Einstein

Erklärung zur Dissertation

Hiermit versichere ich, die vorliegende Dissertation ohne Hilfe Dritter nur mit den angegebenen Quellen und Hilfsmitteln angefertigt zu haben. Alle Stellen, die aus Quellen entnommen wurden, sind als solche kenntlich gemacht. Diese Arbeit hat in gleicher oder ähnlicher Form noch keiner Prüfungsbehörde vorgelegen.

Dortmund, den 4. August 2015

(Jagannath Rao Marati)

Acknowledgements

This doctoral thesis was carried out at the Institute of Technical Thermodynamics (TTD) in the Department of Mechanical Engineering, Technische Universität Darmstadt, Germany. The project was financially supported by the Deutsche Forschungsgemeinschaft (DFG, German Research Foundation) and Sonderforschungsbereich-568 (Flow and Combustion in Advanced Gas Turbine Combustors). I want to thank the DFG for the financial support.

I would like to begin by expressing my gratitude to my guide Prof. Dr. -Ing. Peter Stephan for providing me the opportunity to pursue my Ph.D and for his technical support throughout this work. Learning from him has been extremely satisfying, as he provided much guidance and constructive feedback during this research project. Further, I would like to acknowledge and thank Apl. Prof. Dr. Sc. Tatiana Gambaryan-Roisman for her supervision from the early stages of this thesis and her technical suggestions during my dissertation work. She guided me through all aspects of scientific research, from physical concepts through numerical methods and scientific writing. I am especially thankful to Prof. Dr.-Ing. Cameron Tropea, head of the Institute of Fluid Mechanics and Aerodynamics, Technische Universität Darmstadt, for agreeing to examine my thesis. It is also my pleasure to thank Dr. Frank Dammel and Gaby who have helped me during academic work at TTD.

Additional thanks goes toward my colleague and good friend Mete for having worked on the experimental part, as well as providing measurement data for this research. I also thank my friend Nitin for providing valuable suggestions and helpful discussions during my research work. At the beginning of this project, it was Hongy Yu, who motivated and guided my work with OpenFOAM in right directions. I wish to express my gratitude to Su Bo for assisting me in several ways during my stay in Darmstadt. Many thanks for all TTD employees for their encouragement and friendship. Furthermore, special thanks go to my colleagues, Stefan, Axel. S, Axel. D, Martin, Christian, Felix. B, Felix. C. A special thanks to Mathias Winter and Stefan Batzdorf for their support in writing and correcting the “Kurzfassung” of my thesis. Further thanks must be given to B.Sc. and M.Sc. students for their collaborations, especially Gerard, Jan, Anok for their patience and outstanding enthusiasm. I thank Moritz, Robert and Denis for software installations and solving issues in my PC during my work. I thank Kaushal for the proof reading and scientific suggestions for my thesis draft. I am thankful to my best friend Jithu and all my friends in Germany for their encouragement. Helpful suggestions from Rohan are also appreciated.

I am grateful to my wife Anishka for her constant encouragement, patience and support during difficult moments. I would also thank my children, Ishan and Adviti for their love and smiles. Without their patience, understanding and great support, this dissertation may have never been completed. Finally, I am exceptionally grateful to my parents for consistently pushing me to pursue my desire of higher studies in Germany.

Dortmund, 4. August 2015 Jagannath Rao Marati

Abstract

The emissions of oxides of nitrogen (NO_X) released from combustion chambers have been the subject of numerous experimental, theoretical and numerical studies in recent years. These emissions are directly related to the quality of fuel air mixing prior to combustion in gas turbines. Presently, Lean pre-mixed pre-vaporizing (LPP) concept is considered to reduce NO_X emissions in gas turbines. Therefore, their reduction relies on a more accurate prediction of transport phenomena and interaction between the liquid fuel with the turbulent gas flow field. In LPP concept, liquid fuel is sprayed onto a hot wall thereby forming a thin film. A high velocity co-current hot compressed gas stream blows over this film. The thin film evaporates, and the vapor mixes in the gas stream to form a combustible mixture. The study of the various mechanisms governing transport phenomena in such flows is an important step towards understanding the pre-mixing and pre-vaporization process. The shear force imposed by the gas flow at the gas-liquid interface causes the formation of interfacial waves, and the velocity and amplitude of the traveling waves increase with the rise in interfacial shear force. Furthermore, increase in the interfacial shear force leads to enhancement in the heat and mass transfer rates. The shear-driven flows are turbulent and characterized by strong fluctuations in the velocities of the two phases (air and liquid fuel). In order to have detailed insight of unsteady two-phase flows and thermodynamic processes, new numerical techniques and specific experiments are essential.

The present study focuses on development of numerical model for description of unsteady two-phase flows in an externally heated channel. Within the framework of this dissertation, Computational Fluid Dynamics (CFD) is utilized to elucidate the fundamental mechanisms that govern transport processes in shear-driven liquid film flows on heated walls. The numerical studies are performed in OpenFOAM, an open source CFD code written in the C++ language. The open source code is further modified to perform detailed studies of heat transfer in two-phase flows. To predict the interfacial phenomena of two-phase flow, a Volume of Fluid (VOF) approach with an Eulerian-Eulerian method is adopted. The transport phenomenon in an unsteady two-phase flow behavior is studied in combination with Continuum Surface Force (CSF) model for the surface tension force at the gas-liquid interface. A Low-Reynolds number k-ε turbulence model combined with a near-wall grid adaptation technique is applied to both liquid and gas phases.

The simulation results are verified with theoretical and experimental data from literature and also with in-house experimental data. Furthermore, the numerical simulations are performed by applying an artificial disturbance boundary condition at the inlet. The effect of gas and liquid Reynolds numbers on the hydrodynamics and heat transfer in a channel is investigated. Results of the simulation indicate that the inlet flow parameters such as gas and liquid Reynolds numbers on have a significant influence on heat transfer. Parametric analysis is employed to interpret the mechanism of wave dynamics under the influence of gas Reynolds number. The main parameters considered in this research are liquid Reynolds numbers ($300 \leq Re_L \leq 650$), gas Reynolds numbers ($1 \times 10^4 \leq Re_G \leq 7 \times 10^4$), and wall heat flux at 20 W/cm^2. The flow characteristics and

film thickness in two-phase flow are significantly affected by increasing gas velocity. The heat transfer rate is enhanced due to influence of wavy flow with increasing gas and liquid Reynolds numbers. Ultimately, this numerical study helps to explain unsteady two-phase flow behavior under heat load.

Key words: Shear-driven film, transient two-phase flow, three-dimensional, CFD, turbulence and heat transfer

Kurzfassung

Die Emissionen von aus modernen Gasturbinenbrennkammern austretenden Stickoxiden (NO_X) sind Schwerpunkt zahlreicher experimenteller, theoretischer und numerischer Studien der letzten Jahre. Diese Emissionen werden stark durch die Qualität der Gemischbildung von Kraftstoff und Verbrennungsluft am Eintritt in die Brennkammer beeinflusst. Die Verbrennung in Gasturbinenbrennkammern mit vorverdampftem und mager vorgemischtem Kraftstoff (LPP) wird als Möglichkeit betrachtet, die NO_X-Emissionen zu reduzieren. Zur Auslegung solcher Brennkammern ist eine genauere Kenntnis der Transportphänomene und der Interaktion zwischen dem flüssigen Kraftstoff und der turbulenten Gasströmung erforderlich. In LPP-Brennkammern wird flüssiger Kraftstoff auf die heiße Brennkammerwand aufgesprüht und formt einen Flüssigkeitsfilm. Die verdichtete Verbrennungsluft strömt mit hoher Geschwindigkeit über diesen Film. Dabei verdampft der Kraftstoff und bildet zusammen mit dem Gasstrom ein brennbares Gemisch. Die Untersuchung der dominierenden Transportphänomene in der Filmströmung kann einen entscheidenden Beitrag zum Verständnis der Vormischung und Vorverdampfung leisten. Die Scherkraft durch die Luftströmung an der Gas/Flüssigkeits-Grenzfläche verursacht die Bildung von Wellen an der Grenzfläche. Darüber hinaus resultiert eine Zunahme der Scherkräfte in einer Verbesserung des Wärme- und Stoffübergangs an der Grenzfläche. Scherkraftgetriebene Strömungen sind hochgradig turbulent und weisen starke Geschwindigkeitsfluktuationen in beiden Phasen auf. Um die komplexen Phänomene in der instationären Zweiphasenströmung verstehen zu können, sind neue numerische Methoden und spezifische Experimente notwendig.

Diese Arbeit dokumentiert die numerischen Simulationen zur Entwicklung numerischer Modelle für Zweiphasenströmungen in beheizten Kanälen. Im Rahmen dieser Arbeit wird eine numerische Strömungssimulation (CFD) verwendet, um die grundlegenden Mechanismen zu untersuchen, die die Transportprozesse in scherkraftgetriebenen Flüssigkeitsströmungen an beheizten Wänden dominieren. Die numerischen Studien werden mit OpenFOAM durchgeführt, einem öffentlich zugänglichen CFD–Code, der in der Programmiersprache C++ geschrieben ist. Der Quellcode wird modifiziert, um detaillierte Studien des Wärmetransportes in Zweiphasenströmungen durchzuführen. Die Volume-of-Fluid Methode mit einem Euler-Euler Ansatz wird verwendet, um die Phänomene an der Phasengrenze von Zweiphasenströmungen vorhersagen zu können. Die Transportvorgänge in instationären Zweiphasenströmungen werden mit Hilfe der Kombination der VOF Methode mit einer kontinuierlichen Modellierung der Oberflächenkraft (CSF) infolge der Oberflächenspannung untersucht. Mehrere Standard-Turbulenzmodelle für zweiphasige Strömungen werden verglichen und ein k-ε Turbulenzmodell für niedrige Reynolds-Zahlen aufgestellt. Das k-ε Modell wird zusammen mit einer adaptiven Gitterverfeinerung in Wandnähe für beide Phasen angewendet.

Die Ergebnisse der Simulationen werden mit zahlreichen theoretischen und experimentellen Daten aus der Literatur und hauseigenen experimentellen Daten validiert. Des Weiteren werden die numerischen Simulationen mit einer künstlichen Grenzflächenstörung am Einlass durchgeführt.

Der Einfluss der Gas- und Flüssigkeits-Reynolds-Zahl auf die Hydrodynamik und die Wärmeübertragung in einem Kanal werden untersucht. Die Ergebnisse zeigen, dass die Studien zu den Strömungsparametern am Einlass und den Gas- und Flüssigkeits-Reynolds-Zahlen essentiell sind, um das Strömungsverhalten zu verstehen. Parameterstudien werden durchgeführt, um die Mechanismen der Wellendynamik unter dem Einfluss der Beschleunigung durch die Gasströmung zu untersuchen. Die hauptsächlich untersuchten Parameter in dieser Studie sind die Flüssigkeits-Reynolds-Zahl ($300 \leq Re_L \leq 650$), die Gas-Reynolds-Zahl ($1 \times 10^4 \leq Re_G \leq 7 \times 10^4$) und die Wärmestromdichte an der Wand im Bereich 20 W/cm^2. Die Charakteristik der Strömung und die Filmdicke in Zweiphasenströmungen werden erheblich durch eine steigende Gasbeschleunigung beeinflusst. Durch das Phänomen der welligen Strömung im Kanal wird der Wärmetransport signifikant gesteigert. Die numerische Studie hilft dabei, das Verhalten der instationären Zweiphasenströmung unter Wärmeeinwirkung zu verstehen, sowie ein grundlegendes Verständnis der Physik und der auf die Gas/Flüssigkeits-Grenzschicht wirkenden Kräfte zu erlangen.

Table of contents

Nomenclature

Roman Symbols

Symbol	Description	Unit
A	Surface area	m^2
$[A]$	Quadratic coefficient matrix	variable
b	Constant	-
C_P	Specific heat capacity	J/kg K
C_O	Courant number	-
C_γ	Compression term constant in VOF	-
C_k, C_μ	Turbulence model constants	-
D	Characteristic length	m
d	Diameter	m
$E(\kappa)$	Turbulence energy spectrum	m^3/s^2
E_n	Eigen values	-
F	Force	N
f_1, f_2 and f_μ	Empirical functions in k-ε turbulence model	-
f	Frequency	1/s
g	Gravitational acceleration constant	m/s^2
H	Channel height	m
h	Film thickness	m
$h_{L,1}$	Film thickness in single image	m
$h_{L,avg}$	Average film thickness	m
k_s	Equivalent rough wall thickness	m
K	Curvature	1/m
K_1, K_2	Coefficient constants	-
k	Turbulent kinetic energy	m^2/s^2

Symbol	Description	Unit
L	Channel length	m
l	Length	m
M	Mass	kg
$\dot{M}$	Mass flow rate	kg/s
m	Constant	-
n	Constant	-
$\vec{n}$	Normal interfacial unit vector	-
P	Power	W
P_k	Turbulent production rate	m^2/s
p	Pressure	Pa
Q	Volumetric flow rate per unit length	m^2/s
q	Heat flux	W/m^2
$[R]$	Matrix with discretized terms	variable
r	Radius	m
S_f	Surface area	m^2
$S_\emptyset$	Source term	-
T	Temperature	K ,°C
t	Time	s
u	Velocity in stream-wise direction	m/s
u_i	Velocity component	m/s
u_t	Turbulent velocity	m/s
u^+	Non-dimensional velocity	-
V	Volume	m^3
v	Velocity in longitudinal direction	m/s
w	Velocity in span-wise direction	m/s
x	Longitudinal direction	m
y	Transversal direction	m
y_P	Distance from the cell center to the wall	m
y^+	Non-dimensional wall distance	-
z	Span-wise direction	m

Greek Symbols

Symbol	Description	Unit
α	Heat transfer coefficient	W/m^2 K
γ	Volume fraction	-
δ	Dirac function	-
δ_h	Velocity boundary layer thickness	m
δ_T	Thermal boundary layer thickness	m
ε	Turbulent dissipation	m^2/s^3
ζ	Dimensionless transverse coordinate	-
η	Kolmogorov dissipation length scale	m
θ	Dimensionless temperature	-
κ_C	von Karman's constant	-
κ	Curvature	1/m
λ	Thermal conductivity	W/m K
μ	Dynamic viscosity	kg/m s
μ_{eff}	Effective dynamic viscosity	kg/m s
ν	Kinematic viscosity	m^2/s
ν_t	Turbulent kinematic viscosity	m^2/s
ξ	Dimensionless axial coordinate	-
ρ	Density	kg/m^3
σ	Surface tension	N/m
τ	Shear stress	N/m^2
$\emptyset$	Physical variable	-
φ	Field variable	-
$[\varphi]$	Matrix containing the values of φ	variable
ψ	Eigen-function	-
Γ	Mass flow rate per unit perimeter	kg/m s
Δ	Difference	variable
∇	Nabla vector $[\partial/\partial x, \partial/\partial y, \partial/\partial z]^T$	-

Subscripts and Superscripts

Symbol	Description
0	Reference or initial value
abs	Absolute
avg	Average
ch	Channel
eff	Effective
f	Control volume face
G	Gas phase
int	Interface
i, j, k	Directions of the Cartesian coordinate system (1, 2 and 3)
L	Liquid phase
max	Maximum
n, *n*-1, *n*-2	Time step instance
Ph	Phase
t	Turbulence
s	Source
w	Wall
′	Fluctuating part
+	Normalized value

Abbreviations

Abbreviation	Description
CAD	Computer Aided Design
CCD	Charge-Coupled Device
CDS	Central Difference Scheme
CFD	Computational Fluid Dynamics
CFL	Courant Friedrich Levy
CICSAM	Compressive Interface Capturing Scheme for Arbitrary Meshes
CSF	Continuum Surface Force
CV	Control Volume
DNS	Direct Numerical Simulation
FDM	Finite Difference Method
FEM	Finite Element Method
FVM	Finite Volume Method
LDA	Laser Doppler Anemometry
LES	Large Eddy Simulation
LPP	Lean Pre-mixed Pre-vaporizing
LS	Level Set
MAC	Marker and Cell
NO_X	Nitrogen Oxides
OpenFOAM	Open source Field Operation and Manipulation
PDA	Phase Doppler Anemometry
PDE	Partial Differential Equation
RANS	Reynolds-Averaged Navier–Stokes
SGS	Sub-Grid Scale
UDS	Upwind Difference Scheme
VOF	Volume of Fluid

Dimensionless Numbers

Symbol	Description
Co	Courant number
Nu	Nusselt number
Pr	Prandtl number
Re	Reynolds number
We	Weber number

List of figures

List of tables

1

Introduction

The flow of thin liquid films driven by a shear force is a phenomenon widely encountered in many industrial applications [49, 50, 58, 120]. Such gas-liquid, two-phase flows are commonly observed in power generation (gas turbines and internal combustion engines), thermal management (electronic cooling systems), chemical processes (evaporators, distillation columns and condensers), and in automotive applications for exhaust gas treatments [8, 15, 73, 76]. The interfacial shear significantly influences the hydrodynamics and interfacial heat transfer in two-phase flow. Thus it is extremely important to design these flow systems for maximum overall efficiency. The thin liquid film generated in the two-phase flow plays an important role in modern combustor designs as it promotes momentum transfer and enhances heat transfer with co-current high-speed air-streams [154]. The details of the phenomena occurring in air-blast atomizers related to two-phase flow systems are introduced in the following section.

1.1 Two-phase flow phenomena in combustion applications

Since oxides of nitrogen (NO_X) are toxic and lead to photochemical smog as well as the depletion of the ozone layer, their increased emission in gas turbine combustion engines is a major threat to the environment. Such emissions of toxic gases give rise to environmental concerns such as global warming. Thus, the development of low-emission and efficient combustor designs for aircraft engines has been the subject of research for many years [39]. The aim of the next generation gas turbine combustion chambers is to minimize NO_X emissions. The level of NO_X formation during combustion in gas turbine engines depends on the preparation of the fuel-air mixture. However, the majority of attention has been focused on the processes of liquid fuel injection and mixing prior to the reaction of the fuel vapor/air mixture. An increase in the efficiency of combustors is essentially based on the optimization of the thermodynamic cycle, pressure and temperature level in the combustion chamber [87].

The major goal of current aircraft engine manufacturers is the realization of highly efficient combustion chambers with low pollution emissions. This can be achieved by generating a pre-vaporized fuel and air mixture to attain the desired composition before entering the combustion

chamber. Using lean premixed combustion concepts for efficient and less pollutant gas turbine combustors in power generation systems appears to be a very promising concept. Among the concepts of lean premixed combustion in aircraft engines, the Lean Pre-mixing Pre-vaporized (LPP) technology has attracted particular interest [46, 86]. This LPP concept mainly introduces uniformly mixed fuel vapor and air into the combustion chamber. Since the mixture is lean, the final temperature would be lower, thus keeping the thermal NO_X production at a low level with a high potential to reduce emissions. A successful implementation of such LPP concepts relies on the development of efficient combustion systems capable of evaporating and mixing the liquid fuel.

In LPP technology, the liquid fuel from a pressurized swirl atomizer is injected into the combustion chamber. The spray impinges on the wall forming a thin liquid film that is transported by the turbulent air stream to the air-blast atomizer lip. Turbulent air streams on both sides of the swirl walls induce high shear rates in the liquid film, thereby triggering the process of atomization [127]. This process refers to the fragmentation of a volume of liquid fuel into many small coherent droplets. A schematic of the main processes involved in pre-filming air-blast atomizers of a typical LPP concept are shown in Figure 1.1.

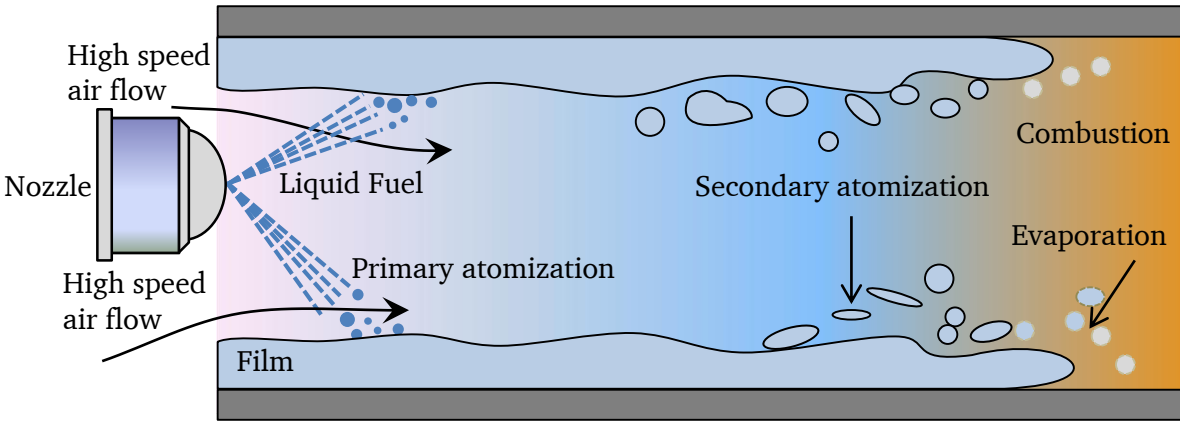

Figure 1.1: The schematic of phenomena in LPP with liquid fuel disintegration, evaporation and combustion [127]

Two main processes occur during the atomization of sprays, namely primary and secondary breakup [88]. A primary breakup process takes place closer to the region of the nozzle. During this process, the liquid fuel is disintegrated into relatively large droplets, which leading the initial evaporation and mixing of the liquid fuel. The initial mixing of spray depends on the liquid fuel droplet size distribution, the flow field, and the thermo-fluid dynamic properties of the fuel and air mixture. The high relative velocities between the liquid and gas phases induce aerodynamic shear forces at the gas-liquid interface and lead to liquid breakup [88]. Further downstream, atomization occurs due to hydrodynamic interaction processes (secondary break-up). This latter break-up mechanism consists of turbulence-induced disintegration, wherein the liquid fuel is dispersed into smaller droplets. During the atomization process, these droplets collide with the wall and create a film on the wall's surface. This wall film's interaction with the co-current gas shear leads to the entrainment of droplets. As the co-flowing air accelerates in the direction of the liquid, this could cause wave instabilities [7, 10, 89]. Turbulence in liquid film is caused by the high-speed air stream, resulting near the liquid surface in the development of waves and leading to a ligament structure appearing under strong air shear force. These ligaments are amplified and form tiny droplets due to the aerodynamic shear forces at the gas-liquid interface. This kind of process has a

large impact on the combustion process as it affects ignition and overall efficiency and pollutant emissions [88]. Understanding of shear-driven flow processes and the effect of turbulent air on the hydrodynamics and heat transfer is very challenging yet critical for improving the efficiency of modern combustion chambers and reducing pollution emissions [9].

1.2 Motivation

A better understanding of complex physics is a prerequisite when considering the evaporation of liquid fuel sheared by the strong air shear forces in promoting an effective mixing process to improve the vaporization process. The justification of parameter effects, important for overall performance, is rather difficult to understand because of the interconnection between multiple parameter effects. Accordingly, knowledge of the hydrodynamics of such interfacial flow phenomena helps in determining the key parameters through transport processes such as heat transfer on wavy film and the effect of gas shear on flow characteristics. Certain key parameters must be associated with such characteristics. These parameters are liquid and gas Reynolds numbers, the heat transfer from a solid wall to liquid, and liquid to gas. Furthermore, these parameters influence the performance of pre-filming air-blast atomizers.

An interfacial phenomenon is a complex multi-parameter problem. A clear understanding and theoretical predictions of such complex phenomenon are necessary. The importance of understanding heat and mass transfer mechanisms in liquid film flows is gaining more attention, especially the convective heat transfer mechanism, which plays an important role in the overall performance of many industrial applications. The study of such complex flow near the wall, including heat and mass transfer phenomena, is very complex and challenging. Primary focus is placed on the dynamics of the interfacial boundary, which is difficult to measure locally. Therefore, a novel numerical methodology which captures the interface between the immiscible fluids needs to be adopted.

Computational Fluid Dynamics (CFD) is the best tool for simulating the hydrodynamic and heat transfer processes in gas–liquid flows. One of the main advantages of CFD is that it can give a deep insight into understanding physical mechanisms. It can provide a local velocity field and phase distribution with a high spatial and temporal resolution for many industrial flow applications. Additionally, it has also become increasingly important in gaining insight into transport phenomena processes for the improvement of process designs. Additionally, it must be noted that the use of CFD tools facilitates the understanding of the local and global mechanisms involved in complex processes at the phase boundary. CFD techniques are used to study the complex flow situations which are difficult to explore through experimental work. Experimental research, which is time consuming as well as expensive, only yields results up to certain limits of spatial and temporal resolutions. However, CFD techniques can be applied beyond these limitations. Moreover, it must be noted that turbulence plays an important role in two-phase flows since it influences momentum between the gas and the liquid film as well as the heat and mass transfer rates. Therefore, turbulence modeling approaches are considered in CFD to investigate the numerical problem.

1.3 Outline of the thesis

Chapter 1 introduces basic information about the LPP concept comprising multi-phase flow phenomena and the motivation for the current research work. The phenomenological aspects of the gas flow over a wavy liquid surface are presented.

Chapter 2 is devoted to the extensive literature survey of experimental and theoretical methodologies related to falling liquid films and shear-driven film flows. A brief overview of previously published research related to the present study is provided. Based on this analysis the scientific objectives of the present research work are stated.

Chapter 3 presents the description of the mathematical models, including continuity, momentum, and energy equations. The concept of interface capturing methods such as the VOF method and the fundamental equations necessary to perform numerical investigations using methods for the description of turbulent flow are discussed. The formulations of the interfacial transport of momentum and heat transfer, as well as two-phase turbulence modeling, are considered. The Euler-Euler technique, which is adopted to model the two-phase flow, is also elaborated. Finally, the chapter closes on a detailed overview of surface tension force modeling.

In Chapter 4, numerical methods and the computational procedures relying on the finite volume method are elaborated. This includes a computational grid, the discretization of the partial differential equations into a solvable algebraic form; the temporal discretization; the boundary conditions; use of the computational solver; the convergence criterion; and the applied solution algorithm.

Chapter 5 deals with the results obtained with the VOF method for the two-phase flow simulation. Two different test cases are examined. For the first test case, a theoretical solution is compared with numerical simulations using Direct Numerical Simulations (DNS). The theoretical considerations for the velocity profile of a smooth laminar film flow bearing the shear force effect from a gas are presented. The second test case shows the results using heat transfer and comparing existing experimental and theoretical literature data using RANS. The numerical procedure and the results obtained from applying these procedures to comparing results with the in-house experimental data are presented. The numerical results as well as the discrepancies due to geometrical modifications while comparing with the experimental results are discussed. Furthermore, the chapter considers the influence of film thickness on heat transfer. Also provided is a comparison of the numerical results and the results of the quantitative measurements of the average film thickness on wavy films under the effect of a gas shear force. A discussion of the effect of inlet flow parameters follows. Wave characteristics, temporal film thickness, and wall temperature data are described as well. Finally, the inlet flow parameters found by various liquid and gas Reynolds numbers are interpreted in terms of the results obtained using the VOF method and turbulence model.

Chapter 6 summarizes the current research work along with the observations, conclusions, limitations of the study, and possible improvements outlining the recommendations for the future work.

2

State of the Art

2.1 Thermo-fluidic processes involved in gas-driven liquid films

The phenomenon in LPP as described in Chapter 1 occurs when the liquid fuel is injected into the hot surface and forms a layer of liquid film on the walls [127]. Due to the high co-current gas velocity, the shearing effect takes place at the gas-liquid interface leading to a wavy liquid film. Overall, the physical processes involved in such gas-driven liquid films are: shear forces on the film, flow separation, conduction, convective heat transfer and evaporation [135]. The details of the mechanisms involved and physical processes affecting the wall liquid film dynamics are shown schematically in Figure 2.1.

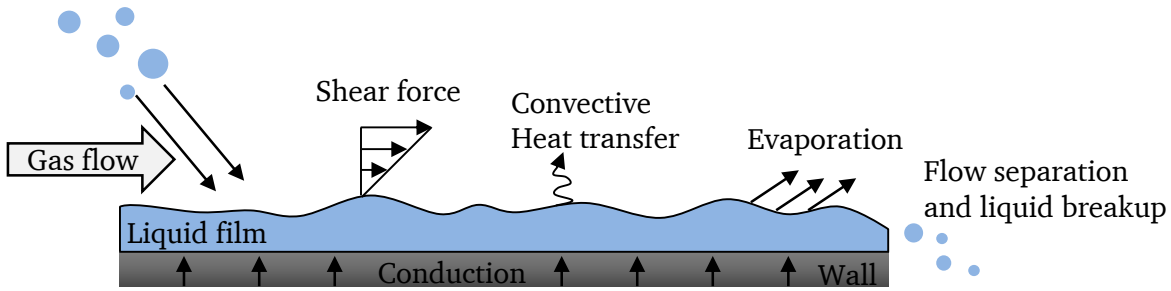

Figure 2.1: Schematic view of the physical processes governing gas-driven film flow. Figure is adapted and reproduced from Stanton and Rutland [135]

The physical phenomena involved in gas-liquid phases are dependent on the inlet flow rates and the temperatures of the gas and liquid phases. The velocity and temperature profiles are schematically presented in Figure 2.2 [154].

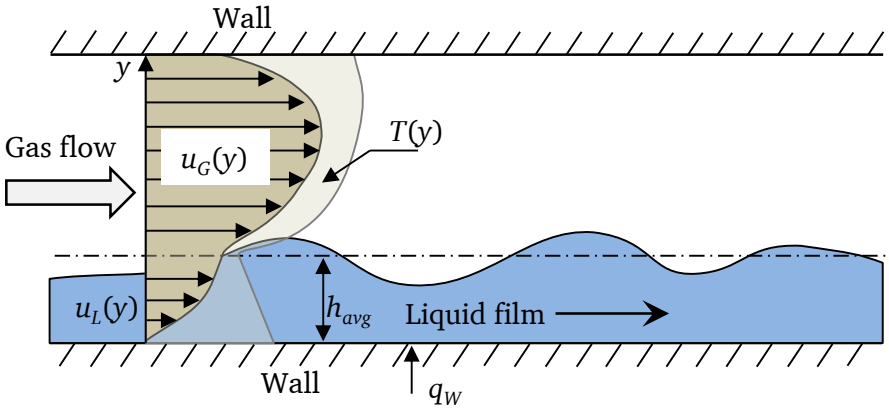

Figure 2.2: Schematic view of internal flow of LPP. Figure is adapted and reproduced from Wittig and co-workers [154]

Dimensionless numbers

The two-phase flow phenomenon can be characterized by several non-dimensional numbers, depending on the dominating mechanisms involved. These dimensionless numbers express the relative importance of two or more of the involved processes: the Reynolds *Re*, Nusselt *Nu*, Prandtl *Pr* and Weber *We* numbers, which are defined in Equations. (2.1), (2.2) (2.3) and (2.4).

Reynolds Number: $$Re = \frac{\rho u D}{\mu} \tag{2.1}$$

The above expression is the ratio of inertial forces to viscous forces, where, u and D denote the characteristic velocity and characteristic length, respectively.

Nusselt Number: $$Nu = \frac{\alpha D}{\lambda} \tag{2.2}$$

The Nusselt number is defined as the ratio of the convective heat transfer and the conductive heat transfer in the fluid. Here, D is the characteristic length $(\upsilon^{2/3}/g^{1/3})$ and α is the heat transfer coefficient.

Prandtl Number: $$Pr = \frac{C_p \mu}{\lambda} \tag{2.3}$$

The above expression is the ratio of molecular momentum and thermal diffusivity, where λ is the thermal conductivity of fluid and C_p is the heat capacity of the fluid.

Weber Number: $$We = \frac{\rho u^2 h}{\sigma} \tag{2.4}$$

The Weber number describes the ratio between inertia and surface tension forces. In the above equation, σ is defined as the surface tension.

2.1.1 Liquid film instabilities

The inertial and viscous forces at the gas-liquid interface as well as the difference in density ($\rho_L/\rho_G \sim 1000$) and viscosity ($\mu_L/\mu_G \sim 100$) affect the gas-driven liquid film, thereby causing instabilities. The difference in velocity at the gas-liquid interface is the most important reason for Kelvin-Helmholtz instability [156]. Furthermore, the liquid film becomes unstable due the effect of the gas flow on the liquid surface, and this results in a wavy film [41, 93]. Another physical mechanism followed by primary instability causes is the development of wavy film into liquid ligaments [70, 155]. The acceleration due to the aerodynamic force of the gas on the wave crests leads to Rayleigh–Taylor instability [63, 147]. In this mechanism, the liquid (heavier fluid) penetrates into the gas stream (lighter fluid), forms into high columns, and then fragments into small droplets [16]. The schematic details of Rayleigh-Taylor and Kelvin-Helmholtz instabilities are shown in Figure 2.3.

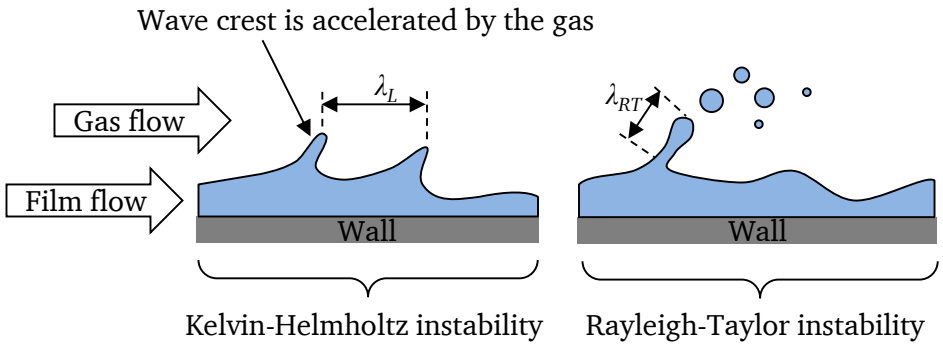

Figure 2.3: Illustration of wavy film structure arising from Rayleigh-Taylor and Kelvin-Helmholtz instabilities. Figure is adapted and reproduced from Hong and co-workers [63]

2.1.2 Wavy film evolution

Linear stability theory is valid for very small amplitudes in two-phase flows. In gas shear-driven flows, the originating waves on the liquid surface are not always periodic and their wavelength prediction is completely different from linear stability theory [71]. However, a map of wave regimes depending on the gas and liquid Reynolds numbers for various liquid viscosities has been established (see Figure 2.4) [113]. The liquid Reynolds number Re_L on the x-axis in Figure 2.4 is a function of the liquid viscosities. Furthermore, the various wave regimes recognized in Figure 2.4 are briefly explained below:

- Flat film: the liquid surface is flat (smooth).
- 2D periodic: two-dimensional waves on the liquid surface are aligned in the stream-wise direction. The frequency is regular and the amplitude of the waves is low. Thus, this wavy regime is characterized by the linear stability theory.
- 3D periodic: the 2D periodic waves develop into a 3D wavy pattern when the gas velocity and varying flow conditions increase (see Figure 2.5). The wave front velocity varies due to fluctuations in the wave amplitude [1].
- Solitary waves: this wave regime consists of irregular and asymmetric waves. These irregular waves carry a significant amount of liquid, causing fluctuations in the liquid film thickness [113]. These solitary waves lead to rolling waves and are fragmented into small droplets by the gas shear force.

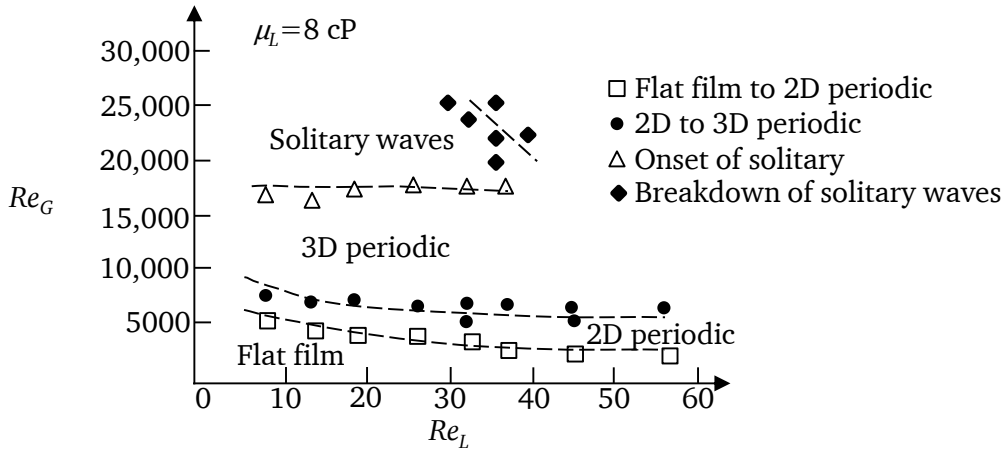

Figure 2.4: Regimes of waves in shear-driven film flows in a map with gas Re_G and liquid Re_L Reynolds numbers as coordinates [113].

Three-dimensional waves are influenced by the pressure gradient, the temporal change of momentum, the convective momentum transfer in all dimensions, and the viscous momentum transfer in the x and z directions [1]. Figure 2.5 shows a schematic of a three-dimensional wave, gaining additional momentum from the flowing fluid at the centerline of the z coordinate. The negative pressure gradient and the convective momentum transfer in the x direction within the wave front region become positive in the back region [1]. Schemes based on an interpretation of individual terms of the Navier-Stokes equation such as pressure gradient, temporal velocity change, and convective momentum transport are provided in Table 2.1 [1]. It is noted that most of the terms have different signs at the wave front and at the wave back (see Figure 2.5).

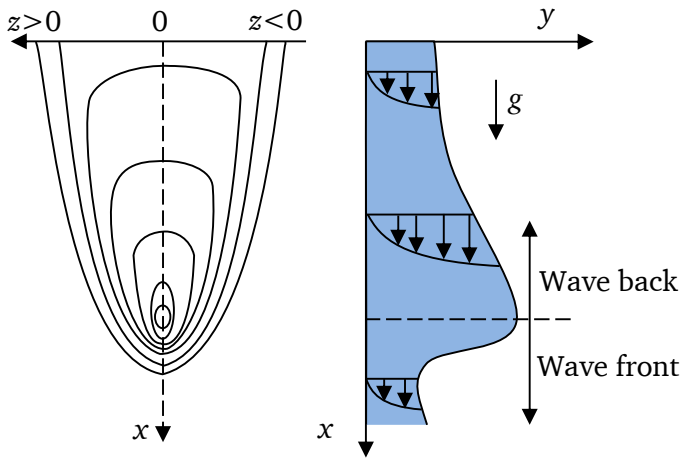

Figure 2.5: Schematic of a 3D-wavy film, top view (left), side view (right). Figure is adapted and reproduced from Adomeit and Renz [1]

Table 2.1: Estimated signs of physical terms contributing in the wave front and wave back regions in a 3D wave. The interpretation of these individual terms are adapted from Adomeit and Renz [1]

Term	Wave front	Wave back
Temporal change $\left(\frac{\partial u}{\partial \tau}\right)$	> 0	< 0
Pressure gradient $\left(\frac{\partial p}{\partial x}\right)$	< 0	> 0
Convective x-momentum transports $u\left(\frac{\partial u}{\partial x}\right)$ in the x-direction	$u > 0, \left(\frac{\partial u}{\partial x}\right) < 0$	$u > 0, \left(\frac{\partial u}{\partial x}\right) > 0$
Convective x-momentum transports $v\left(\frac{\partial u}{\partial y}\right)$ in the y-direction	$v > 0, \left(\frac{\partial u}{\partial y}\right) > 0$	$v < 0, \left(\frac{\partial u}{\partial y}\right) > 0$
Convective x-momentum transports $w\left(\frac{\partial u}{\partial z}\right)$ in the z-direction	$w > 0, \left(\frac{\partial u}{\partial z}\right) < 0$	$w > 0, \left(\frac{\partial u}{\partial z}\right) < 0$

2.1.3 Liquid entrainment phenomena

As discussed in the previous section, the liquid film changes into a rolling wavy film when the effect of the high gas shear on the liquid surface causes shearing-off at the wave crest. The sheared liquid enters the gas phase in the form of droplets, a process known as liquid entrainment. These small droplets in the gas phase are deposited on the liquid film. The process of entrainment and

deposition is dynamic with a continuous exchange of mass, momentum, and energy between the liquid and gas phases [25, 32, 51, 110]. This process of rolling wave entrainment and shearing-off is schematically demonstrated in Figure 2.6. Within the process, the tip of the disturbance wave is rolled forward at high gas speed and subsequently entrained into small liquid droplets [58, 64].

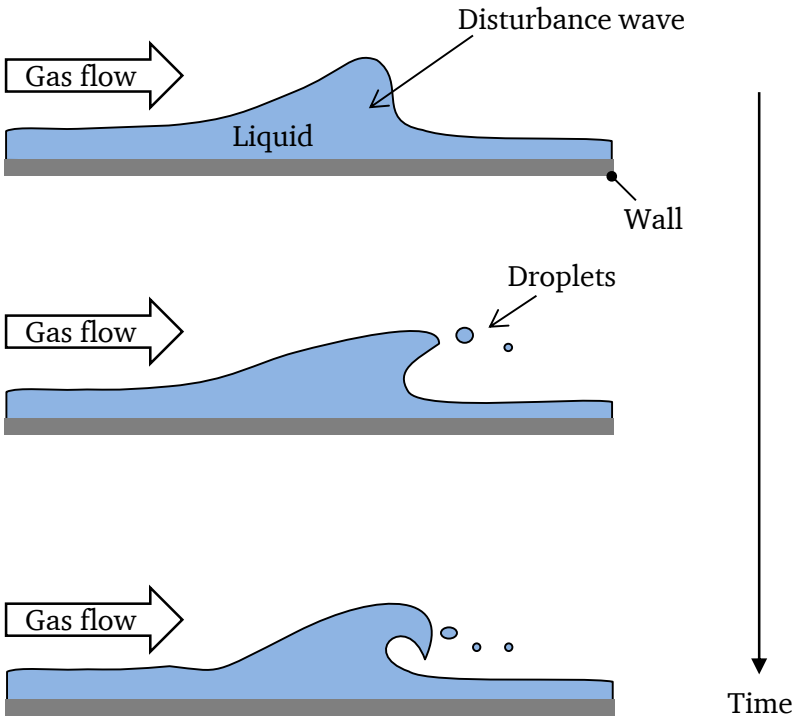

Figure 2.6: Schematic of the mechanism occurring in roll wave entrainment [58]

2.2 Literature review

One of the key objectives of this thesis is developing a suitable flow solver which can numerically predict the wavy interface of a liquid film. This would facilitate the understanding of the physical processes involved in shear-driven film flows. To develop such a solver, it is necessary to understand the possibilities and limitations of computer simulations of multiphase flows and experimental data. In the following sections, the physical principles of shear-driven film flows and the current state of research related to two-phase flows are explained.

2.2.1 Shear-driven flows: experimental investigations

Hanratty and Engen [50] studied the interaction between a turbulent air stream and a parallel flowing water film. The experimental test section of a horizontal rectangular channel with an aspect ratio of 1:12 was considered. They measured the pressure drop and velocity profile in the

gas, which reflected the effect of changes of the liquid surface upon the flow in the gas phase. In their experiment, liquid and gas flow rates as well as film height were varied. The data they gathered was correlated in terms of liquid and gas Reynolds numbers. The authors observed that the liquid's movement was affected by the resulting drag of the air flow. In their research, the transition from a smooth surface to one made up of two-dimensional waves occurred at a critical liquid Reynolds number of about 520. The researchers also reported that small droplets began to loosen from the liquid surface at higher gas Reynolds numbers ($Re_G = 39{,}300$) and that the velocity profile of the gas was affected by the liquid surface's waviness. According to the investigators, the effect of the gas flow on the liquid can be described in terms of the following types of liquid surfaces:

- smooth,
- two-dimensional waves,
- roll waves,
- dispersed flow.

Jurman and McCready [72] studied the behavior of thin waves of shear-driven films in co-current flowing air with water and water-glycerol mixtures. The dynamic viscosities of the water-glycerol mixtures varied from 0.013 to 0.015 kg/m-s. In this range of viscosity of water, the wave structure is no more complex than that observed in ordinary water. The experimental setup using a channel length of 9 m was arranged horizontally with a rectangular cross-section of 0.3 x 2.54 m^2. The qualitative analysis was done by measuring waves with parallel wire conductance probes. The waves were generated due to interfacial instabilities caused by liquid inertia in the presence of gas shear on the liquid surface. It was observed that at low Reynolds numbers with the gas Reynolds number $Re_G = 9850$ and liquid Reynolds number $Re_L = 3$, waves were sinusoidal. Three-dimensional waves were observed when the film thickness decreased due to an increase in the gas velocity. Researchers also observed the formation of solitary waves within the region at the beginning of the channel. In order to validate the data obtained from the experiments, a non-linear wave equation was derived using a boundary layer approximation to describe the amplitude, shape, and interaction of the amplitude waves. The experiments yielded the following results:

- for $Re_G < 9850$ and $Re_L < 3$, two-dimensional waves predominate,
- for $Re_G < 9850$ and $Re_L > 3$, 3D waves appear and a reduction in film thickness occurs,
- for $Re_G < 9850$ and $Re_L > 30$, no waves were detected.

Andreussi et al. [5] investigated the instability conditions for the formation of roll waves during the interaction of the gas and liquid phases by varying fluid viscosity. The experimental apparatus was 10 m in horizontal length, with a rectangular cross-section of the dimensions of 2.54 x 30.5 cm^2. In order to vary the viscosity of the fluid, glycerin-water mixtures were used. It was observed that the transition to roll waves at the interface was due to the destabilizing effect of fluid inertia. The authors concluded that the formation of roll waves happened above a gas Reynolds number of 20,000. Consequently, the liquid viscosity at the critical liquid Reynolds number has a lower influence on the formation of roll waves. It was further observed that at high liquid viscosities, there is a trend towards the formation of two-dimensional waves.

Pilmon [114] performed experiments determining the velocity profiles of shear-driven liquid films in a transparent rectangular channel with the dimensions 0.012 x 0.1 m^2 and a length of 0.4 m. The film thickness was measured by a fluorescent method. In this method, liquid ink was added on the film surface, and the local fluorescent particles were stimulated by means of a focused laser beam. The author also measured the velocity profile via an LDA system with a resolution of 20 microns and concluded that the mentioned measuring method is an appropriate way for determining velocity profiles.

Alekseenko et al. [3] undertook an experimental investigation of liquid falling films under the influence of a turbulent gas flow in the opposite direction. The test rig used in the analysis was constructed using a vertical transparent plastic tube of 1 m in length and 15 mm in diameter. Distilled water was used as a test fluid in the experiment, mixed with glycerol and sodium chloride at 0.1 mass percent. The waves were generated by vibrations of a membrane positioned at the tube inlet. The Reynolds number of the fluid was maintained between 24 and 125, and that of the gas varied from 0 to 8000. For the measurement of wave parameters, a method based on the conductivity of the coaxial electrodes was used. The wave parameters were influenced by a destabilizing effect of the co-current flow of the gas on the liquid film. The purely laminar flow pattern is not observed during atomization because of the high velocity of gas flows. In addition, shearing of the liquid induced by the accelerated turbulent gas phase leads to turbulent flow.

Sattelmayer and Wittig [125] demonstrated the influence of the gas phase velocity, film loading, surface tension and viscosity on the film's disintegration in LPP applications. Aigner and Wittig [2] characterized the factors influencing the atomization in cylindrical swirling air-blast atomizers. Sattelmayer et al. [124] used optical instruments for the investigation of wavy liquid films in their experiments. Wittig et al. [154] and Himmelsbach et al. [59] examined the interaction between a laminar liquid film and a turbulent gas phase (see Figure 2.7) as well as the evaporation modeling of a wavy film. The gas-liquid interaction depends on the mass flow rates and temperatures of the two phases as well as on the local temperature gradient. In order to compute such a gas-liquid interaction, appropriate simplifications must be considered such as the temporal averaging of the film's height, gas, and liquid velocities. The authors measured the flow of a shear-driven thin liquid film in a duct and proposed a model based on the concept of an "equivalent rough wall, k_s" for simulating a shear-driven flow (see Figure 2.7). The researchers argued that the undulations of the liquid film can be treated as wall roughness, with the roughness being a function of the interfacial shear stress and the average liquid film thickness. The interfacial shear stress provides coupling between the liquid film and the gas flow through an iterative scheme, which is applicable to two-dimensional flows.

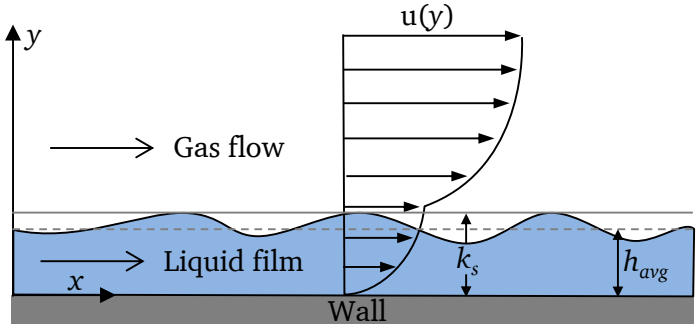

Figure 2.7: Simplified representation of a shear stress-driven wavy wall film [59]

The experimental determination of the velocity profile in a wall liquid film driven by shear stress as a function of the film thickness is essential for the further development of numerical models. Therefore, Wittig et al. [153], Samenfink et al. [123], Elsaesser et al. [34] and Schober et al. [129] performed experimental research on such shear-driven film flows. The modified experimental setup was based on a combination of film thickness measurement techniques and Laser Doppler Anemometry (LDA) for determining the velocity of the gas phase instead of the Pitot tube method. The measured value of the average height of the film was approximately 100 μm. It was found that the flow of the liquid film in the domain is highly turbulent.

Elsaesser et al. [35] and Schober [128] studied the fuel preparation and the dynamics of shear-driven wall films in detail. Their aim was to develop a suitable method to achieve a high temporal and spatial measurement resolution of the flow variables in wall films. Rosskamp et al. [119] developed an improved model to calculate the heat transfer between the film applicator (see Figure 1.1 the wall, and the wall film. This model is based on the waviness of the film because of internal flow and the local Nusselt number. The authors concluded that the surface tension, density, and viscosity of the fuel significantly influenced its primary atomization [119]. The experimental studies show that the physical properties of the fluids, as well as the flow conditions of liquid film and of the surrounding gas phase, significantly influence the primary atomization. It was also determined that the interaction at the interface was particularly important.

Gepperth et al. [45] investigated the influence of the fluid's physical properties on the air velocity and the film loading on the primary atomization on a flat film applicator edge. Phase Doppler Anemometry (PDA) measurements were also performed downstream of the atomizer in order to determine the characteristic mean diameter of the fuel drops. Müller et al. [103] considered shadowgraphy and high-speed visualization techniques to investigate the transient processes of wave formation and disintegration of the liquid film at the trailing edge.

Helbig [54] investigated the hydrodynamics and evaporation processes in gas-driven liquid films. Various film thickness measuring techniques were utilized and compared. The advantages and disadvantages of the various measurement techniques were also identified. Moreover, experiments were performed to study heat transfer with and without the gas flow at various temperatures on the heated walls. A schematic representation of the experimental apparatus used by Helbig [54] is shown in Figure 2.8. Main critical parameters such as film thickness, wave velocity, and wave frequencies were determined both through investigating the hydrodynamics and evaporation of a liquid film. A comparison of various film parameters was performed on an unstructured (smooth) and a structured surface with triangular grooves. The results indicated a 40% improvement in heat flux for structured surfaces. The author measured the film thickness and wave velocities for both structured and unstructured surfaces, concluding that the wave length and wave period for low Reynolds numbers on structured surface are higher. Overall, Helbig [54] summarized the need for continued investigation of two-phase flows with high accuracy. Furthermore, it is necessary to compute such complex flow problems with reliable physical models and numerical methods. Budakli et al. [21] performed heat transfer measurements on shear-driven liquid films flowing on micro-structured heated tubes, and found a higher heat transfer coefficient on the micro-structured tube than on the smooth tube.

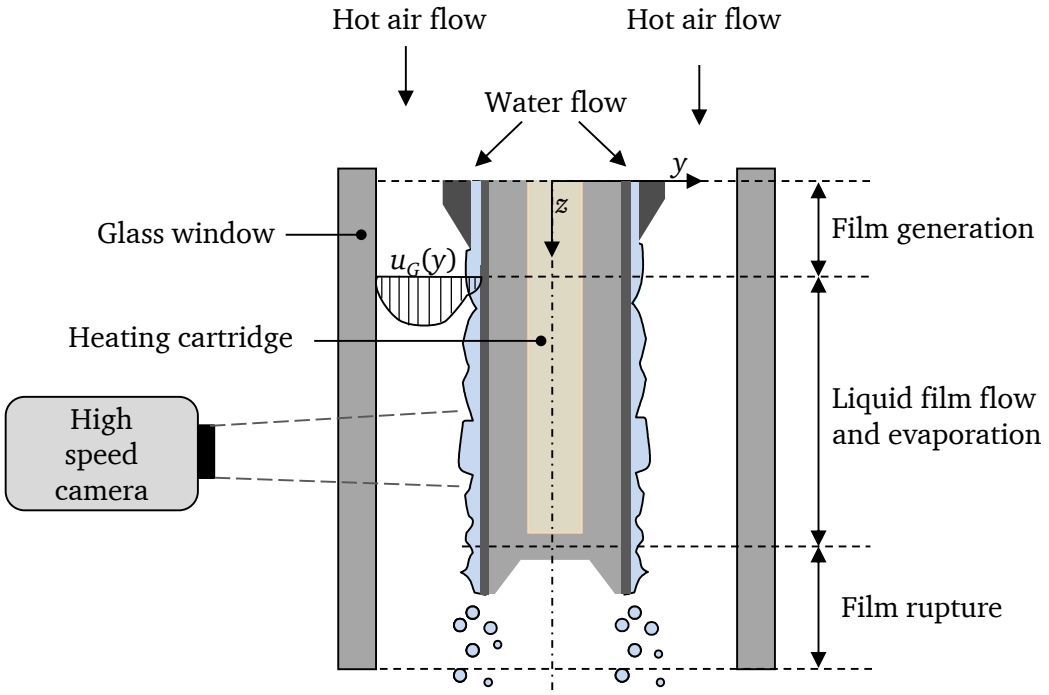

Figure 2.8:Test section diagram of the experimental study of the wavy film according to Helbig [54]

2.2.2 Theoretical and numerical studies of shear-driven liquid films

Ebner et al. [33] investigated the effect of air shear force on liquid films in pre-film fuel atomizers for modern aircraft turbines. The effect of a pressure gradient in the air flow and local varying film loads were studied to characterize the liquid film behavior and develop a mathematical model to describe the velocity field of the turbulent air and liquid film. The authors were able to predict the evaporation rate and velocity of the propagation of waves of liquid films on smooth walls using this mathematical model. The latter also allowed them to compute the liquid wall film through a 2D boundary layer approach by modeling the liquid film as a turbulent boundary layer flow. The governing equations within the developed CFD code were solved using a finite difference method. The model's high accuracy has been proven in a wide range of pressure gradients. Furthermore, the behavior of the film was noted to depend mainly on the exchange of momentum at the air to liquid interface. The effect of an accelerated air flow as well as varying liquid film flow rates on the film dynamics and at the gas-liquid interface are discussed. The authors concluded that the validated model can be applied to all technical applications where shear-driven liquid film phenomena play a major role for development and optimization.

2.2.3 Heat transfer in two-phase flows

The heat transfer in a two-phase flow under the influence of a counter-current air flow in an 8 m long pipe with an inner diameter of 76 mm was investigated by An et al. [4]. A film of water was

supplied to the inner side of the electrically heated tube. In the experiments, the water temperature at the inlet was varied between 293 K and 353 K. The authors further described the strong decrease of the wall temperature along the pipe for the gas Reynolds number range of 4600 - 13800 and showed that evaporation is dominant above a liquid temperature of 328 K [4].

Kitagawa et al. [75] investigated heat and mass transfer experimentally and numerically in a liquid film with a counter-current turbulent air flow in a vertical stainless steel tube with a length of 500 mm and an inner diameter of 11 mm. The temperature measurements were recorded with 108 pairs of thermocouples, which were welded with a 10 mm gap, and an inlet gas Reynolds number was maintained at $Re_G = 32000$. The authors observed a high heat flux with a strong increase in the wall temperature and tearing of the film. They also found a very good agreement between experimentally determined and numerically calculated results in the uninterrupted part of the film region. Furthermore, it was determined that airflow enhances the heat transfer significantly.

Chun and Seban [23] studied heat transfer on a vertical stainless steel tube with a length of 610 mm and an outer diameter of 28.5 mm. The tube was heated electrically along the length of a 300 mm section, and a distilled water film was applied to the outside. The experiments were performed at $320 < Re_L < 21000$ and $1.77 < \mathrm{Pr} < 5.7$. Thermocouples were used to measure the wall temperature. The results showed that the Nusselt number decreases in the region of laminar flow to a minimum, subsequently rising again with an increasing liquid Reynolds number Re_L. The authors further concluded that, apart from the Reynolds number, the Weber number is also an important parameter for heat transport.

Shmerler and Mudawar [133] investigated heat transfer in falling films on a vertical tube (length $L = 1838$ mm, outer diameter = 25.4 mm). The tube was composed of various materials with fiber glass ($L = 757$ mm) at the top, polyethylene ($L = 300$ mm) in the middle, and stainless steel at the end ($L = 781$ mm). The stainless steel portion was heated electrically and the wall temperatures were measured with thermocouples. The Prandtl number (2.55 - 6.87) and the Reynolds number (2500 - 39500) were varied to determine the Nusselt number. The authors realized that the heat transfer coefficient decreases first and then increases along with Re_L. They also found their findings to be consistent with the results of Chun and Seban [23]. In addition, Shmerler and Mudawar [133] concluded that the heat transfer coefficient increases with an increasing Prandtl number and derived a correlation (2.5) for the heat transfer in the turbulent region.

$$Nu = \frac{\alpha}{\lambda}\left(\frac{\nu^2}{g}\right)^{1/3} = bRe_L^m Pr^n \tag{2.5}$$

The coefficient $b = 0.0106$, $m = 0.3$ and $n = 0.63$ show an average error of 5.5% and a standard deviation of 17%.

Leuthner [91] experimentally studied heat transfer in a falling film evaporator of 2600 mm in length with an outer diameter of 25.5 mm. An electric heating part was included in the experiment. Water and a water-ethylene glycol mixture were used as fluids, and experiments were performed at a reduced pressure of $P_{abs} = 0.02$ bar. The researcher concluded that the heat transfer coefficient is dependent on the length of the tube [91].

Rosskamp et al. [120] investigated the evaporation process of a shear-driven liquid film surrounded by a hot turbulent air flow. The experimental setup consisted of a rectangular channel

with the cross-sectional dimensions 0.1 x 0.055 m and a length of 1.2 m. The experiments were undertaken by varying gas temperatures between 314 and 373 °C at normal pressure conditions. In the experiments, the gas Reynolds number of 81,000 was increased up to 162,000, and the liquid mass flux of water was varied from 33 to 100 g/(ms). To measure the temperatures, thermocouples were used at 13 locations in the channel. The film thickness was determined by the laser absorption method. The analysis of the measured values included interfacial shear stress, gas phase velocity, and temperature profiles. The results showed that film thickness increases with decreasing shear stress on the liquid surface. It was found that the behavior of a turbulent boundary layer and a boundary layer on a dry surface are qualitatively similar.

Kabov et al. [74] studied locally heated shear-driven liquid films on heated surfaces in micro-channels with the influence of thermo-capillary forces on convective heat transfer theoretically, numerically, and experimentally. The simulation results showed a strong dependence of tangential shear stress on the shape of the liquid surface, and the effect of the gas pressure was found to be insignificant. Furthermore, the dominant driving force of friction on the liquid surface was observed at $Re_L / Re_G < 0.35$. The experiments were performed in a mini-channel with a width of 40 mm and an adjustable height of 1-3 mm, while an infrared scanner (resolution of 0.06 K) was used for temperature measurements. The investigators also observed that the shear-driven liquid film is stable relative to the wave formation over a range of liquid and gas Reynolds numbers. Finally, the researchers concluded that the critical heat flux at which the rupture of a liquid film in shear-driven films takes place is up to three times higher than that of vertical falling films.

Dietze et al. [29] studied the phenomenon of backflow in the capillary wave region of laminar falling films. The study was undertaken on an inclined liquid film flow with surface waves externally excited at a forcing frequency. In order to measure the local stream-wise velocity component, the Laser-Doppler velocimetry technique was used. Computations were also executed using the volume of fluid method and compared with experimental data in the developed flow region. The authors concluded that the pressure distribution was inducing deformation and causing the separation of the flow in the capillary wave region.

2.2.4 Computational methods for two-phase flow

A two-phase flow system including dynamic interface phenomena is critical for the design and analysis of LPP chambers and many other related industrial applications. The challenge lies in locating the phase boundaries and transporting them into the numerically discretized solution using phase boundary resolution methods. Moreover, the physical quantities, such as viscosity, density, and pressure at the interface, experience a step change. For the study of the physics of gas-liquid flows, several models for tracking the interface with explicit treatment and the macroscopic continuum methods have been developed over the past few decades. In order to capture the interface of the immiscible two-phase fluids, an accurate model without introducing large errors is essential [80, 139]. The numerical method for the simulation of physical phenomena can be distinguished based on the reference coordinate system of the governing equations. The two-phase flow formulation can be categorized into Lagrangian and Eulerian types of methods based on the spatial and temporal resolution [11].

In the Lagrangian type of method, a moving computational grid describes the motion of the interface and is responsible for the grid deformation in each time step as depicted in Figure 2.9.

This method is robust, and the mesh may be distorted for many flow simulations. However, these methods are not applicable for flows with large deformations. In this approach, closure relations are considered to account for the interfacial forces and these closure models can be obtained from empirical relations [38]. The calculation of the gas and liquid phases requires two reference frames. The reference frames must be coupled in a suitable manner in order to ensure the exchange of information between the two phases and the consideration of interfacial effects. Hence, computational resources for the simulation of complex flow within complicated geometries increase significantly. In this grid-based method, a severe deformation of the grid is caused by complex grid cells, which greatly affect the accuracy of computation.

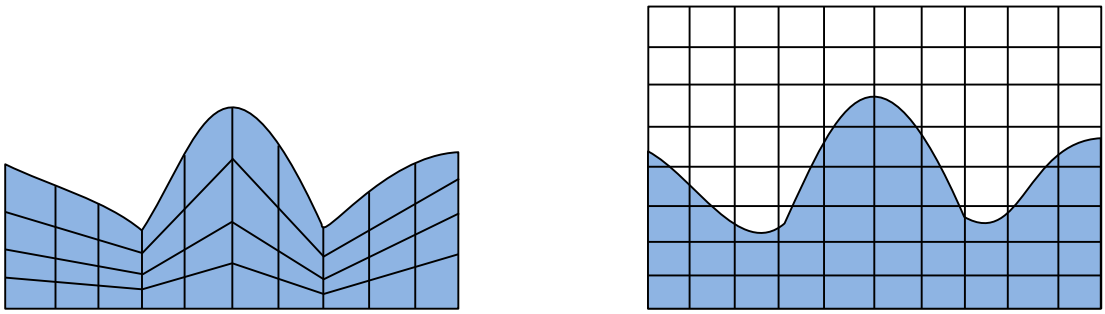

a) b)

Figure 2.9: a) Sketch of the Lagrangian type of mesh deformation: the interface describes the moving boundary of the computational grid, b) the Eulerian type of interface capturing on a fixed grid [38]

In the Eulerian method, both phases are treated as a single continuous medium. Conservation equations are formulated in a fixed computational grid in the entire flow domain. This fixed grid method reduces computational efforts compared to the moving grid of the Lagrangian method [48, 97]. This approach is also easily extended to the three-dimensional flow problems. The major advantage of this method is its ability to capture arbitrarily shaped interfaces and large deformations [142]. This approach in a stationary coordinate system is considered to be relatively robust. Currently, the most commonly used interface capturing models based on the Eulerian formulation in numerical simulations are the marker and cell (MAC), the level set function (LS), and the Volume of Fluid (VOF) model. A common disadvantage of these models with regard to multi-phase flows is their inaccurate determination of interfaces due to numerical diffusion. However, the latter can be minimized by refining the grid elements in the interfacial region. In the following, the three methods for interface capturing are described in greater detail.

The MAC method is based on an Eulerian grid approach which was originally developed for the modeling of free surface flows [52]. In this method, Lagrangian virtual particles are used to store the coordinates and which move from one cell to the next during computation (see Figure 2.10) [98]. This method's disadvantage lies in the effect of the markers' accumulation at the interface in highly curved regions. The velocity at which the labels are moved is calculated by interpolating the speed of the adjacent nodes of the computational grid leading to numerical instabilities. This method is not suitable for liquid breakup, as it probably leads to unphysical fluctuations of density, velocity, and pressure. In addition, this method is computationally expensive because the interface is resolved for the location of the particles in each iteration during simulation.

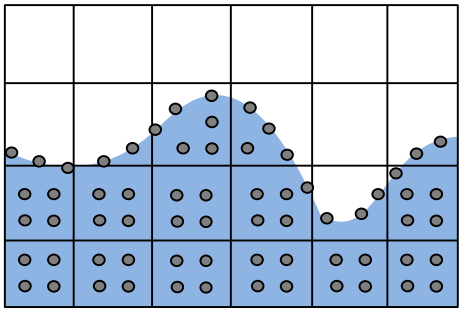

Figure 2.10: Illustration of the MAC method [98]

The LS method illustrated in Figure 2.11 introduces a signed distance function which is defined as zero at the interface, and which takes positive and negative values on either side of it [137]. In this method developed by Osher and Fedkiw [107, 108], the interface is captured by solving a scalar transport equation. The interfacial behavior is defined by a time-dependent initial value problem [131]. Sussman et al. [137] successfully implemented the numerical simulation of an incompressible two-phase flow with a density ratio of 1000/1. An overview of the LS methods can be found in the work of Sethian and Smereka [132]. This method has a simple mathematical formulation and is easy to implement [80]. Enright et al. [36] combined the Lagrangian marker particle method with the LS method to maintain a smooth geometrical curvature of the gas-liquid interface. However, the transport equation does not fit the law of conservation and requires re-initialization at every time step, which is a major drawback [104]. In order to reduce computational time while studying the movement of the interface, a fast marching algorithm has been developed, improving upon the LS method [130]. A major disadvantage of this approach is that the mass balance is not strictly fulfilled, especially in regions with low spatial resolution. In order to model multiphase flows with sufficient accuracy, Fedkiw et al. [37] combined the LS approach with the ghost fluid method. This procedure enables the accurate description of the density discontinuity at the interface of a two-phase flow in the form of a step function, that is, without diffusion of the density and the extent of the interface across multiple cells. The ghost cells are used to describe both fluids in the entire computational domain. Flow variables of both fluids are determined at each time step at each discretization point in space. The difficulty in this approach lies in the appropriate definition of ghost cells and assigning the correct physical quantities corresponding to the required boundary conditions at the phase interface. Pai et al. [109] turned to the level-set modified SRI (Spectrally Refined Interface) method by imposing a stationary laminar velocity profile at the inlet. The size of the computational grid used was very high and varied between 36 million and 110 million grid points. Herrmann [56] used the RLSG (Refined Level Set Grid) method to improve accuracy by varying the numerical grid size which was varied between 8.7 million and 110 million grid points.

Currently, the commonly used model based on the Eulerian formulation in numerical simulation is the VOF model. Hirt and Nichols [61] first introduced the VOF method in 1981 to capture the interface using the Eulerian method, satisfying the law of conservation of mass. To capture the interface, this method uses a volume fraction function based on the volume percentage of control volumes [136]. The sum of the volume fractions is equal to one, and these volume fractions are continuous functions of spatial coordinates and time. This VOF method is based on single fluid flow formulation combined with a mathematical model to track the location of the interface on a fixed grid. Scardovelli and Zaleski [126] reported a detailed review of the VOF methods and their

applications. The VOF method is widely applied in the simulation of two-phase flows involving immiscible phases because the mass is conserved. Its innovative aspects have been applied to various applications of two-phase fields by several researchers. Accordingly, many research articles can be found on the topic. However, an accurate computation of accurate local interface curvatures from volume fractions is challenging in the VOF method. Several interface-capturing methods have been developed with the aim of reducing the disadvantages associated with VOF and the level set method. There are several interface-capturing methods that have been developed with the aim to reduce the disadvantages associated with VOF and the level set method. The details of couplings between the level set and VOF method are mentioned in the works of Menard et al. [99], Sussman and Puckett [136], Sussman et al. [138] and Van Der Pijl et al. [145].

Miyara [101] numerically simulated the wave formation over the falling liquid films using the VOF method and compared it with experiments. The researcher concluded that the optimum waveform is necessary to promote the heat and mass transfer across the interface. Lan et al. [82] simulated a 3D shear-driven film in a rectangular duct using the VOF model, validating the measured film thickness data. The results determined that the two were in very good agreement. The results determined that the two were in very good agreement. Gao et al. [42] and Hashmi et al. [53] performed numerical simulation of stratified two-phase turbulent flow using the VOF model including the Continuum Surface Force (CSF) model for the effect of surface tension force. In order to avoid the LS method's main drawback (loss of mass conservation), Sussman et al. [138] proposed a coupled LS-VOF method in which the LS function is used to compute the normal vectors to the interface instead of the VOF fractions. In another approach of coupled LS and VOF methods, Van der Pijl et al. [145] used the VOF function to ensure mass conservation by avoiding reconstructing the interface techniques. This research report is mainly focused on the interface capturing method using the VOF method and the mathematical modeling details, which are presented in Chapter 3.

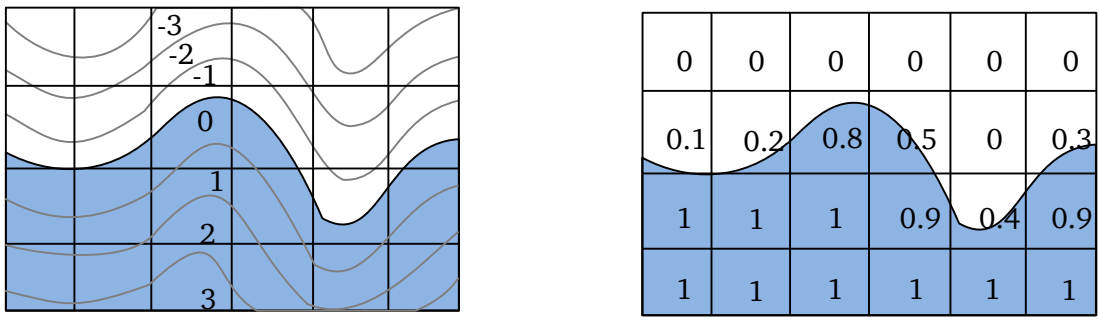

Figure 2.11: Illustrations of the LS (left) and VOF (right) methods [61, 137]

Treatment of the interface in the VOF method

To achieve a sharp representation of the phase boundary in the numerical treatment and to avoid smearing the phase boundary, various special methods have been developed. A detailed overview of interface treatment during computation is provided in the work of Rider and Kothe [116]. In

OpenFOAM, the Compressive Interface Capturing Scheme for Arbitrary Meshes (CICSAM) is implemented in the VOF method based on the work of Ubbink [141]. CICSAM is an explicit scheme that can maintain the sharp interface in geometrical re-construction schemes implemented in commercial codes. In this approach, an extra term "interface-compression velocity (u_C)" is introduced in the proximity of the interface. This extra term improves the interface resolution by steepening the volume fraction gradient. The modified conservation equation for volume fraction with an additional convective term is provided in the following form [141]:

$$\frac{\partial \gamma}{\partial t} + \nabla \cdot (u\gamma) + \nabla \cdot \big(u_C \gamma(1-\gamma)\big) = 0. \tag{2.6}$$

The last term on the left-hand side of the above equation is referred to as an artificial compression term. Here, the factor $\gamma(1-\gamma)$ is active only at the interface; i.e. it is non-zero at the interface. The advantage of this formulation (2.6) is the preservation of the steep gradient of the indicator function without any geometric reconstruction of the phase boundary [149]. The determination of compression velocity u_C is based on the maximum velocity at the interface, which is calculated as:

$$u_C = min\big[C_\gamma |u|, max(|u|)\big] \frac{\nabla \gamma}{|\nabla \gamma|}. \tag{2.7}$$

In the above expression, C_γ is a constant controlling the intensity of the compression term [141]. The value of constant C_γ is assumed to be zero for no compression and $C_\gamma = 1$ is considered to represent conservative compression. The CICSAM algorithm is available with the OpenFOAM solver code and provides accurate results for the interfacial position on various resolution grid elements. The re-construction of the interface is not considered in this work, and the adapted method corresponds to the one reported in the work of Rusche [122]. The pressure and velocity components are coupled through the Pressure Implicit with Splitting of Operators algorithm (PISO) for transient two-phase flows [65]. The details and a summary of the OpenFOAM solver are presented by Jasak and Rusche [67, 122].

Numerical description of surface tension force modeling

The surface tension is a balance of the inward intermolecular attractive force with the upward pressure gradient force across the interface in two-phase flows. The most common methods to model the force produced by the surface tension are the Continuum Surface Force method (CSF) [17], the Continuum Surface Stress method (CSS) [79], and the ghost fluid method [62, 99]. The surface tension force must be considered as one of the most important factors in the consideration of the gas-liquid flow simulations. The surface tension occurs as the surface force in nature results in a reduction to the interface between two phases. However, the implementation of the simulation of a surface force in a fixed grid based on finite volume methods (FVM) proves to be difficult. Hence Brackbill et al. [17] implemented the effect of surface tension force along the interface between the phases by employing the CSF approach in the VOF method. The coarse resolution of the grid during the computation of the surface tension based on the interface curvature leads to an approximation error. Therefore, large errors can occur especially in the

reconstruction of three-dimensional interfaces. Due to inaccuracies in the surface tension modeling, the exact interface is not represented physically [17]. Although a grid refinement of interfacial resolution leads to a minimization of these errors, the computational effort increases enormously.

2.2.5 Numerical perspective of turbulence modeling

The study of turbulence phenomena in two-phase flows has been performed over the past few decades. Brauer [18] reported an initial survey of various turbulence sources in two-phase flows. According to his research, turbulent intensity in two-phase flows is due to fluctuating velocities, such as in single-phase flows. In recent years, incorporation of turbulence effects into single-phase flow computations have been developed [117, 152]. Turbulence modeling is crucial for the CFD modeling of two-phase flows. Single-phase turbulence models have been adapted to two-phase flow simulations by accounting the grid size in the vicinity of the interface region.

In the context of shear-driven flows, a numerical code to compute the interaction between gas phase and liquid film flow on a flat surface was developed by Wittig et al. [154]. In this numerical study, the gas phase was based on the Reynolds-averaged Navier-Stokes (RANS) equations using the finite volume method computed with in-house flow solver code Elliptic Package On Shear-flows (EPOS) for three-dimensional turbulent flows. The liquid film was assumed by a fixed boundary layer near the wall. The gas and liquid phases were coupled through the exchange of mass, momentum, and energy, and simulated the two-dimensional code through the boundary layer approximation. Wittig et al. reported that the simulation results agree well with the values determined by corresponding measured values of the film thickness under ambient conditions [154].

Ebner et al. [33] described the computation of the interaction of a wave of shear-driven wall film with the gas phase based on the work done by Himmelsbach et al. [59] and Rosskamp et al. [119]. The gas phase was modeled with the standard model k- ε turbulence model and the liquid film was computed using finite difference method assuming a turbulent boundary layer near the wall. The waviness of the film was proposed by the sand grain roughness and the comparison of the simulation results with the experimental data showed good agreement [59]. Details of the effect of pressure gradient on the momentum exchange at the phase boundary are discussed in the research work of Ebner et al. [33].

Hashmi et al. [53] examined various CFD methods to simulate shear-driven wall films in the context of turbulent two-phase flow. The errors during calculating momentum exchange led to an incorrect prediction of the velocity profile and an overestimation of the pressure drop. An improvement in the prediction of turbulent velocity profiles over the channel height was achieved by the modification of the turbulence parameters at the interface. However, no general approach for simulation of shear-driven flows was found, since modeling the additional source term in the dissipation was still unclear. Gao et al. [42] utilized the k- ε turbulence model for simulating two-phase flows by avoiding the use of standard wall functions. The computed results were compared with the available published experimental data and were found to be in very good agreement. Researchers presented a correlation for calculating the pressure drop and the oil holdup based on their numerical results.

2.3 Objectives of the research work

Conclusions for further studies: From the above literature review, it can be concluded that no realistic theoretical approach is feasible due to the high complexity of the thin film flow under the effect of turbulent gas flow. Gas shear force can play an essential role in the formation of wavy films and secondary streams on heated walls. The mechanism of the effect of turbulent gas flow on the film waviness and its influence on heat transfer is still not well understood and requires a deeper study of the film thickness distribution through numerical procedures. These problems are the subject of the present research work. Therefore, two-phase flow modeling using the VOF method and the RANS approach for turbulent modeling are considered in the current research.

The analysis of the literature allows further identification and definition of the objectives of the current thesis work. The limited know-how about thermo-hydrodynamic mechanisms in gas-driven two-phase flows restricts the prediction of the wavy film and also the evaporation rate of liquid fuels. Thus, the objective of this study is to develop a numerical code to simulate turbulent two-phase flows coupled with heat transfer, validating the results against experimental data. Additionally, the influence of individual parameters by varying inlet conditions is explored. The present study is aimed at developing a new solver for convective heat transfer in shear-driven film flows within the 'OpenFOAM' framework. The following tasks are performed to meet the aim of the research project:

- Develop a numerical model to track the interface and take into account large variations in density (~1000:1) and viscosity across the interface
- Modify and implement the source code to account for the effects of heat transfer within two-phase flows
- Identify the parameters affecting wavy film on a heated wall and evaluate the wall liquid film flow characteristics of gas-driven films at high gas Reynolds numbers
- Implement and examine turbulence models in the solver code and study the effect of gas velocity on thin wall liquid film flows
- Study the influence of inlet flow parameters on the forced convective heat transfer mechanism

The present thesis work comprises three main development stages. The first is dedicated to developing an adiabatic solver without phase change, further modifying it to account for heat transfer and subsequent turbulence flow modeling. The solver is validated against theoretical data and experiments on shear-driven two–phase flows in rectangular channels. The second step is about comparing and analyzing the in-house measured data with further numerical analysis. The final stage consists of studying and executing a parametric study on the effect of various flow parameters.

3

Modeling of Turbulent Two-phase Flows

In this chapter, based on the project's objectives and the literature review, a description of the applied mathematical models is presented in the form of conservation equations and their source terms. In gas-driven two-phase flows, turbulence plays a vital role on the evolution of thin film surfaces. Therefore, the appropriate turbulence model is incorporated for both liquid and gas phases. The details of two equation turbulence modeling approach is described. The first section of this chapter describes conservation equations of mass, momentum, and energy followed by the interface capturing technique of two-phase laminar flows. Subsequently, the modeling of the surface tension force acting on the surface of the wavy film in contact with the gas is provided. Turbulence RANS modeling for stratified gas-liquid flows is described in detail. The chapter also presents equations for the modeling of turbulence in both phases. Finally, this section closes by discussing the near wall treatment for the low Reynolds number modeling approach.

3.1 Two-phase conservation equations

Two-phase flow is characterized by a moving interface between the phases, and the flow domain is divided into two separate regions. The presence of this interface increases the complexity of the problem over that of the single-phase flow. In this work, the interface capturing method is considered in two-phase flow modeling based on one-fluid formulation, where a single set of governing equations is solved. This one-fluid formulation takes into account the entire fluid flow domain as a single-phase flow field with varying thermo-physical properties across the interface. The single-phase governing equations are solved for each phase with additional source terms such as the surface tension force at the interface and the appropriate boundary conditions. The latter must be incorporated into the governing equations in order to describe the interaction between the gas and liquid phases.

In two-phase flow modeling, the governing equations describe the hydrodynamics and thermodynamics of fluids with the dependent local instantaneous variables such as velocity and temperature for each phase (see Figure 3.1). For the present case of study, the governing equations for fluid flow and heat transfer are continuity, momentum, and energy equations. In this

work, turbulence is described using the k- ε model. As a result, two scalar transport equations for turbulent kinetic energy k and the rate of dissipation ε are added to the governing equations [38]. The flow governing equations are based on the assumption that the two-phase fluids are Newtonian as well as incompressible and immiscible.

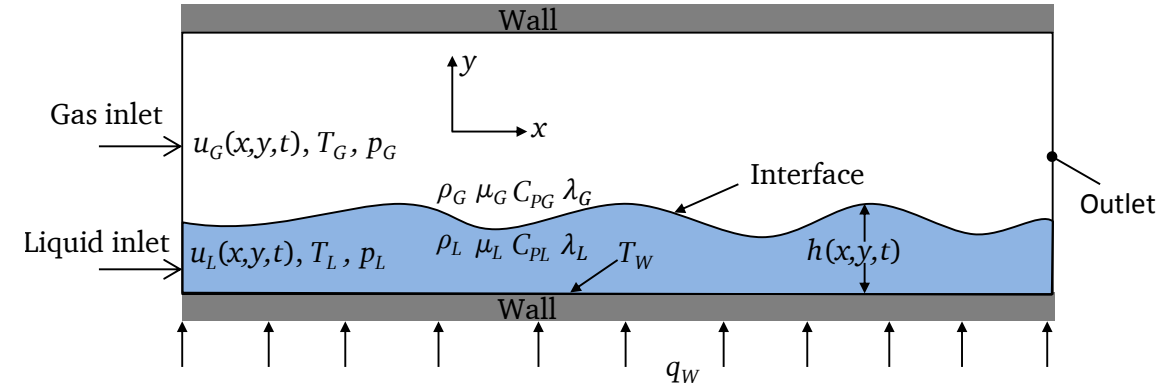

Figure 3.1: Schematic view of the physical model concerning the two-phase flow problem formulation

In order to track the interface, the Volume of Fluid (VOF) method initially developed by Hirt and Nichols [61] is employed to solve a single set of conservation equations in one fluid-formulation. In this chapter, conservation equations are initially derived in integral form and then provided in differential forms, which are used very often throughout this thesis. A brief overview of the VOF formulation with a description of one-fluid formulation is provided in Section 3.1.1.

3.1.1 VOF formulation

In order to identify the interface, an indicator or "color" function γ is introduced to indicate the fraction of a computational volume filled with the liquid or gas phase. An additional scalar transport equation for γ is introduced while computing the two-phase flows. This additional transport equation solves the quantity γ which accounts for the changing fluid properties in the interface region. In the VOF method, the indicator function is defined as the volume fraction γ based on the distribution of phases and the size of the computational volume:

$$\gamma = \frac{V_{Ph}}{V_{CV}}. \tag{3.1}$$

The variable V_{Ph} describes the volume fraction of the phase in each control volume V_{CV} and indicates this by using the values between zero and one in a single computational cell (Figure 3.2). The volume fraction γ has no physical significance but is considered as a numerical property. It is a scalar variable and serves to identify the gas-liquid phases in the fluid domain.

$$\gamma = \begin{cases} 1 & \text{for a control volume filled with fluid 1,} \\ 0 < \gamma < 1 & \text{for a control volume filled with two fluids,} \\ 0 & \text{for a control volume filled with fluid 2} \end{cases} \tag{3.2}$$

Although it would ideally be sharp, the interface between the phases in the VOF method is smeared across grid cells. In the phase boundary area, these grid cells must be maintained at the smallest possible size to minimize such smearing (a process known as false diffusion). However, this leads to a high increase in computational time for unsteady simulation.

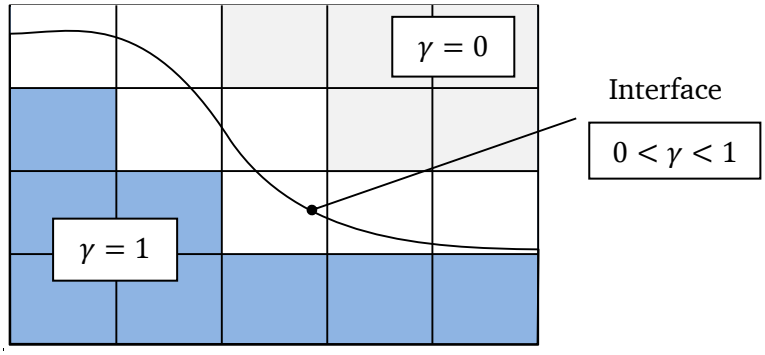

Figure 3.2: VOF methodology by coloring the fluid domain by the volume fraction

The temporal evolution of the indicator function for an incompressible flow field is described by the following equation,

$$\frac{\partial \gamma}{\partial t} + \nabla \cdot (\gamma u) = 0. \tag{3.3}$$

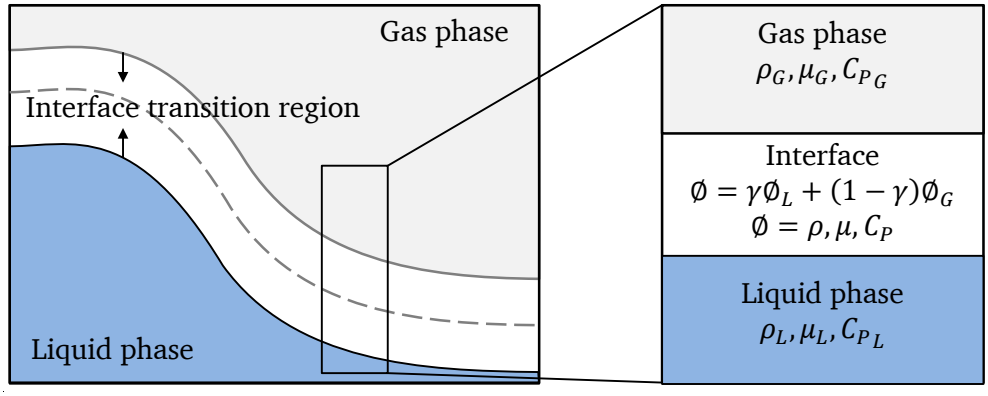

Figure 3.3: Schematic view of the interfacial region in the VOF method and the properties in each cell in two-phase flows [61]

In the two-phase flow system, the properties appearing in the conservation equations are determined by the distribution of the phases in each control volume depending on the phase indicator. If the volume fraction of the liquid phase is known, the properties of the fluid are computed by the following expression:

$$\emptyset = \gamma\emptyset_L + (1-\gamma)\emptyset_G, \tag{3.4}$$

where $\emptyset$ stands for each physical property of the fluid mentioned above, the subscript L denotes the liquid phase, and subscript G is used for the gas phase (see Figure 3.3).

Modified VOF equation

The computation of the volume fraction is crucial during the simulation of high-density ratio fluids such as water and air, where small errors on the volume fraction generate significant errors due to smearing. In order to avoid such issues, many researchers have proposed numerous alternative methods [141, 142]. In the present approach, an additional term is incorporated into the VOF equation (3.3). This term allows the reconstruction of the interface to be avoided and ensures the boundedness of the phase fraction. This modified VOF equation is expressed with an additional convective term derived from the weighted average of individual phase velocities.

The modified VOF equation is derived through the following two individual γ equations of the gas and liquid phases:

$$\frac{\partial\gamma}{\partial t} + \nabla\cdot(\gamma u_L) = 0, \tag{3.5}$$

$$\frac{\partial(1-\gamma)}{\partial t} + \nabla\cdot[u_G(1-\gamma)] = 0. \tag{3.6}$$

In the above equations, subscripts L and G denote the liquid and gas phases respectively. The Equation (3.5) is re-arranged in terms of the gas and liquid phase velocities as follows:

$$\frac{\partial\gamma}{\partial t} + \nabla\cdot\left[u_L\gamma + \underbrace{\gamma(u_L\gamma) - \gamma(u_L\gamma)}_{=0}\right] + \nabla\cdot\left[\underbrace{\gamma(1-\gamma)u_G - \gamma(1-\gamma)u_G}_{=0}\right] = 0, \tag{3.7}$$

$$\frac{\partial\gamma}{\partial t} + \nabla\cdot\left[\gamma\underbrace{\{\gamma u_L + (1-\gamma)u_G\}}_{=u}\right] + \nabla\cdot\left[\left(\underbrace{u_L - u_G}_{=u_C}\right)\gamma(1-\gamma)\right] = 0. \tag{3.8}$$

In the Equation (3.8), $u_C = u_L - u_G$ is commonly referred to as the compression term, which is the phase relative velocity and vanishes in individual phases except at the phase interface [13, 22]. This compression velocity is used to maintain a sharp interface and minimize numerical smearing. In the above equation, an artificial supplementary velocity field u_C is defined in the vicinity of the interface. The field is defined in such a way that the local flow steepens the gradient of the volume fraction function, resulting in an improved interface resolution. This results in an improved interface resolution. The final modified VOF equation adopted in the current study to capture the gas-liquid interface is:

$$\frac{\partial \gamma}{\partial t} + \nabla \cdot (\gamma u) + \underbrace{\nabla \cdot \left(u_C \gamma (1-\gamma)\right)}_{\text{Interface compression}} = 0. \tag{3.9}$$

The third term in the above expression on the left side is added artificially to reduce numerical diffusion and has no physical significance. This term only plays an important role in the interface region. Rusche [122] introduced this methodology to preserve the interface sharpness, which is important in the VOF approach [122]. The modified VOF formulation ensures the sharp gradient of the indicator function γ without any geometric reconstruction at the interface region. The modified VOF equation explicitly accounts for the topology of the interface by reducing numerical diffusion at the interface [13]. The velocity at the interface region is assumed with a weighted average of the velocity between the two phases and can be determined as:

$$u = \gamma u_L + (1-\gamma) u_G. \tag{3.10}$$

3.1.2 Mass conservation equation

The mass conservation equation for an infinite control volume dV in a fixed space with the difference between the entering and outgoing mass flow at each time interval and the variable density ρ can be expressed as:

$$\frac{\partial \rho}{\partial t} + \frac{\partial (\rho u_i)}{\partial x_i} = 0, \tag{3.11}$$

where u_i and x_i are the velocity component and spatial coordinate in the direction of i (i = 1, 2 and 3), t is the time. The first term in the above equation is a transient density variation within the control volume, while the second term is the net mass flow through the surface enclosing the control volume. A schematic representation of mass conservation in two-phase flows is shown in Figure 3.4. In the two-phase flow problem, the local gas and liquid densities are evaluated using the indicator function γ (Equation 3.4).

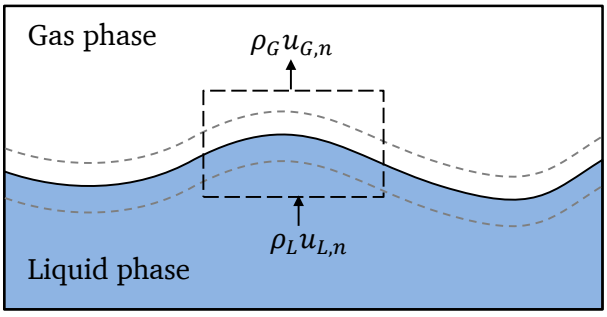

Figure 3.4: Interfacial characteristics of the control volume for the conservation of mass at the gas-liquid interface [22]

3.1.3 Momentum conservation equations

In gas-driven liquid flows, the viscosity of the gas phase affects the boundary layer near the interface, and the interface shear determines the evolution of interface. For the modeling of such two-phase flows, the inertia force as well as the viscosity of the gas and the liquid must be considered. The surface tension force is a specific term in two-phase flows, which tends to minimize the surface area of the interface, and is therefore vital for accurately modeling interfacial topology.

The transient variation of the momentum is equal to the sum of the volume and surface forces acting in the control volume dV. The momentum balance equation comprises three equations for the x, y, and z components, and it represents a vector equation. The conservation of the momentum equation can be expressed in one-fluid formulation. The momentum equation is expressed in the following:

$$\frac{\partial \rho u_i}{\partial t} + \frac{\partial (\rho u_i u_j)}{\partial x_j} = -\frac{\partial p}{\partial x_i} + \frac{\partial \tau_{ij}}{\partial x_j} + \rho g_i + F_{si}, \tag{3.12}$$

$$\tau_{ij} = \mu \left[\left(\frac{\partial u_i}{\partial x_j} + \frac{\partial u_j}{\partial x_i} \right) - \frac{2}{3} \mu \frac{\partial u_k}{\partial x_k} \delta_{ij} \right]. \tag{3.13}$$

In the above equations, p denotes the pressure, μ is the dynamic viscosity and ρ denotes the density of the fluid, t is the time, x is the cartesian coordinate and u is the velocity vector. The term δ_{ij} called the Kronecker symbol is equal to the value 1 with the same indices and otherwise 0. In the momentum equation (3.12), the first term on the left-hand side describes the time variation of velocity, and the second term is the convective term representing the momentum flux across the control volume. As mentioned before, the right-hand side of the equation represents the sum of the volume and surface forces acting on fluid. The first term on the right hand side denotes the pressure term, while the second term denotes the viscous force acting directly on the surface of the control volume. The last terms on the right hand side represent body forces such as gravitational acceleration and the external force per unit volume. The forces involved in two-phase flows considered in this current research are summarized in Table 3.1. The term L defined in the force terms is the characteristic length.

Table 3.1: Summary of forces in two-phase flows and their magnitude

Force	Magnitude of force per unit volume
Pressure force	Surface force $\sim \Delta p L^{-1}$
Inertia force	Volume force $\sim \rho u^2 L^{-1}$
Viscous force	Surface force $\sim \mu u L^{-2}$
Gravity force	Volume force $\sim g\rho$
Surface tension force	Line force $\sim \sigma L^{-2}$

The balance of forces in a two-phase flow system is shown in Figure 3.5. The source term F_s in Equation (3.12) represents the source of momentum due to the surface tension force, which can be modeled using the CSF model [17]. The details related to the CSF model are discussed in Section 3.2. In this work, gas-liquid phases are treated as incompressible since the Mach number associated with gas at maximum velocity is low, thus the second term in Equation (3.13) is neglected. The density ρ in the momentum equation depends on the volume fraction γ (Equation 3.4).

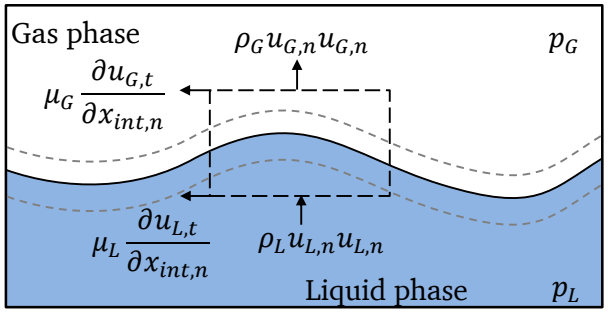

Figure 3.5: The conservation of momentum at the gas-liquid interface [22]

3.1.4 Energy conservation equation

The energy equation describes the conservation of energy generated by flow dynamics, temperature gradients, and heat sources in the system. The energy equation is expressed as:

$$\frac{\partial(\rho C_p T)}{\partial t} + \frac{\partial(\rho C_p u_j T)}{\partial x_j} = \frac{\partial}{\partial x_j}\left(\lambda \frac{\partial T}{\partial x_j}\right) + S_h\,, \tag{3.14}$$

where λ is thermal conductivity, C_p is heat capacity of the fluid, and its value at the interface depends locally on the volume fraction variable γ (Equation 3.4).

The variations of the remaining variables (ρ and μ) at the interface have already been mentioned. The above Equation (3.14) is the form of the energy equation representing the generic scalar transport of heat equation. The first part of Equation (3.14) is the transient term while the second part represents convective heat transfer. The first term in the right-hand side of the equation is the heat conduction and the last term S_h includes the source of the phase change and chemical reaction. This last term is neglected as the simulations described in this thesis do not have any phase change. The conservation of energy transport at the gas-liquid interface is shown schematically in Figure 3.6. The fluids considered in this thesis are air and water, and constant thermal properties are assumed for both.

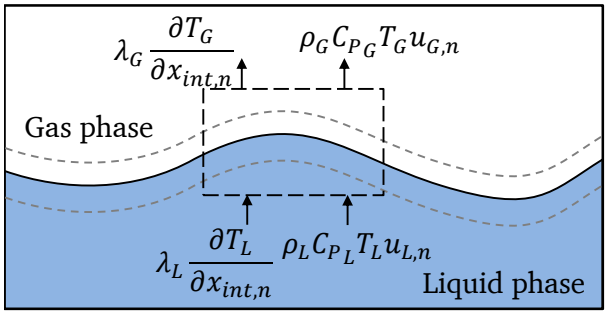

Figure 3.6: The conservation of energy transport at the gas-liquid interface [22]

3.2 Surface tension force modeling

In stratified two-phase flows, attraction forces between the molecules cause the rise of a surface tension effect along an interface. The surface tension force acts to minimize the interfacial area and affects the interface shape. The implementation of the surface tension force is important, because it creates a pressure jump across a curved surface. The influence of the surface tension exerted at the phase boundary of the flow must be taken into account in the momentum equations by describing the two-phase flow. The surface tension force acts to balance the pressure difference in both the fluids on either side of the interface and it is expressed by the Young-Laplace's formula:

$$\Delta p = p_L - p_G = \sigma\kappa. \tag{3.15}$$

In the above expression, Δp is the pressure drop across the surface, κ is the mean curvature, and σ is the surface tension coefficient, which is defined as the amount of work necessary to create a unit area of free surface. Its value is always positive for immiscible fluids and determined by the nature of the fluids. The mean curvature κ is defined by:

$$\kappa = \left(\frac{1}{R_G} + \frac{1}{R_L}\right), \tag{3.16}$$

where R_G and R_L are the principal curvature radii in orthogonal directions.

The pressure is discontinuous at the interface. In order to overcome this discontinuity, Brackbill and co-workers proposed a Continuum Surface Force (CSF) model [17]. This CSF model is the volumetric force caused by surface tension acting on the gas-liquid interface, and it is defined in a direction normal to the interface (see Figure 3.7). In this model, the pressure is expected to rise within the transitional region between fluids with the same smoothness as the indicator function γ.

In the CSF approach, the interface transitional area is divided into several layers according to the definition of indicator function γ. The surface tension force direction depends on the normal vector on the interface, and its magnitude depends on the interface curvature. The unit normal vector of each layer in the transitional domain is determined by the gradient of the indicator function γ.

$$\overrightarrow{n^*} = \frac{\nabla\gamma}{|\nabla\gamma|} \tag{3.17}$$

The gradient of the indicator function $\nabla\gamma$ is a continuous function which is zero everywhere in the two-phase flow domain except in the interfacial region. The interfacial curvature can be expressed in terms of the divergence of the unit normal vector from the interface, which is expressed as follows:

$$\kappa = \nabla \cdot \frac{\nabla\gamma}{|\nabla\gamma|}. \tag{3.18}$$

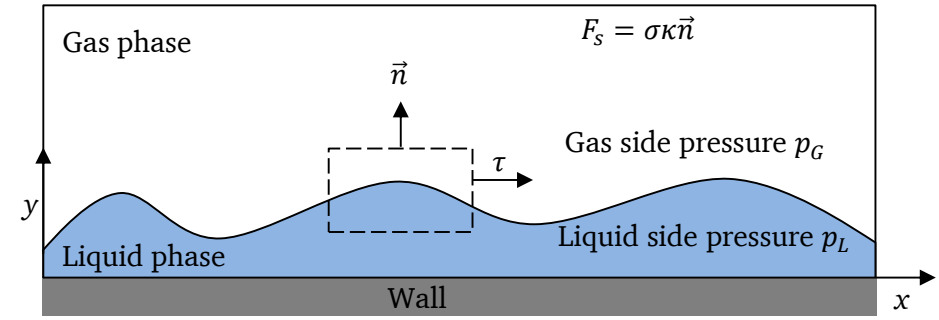

Figure 3.7: Sketch of a wavy film with forces acting on the surface in the CSF model [17]

The surface tension value (for water) is considered constant during simulation, since it does not vary much between temperatures of 60°C to 80 °C. In this CSF formulation, the additional source term F_s with constant surface tension σ in the momentum equation (3.12) is used, which is expressed by the following equation:

$$F_s = \sigma\kappa\vec{n} = \sigma\left(\nabla \cdot \frac{\nabla\gamma}{|\nabla\gamma|}\right)\nabla\gamma. \tag{3.19}$$

3.3 Two-phase turbulence modeling

In gas-driven liquid film flows, turbulence plays an important role since it significantly influences the mass, momentum and energy transfer rates between turbulent gas and the liquid film. It is characterized by the fluctuating gas phase velocity at high Reynolds numbers. There is no analytical solution for the governing equations of complex flows containing all turbulence properties. Turbulence modeling is important and challenging to precisely predict two-phase flows due to complex interface dynamics compared to single-phase flows. In order to model a turbulent two-phase flow, a two-equation turbulence model approach is employed in this approach with a modification to account for the near wall boundary layer. In this research, single-phase k-ε turbulence models with two additional equations, turbulent kinetic energy and turbulent

dissipation, are applied to each phase. In the following sub-chapter, the characteristics of two-phase flow turbulence and details of the RANS modeling approach are described.

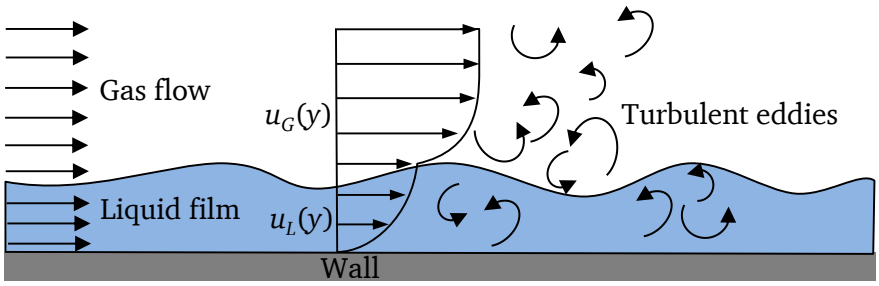

Figure 3.8: Schematic of the flow structure in two-phase flow with small and large eddies as well as deformations near the gas-liquid interface [140]

3.3.1 Characteristics of two-phase flow turbulence

In gas-driven liquid flows, turbulence is generated by the presence of gas shear on the liquid interface leading to fluctuations of the interface boundary at high Reynolds numbers. The turbulent flow phenomenon of two-phase flow depends on the inertia of the driven gas, the structure of the flow, and geometry. An illustration of the fluctuating gas-liquid interface is shown in Figure 3.8. Beyond the critical value of the Reynolds number, the inertial forces are more dominant than the viscous forces and the flow becomes unstable, tending to produce chaotic eddies and vortices. Turbulence in two-phase flows is characterized by velocity unsteadiness, a three-dimensional structure, randomness, and dissipativeness. The wavy liquid film instabilities cause various sizes of eddies in the gas phase. The kinetic energy of the larger eddies is transferred among other eddies due their interaction, finally dissipating into the smallest scale of eddies. These eddies fluctuate randomly, causing rapid variations of flow properties which need to be modeled appropriately via numerical formulation. The largest eddies are up to several orders of magnitude while the smallest eddies are at Kolmogorov length scales. The size of the Kolmogorov length scale l_η can be obtained by using kinematic viscosity ν and the dissipation rate of turbulent kinetic energy ε:

$$l_\eta = \left(\frac{\nu^3}{\varepsilon}\right)^{1/4}. \tag{3.20}$$

In a similar way, a Kolmogorov time scale is determined by the square root of the ratio of ν and ε:

$$\tau = \left(\frac{\nu}{\varepsilon}\right)^{1/2}. \tag{3.21}$$

In the above expressions, the dissipation rate of turbulent kinetic energy ε is the function of velocity, containing the integral scale of an eddy (l), which is equal to u^3 / l.

The above expressions are very important for the computation of turbulent flows, because they imply that the Kolmogorov length scales must be resolved in a Direct Numerical Simulation (DNS) of the Navier-Stokes equations (or, in other words, when Navier-Stokes equations of turbulent flows are solved numerically without any modification). The DNS technique resolves time and length scales directly in a turbulent flow. The greatest problem faced by turbulent flow simulation is the resolution of the high-frequency fluctuations requiring a very fine numerical grid and considerably smaller time steps. Thus, the number of grid points required to resolve the smallest Kolmogorov scales (l_η) up to the integral scales (l) in one direction can be estimated for a single time step by the following expression:

$$N = \frac{l}{l_\eta} = Re^{3/4}\,. \tag{3.22}$$

While in a three-dimensional problem, it can be estimated as,

$$N = \left(\frac{l}{l_\eta}\right)^3 \sim \left(\frac{ul}{\nu}\right)^{9/4} = Re^{9/4}\,. \tag{3.23}$$

The number of grid points required in DNS is very large for high Reynolds number flows, and the number of time steps required is the cube of the Reynolds number, thus greatly increasing computational costs. Hence, DNS is limited to simple geometries for low Reynolds numbers even with high performance computing resources.

Crowe et al. [24] described the possibilities of turbulence models for two-phase flow calculations. The main turbulent modeling techniques available for solving two-phase flows are Large Eddy Simulations (LES) and Reynolds-Averaged Navier-Stokes models (RANS). In the LES approach, large eddies transporting major shares of the kinetic energy are resolved explicitly. Small scale eddies are dissipative in nature and modeled using sub-grid scale formulations (SGS) [115]. Therefore, LES still requires high computing power for two-phase flow problems at high Reynolds numbers. In the RANS turbulence modeling approach, the flow variables are time-averaged, reducing the numerical efforts significantly with reasonable accuracy. The additional unknown terms in the momentum and energy equations are referred to as Reynolds stresses, and they can be modeled by way of two-equation eddy viscosity models. A single-phase two-equation model is considered as a basis for the two-phase turbulence models. In the case of two-phase flow, a two-equation model of single-phase turbulence is solved for each phase via the VOF variable γ. Within the scope of this research work, the RANS approach is adopted for the two-phase flows, and the details are discussed in Section 3.3.2.

3.3.2 RANS modeling

As previously mentioned, turbulent flows are characterized by strong spatial and temporal fluctuations and these fluctuations result in mixing at high frequency. In order to obtain the governing equations of a turbulent two-phase flow in the framework of RANS modeling, the approach is to decompose the variables into an averaged part and a fluctuation as in the

conventional Reynolds averaging in single-phase flow. However, the number of unknowns eventually becomes greater than the number of equations, resulting in a closure problem. Therefore, the choice of a turbulence model depends upon the physical phenomena happening in the problem, the level of accuracy required, and the time available. Navier-Stokes equations are averaged with respect to time, and the unsteady behavior of the turbulent flow is completely neglected when considering the effects of fluctuations on the mean flow. Using Reynolds-Averaged Navier-Stokes equations, continuity and energy equations in the simulations are a state of the art approach for investigating two-phase flows with heat transfer. The numerical treatment of a turbulent two-phase flow with a RANS approach is based on the same principle as that for single-phase flows. Hence, the numerical details of RANS modeling are discussed for the single-phase flow in the following section.

Reynolds-averaged conservation equations

In the RANS approach, each transport flow quantity $\emptyset$ is split into its time-averaged value $\overline{\emptyset}$ and into its fluctuation value $\emptyset'$ [92]. Such splitting of turbulent fluctuating variables is called Reynolds averaging. The flow quantity $\emptyset$ can either be velocity component, pressure or temperature. Therefore, a variable $\emptyset$ is defined as the sum of its mean value and its fluctuating value:

$$\emptyset = \overline{\emptyset} + \emptyset' . \tag{3.24}$$

The use of time averaging is described as the temporal average. The time average of a variable is defined by:

$$\overline{\emptyset} = \lim_{\Delta t \to \infty} \frac{1}{\Delta t} \int_{t}^{t+\Delta t} \emptyset dt , \tag{3.25}$$

with Δt as a time scale that is much larger than the largest time scale of turbulent fluctuations, so that the mean value is independent of time. This kind of averaging is applicable to stationary turbulence.

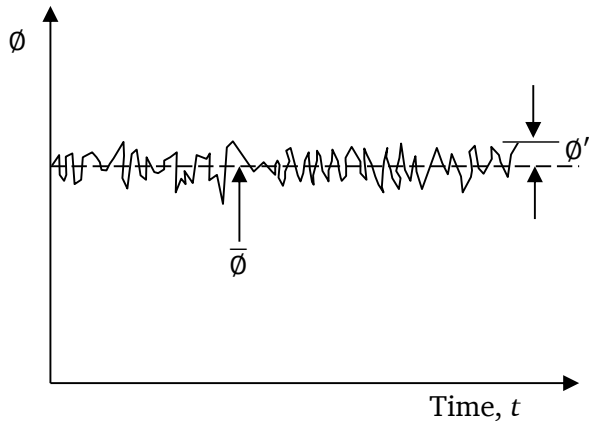

Figure 3.9: Statistical averaging of the fluctuation velocity $\emptyset'$ with time in turbulent flow [148]

The application of such averaging processes on the dependent variable of the Navier-Stokes equations leads to the so-called Reynolds-averaged equations. This results in the time-averaged equations for incompressible flows for the mass, momentum, and energy conservations. The Reynolds-averaged continuity equation is basically identical to the continuity equation without new additional terms. However, additional flux terms arise in the momentum and energy equations. The Reynolds-averaged momentum and energy equations obtained by time-averaging Equations. (3.11), (3.12) and (3.14) are expressed as follows:

$$\frac{\partial \rho}{\partial t} + \frac{\partial (\rho \bar{u}_i)}{\partial x_i} = 0 \,, \tag{3.26}$$

$$\frac{\partial \rho \bar{u}_i}{\partial t} + \frac{\partial (\rho \bar{u}_i \bar{u}_j)}{\partial x_j} = -\frac{\partial \bar{p}}{\partial x_i} + \frac{\partial}{\partial x_j}\left(\mu\left[\frac{\partial \bar{u}_i}{\partial x_j} + \frac{\partial \bar{u}_j}{\partial x_i}\right] - \rho\overline{u_i' u_j'}\right) + \rho g_i + F_{si} \,, \tag{3.27}$$

$$\frac{\partial (\rho C_p \bar{T})}{\partial t} + \frac{\partial (\rho \bar{u}_j C_p \bar{T})}{\partial x_j} = \frac{\partial}{\partial x_j}\left(\lambda \frac{\partial \bar{T}}{\partial x_j} - \rho\overline{C_P T' u_j'}\right). \tag{3.28}$$

The averaging procedure of Navier-Stokes equations due to the turbulent motion yields additional unknown terms $\rho\overline{u_i' u_j'}$ and $\overline{C_P T' u_j'}$, which represent the Reynolds stresses and turbulent heat fluxes, respectively. During the averaging procedure of the Navier-Stokes equations process, no new equations have been introduced. The Reynolds stress tensor $\rho\overline{u_i' u_j'}$ in Equation (3.27) has the form of the symmetric tensor of the second order and consists of six additional unknown variables. This Reynolds stress tensor is modeled based on the eddy viscosity approach with turbulent viscosity multiplied by velocity gradients based on the Boussinesq assumption. Therefore, the turbulent contribution term can be expressed as:

$$-\rho\,\overline{u_i' u_j'} = \mu_t \left[\frac{\partial u_i}{\partial x_j} + \frac{\partial u_j}{\partial x_i}\right] - \frac{2}{3}\rho k \delta_{ij} \,. \tag{3.29}$$

The term turbulent viscosity μ_t, also called eddy viscosity is not a material constant but does depend on the local state of turbulence and local flow conditions [60, 84]. The term δ_{ij} is the Kronecker symbol ($\delta_{ij} = 1$ if $i = j$ and $\delta_{ij} = 0$ otherwise) and k is the turbulent kinetic energy given by:

$$k = \frac{1}{2}\,\overline{u_i' u_i'}. \tag{3.30}$$

Turbulent Prandtl number

Turbulence in the flow influences the momentum transfer as well as the energy transport. The term $\overline{C_P T' u_j'}$ in Equation (3.28) characterizes the turbulent diffusion energy flux that is causing

three additional unknown variables which are modeled analogous to the momentum equation in terms of the turbulent Prandtl number Pr_t.

$$\underbrace{\rho C_p \frac{v}{Pr}\frac{\partial \bar{T}}{\partial x_j}}_{Viscous} - \underbrace{\rho\overline{C_P T' u_j'}}_{Turbulent} = \lambda\frac{\partial \bar{T}}{\partial x_j} - \frac{\mu_t}{Pr_t}\frac{\partial (C_P\bar{T})}{\partial x_j}, \tag{3.31}$$

$$-\rho\overline{C_P T' u_j'} = \frac{\mu_t}{Pr_t}\frac{\partial (C_P\bar{T})}{\partial x_j}. \tag{3.32}$$

The definition of the turbulent Prandtl number is given by:

$$Pr_t = \frac{C_P\mu_t}{\lambda_t}. \tag{3.33}$$

In the above definition, λ_t is the turbulent thermal conductivity. The turbulent Prandtl number is not based on material properties but depends on flow characteristics. The current research work assumed a constant value $Pr_t = 0.9$ [94]. The assumption of a constant value for the turbulent Prandtl number Pr_t in the k- ε model approach is used frequently to predict heat transfer in separating and reattaching turbulent flows [83].

The final momentum and energy equations after substituting an effective eddy viscosity ($\bar{\mu}_{eff} = \bar{\mu} + \bar{\mu}_t$) and the effective turbulent thermal conductivity ($\lambda_{eff} = \lambda + \lambda_t$) are given by:

$$\frac{\partial \rho\bar{u}_i}{\partial t} + \frac{\partial(\rho\bar{u}_i\bar{u}_j)}{\partial x_j} = \frac{\partial}{\partial x_j}\left[\underbrace{(\bar{\mu} + \bar{\mu_t})}_{\mu_{eff}}\left(\frac{\partial \bar{u}_i}{\partial x_j} + \frac{\partial \bar{u}_j}{\partial x_i}\right)\right] - \frac{\partial}{\partial x_i}\left(\bar{p} + \frac{2}{3}\rho k\right) + \rho g_i + F_{si}, \tag{3.34}$$

$$\frac{\partial(\rho C_p\bar{T})}{\partial t} + \frac{\partial(\rho C_p\bar{u}_i\bar{T})}{\partial x_j} = \frac{\partial}{\partial x_j}\left(C_P\left[\frac{\mu}{Pr} + \frac{\mu_t}{Pr_t}\right]\frac{\partial \bar{T}}{\partial x_j}\right). \tag{3.35}$$

The term turbulent viscosity μ_t in RANS equations for averaged velocity, pressure, and energy cannot be solved directly. The approximations introduced to solve these unknowns in terms of known quantities are called turbulence models. These are usually obtained from the empirical or semi-empirical correlations, which are applicable within limits to the specific geometries and ranges of Reynolds numbers. Based on the complexity of the flow problem, turbulence models are applied to calculate the turbulent viscosity μ_t. This indicates that additional equations must be solved to determine μ_t. In the literature, there are zero, one, and two equations models that are employed for turbulence modeling with an assumption of isotropic turbulence. The zero-equation turbulence modeling approach is based on the turbulence length scale l, with an assumption of constant viscosity [115]. In the one-equation modeling approach, a single equation is used to describe the transport of the turbulent fluctuations by relating to time-averaged kinetic energy.

The two-equation k- ε model is the most common and most popular turbulence model proposed by Launder and Spalding [69, 84]. In this thesis, the k- ε model is preferred because of its stability calculations, and because it is particularly applicable to highly turbulent flows with reasonable

accuracy at low computational efforts. In this approach, the turbulent viscosity μ_t is determined with an assumption of isotropic turbulence. The former is modeled as a product of turbulent velocity u_t, and length scale l for the local conditions in a flow. The resulting turbulent viscosity can be calculated according to the following relation [148]:

$$\mu_t = \rho u_t l = C_\mu \rho \frac{k^2}{\varepsilon}. \tag{3.36}$$

In the above relation, C_μ has an empirically derived constant value of 0.09. The specific turbulent kinetic energy k and for the dissipation ε are determined by solving relevant transport equations [85]. A detailed description of the two-equation turbulence model is presented in Section 3.3.3.

RANS k-ε equations

The k- ε turbulence model belongs to the two-equation class of turbulence models with transport equations for kinetic energy of turbulence k and dissipation rate of turbulence ε. The first transport equation in this model, the turbulent kinetic energy k of the fluctuating motion is [152]:

$$\underbrace{\frac{\partial(\rho k)}{\partial t}}_{Transient} + \underbrace{\frac{\partial(\rho \bar{u}_j k)}{\partial x_j}}_{Convection} = \underbrace{\frac{\partial}{\partial x_j}\left[\left(\mu + \frac{\mu_t}{\sigma_k}\right)\frac{\partial k}{\partial x_j}\right]}_{Diffusion} + \underbrace{\mu_t\left(\frac{\partial \bar{u}_i}{\partial x_j} + \frac{\partial \bar{u}_j}{\partial x_i}\right)\frac{\partial \bar{u}_i}{\partial x_j}}_{Production} - \underbrace{\rho\varepsilon}_{Destruction}. \tag{3.37}$$

The first term in the above equation describes the rate of change for the turbulent kinetic energy. The second term represents the convective transport of the turbulent energy. The first term on the right side is the diffusion term, while the second term there describes the turbulence production. This production term is responsible for the transfer of energy from the mean flow to the turbulence that is also modeled using the eddy viscosity approach. The last term describes the destruction of turbulence through the dissipation of energy into heat due to the viscous nature of the flow.

The second transport equation for ε is solved to describe the turbulent length scales, which is similar to the k equation. The turbulent dissipation rate ε can be determined by solving the following equation:

$$\frac{\partial(\rho\varepsilon)}{\partial t} + \frac{\partial(\rho \bar{u}_j \varepsilon)}{\partial x_j} = \frac{\partial}{\partial x_j}\left[\left(\mu + \frac{\mu_t}{\sigma_\varepsilon}\right)\frac{\partial \varepsilon}{\partial x_j}\right] + C_{1\varepsilon}\frac{\varepsilon}{k}\mu_t\left(\frac{\partial \bar{u}_i}{\partial x_j} + \frac{\partial \bar{u}_j}{\partial x_i}\right)\frac{\partial \bar{u}_i}{\partial x_j} - C_{2\varepsilon}\rho\frac{\varepsilon^2}{k}. \tag{3.38}$$

In the above equations, $C_{1\varepsilon}$, $C_{2\varepsilon}$, σ_k, σ_ε are constants which are derived empirically. The standard k-ε model has five empirical constants presented in Table 3.2 [148].

Table 3.2: Coefficient values of the k-ε model [148]

Constant	Value
$C_{1\varepsilon}$	1.44
$C_{2\varepsilon}$	1.92
C_{μ}	0.09
σ_k	1.00
σ_{ε}	1.30

3.3.3 Flow modeling near the wall

In gas-driven liquid film flows, velocity, temperature, and turbulence distributions can be resolved through the same procedure with which they are solved in single-phase flows. The near wall flow modeling is of major concern because the walls are the main source of turbulence. The velocity and pressure gradients are high near the wall, significantly influencing the hydrodynamics. Transport processes with large gradients of momentum and scalar transport variables occur most vigorously near the wall region due to the viscous effects. These are caused by the viscous friction near the wall. They recede when moving away from the wall while turbulent fluctuations become dominant. The velocity profile for turbulent flows is flattened compared to the laminar flow in the channel. Further, the near-wall region can be sub-divided into three sub-regions, namely: the viscous sub-layer, the buffer layer, and the fully turbulent region. This categorization is based on both experiments and mathematical analysis [151]. Figure 3.10 illustrates these typical three subdivisions of the near-wall region, which are plotted on semi-logarithmic axes corresponding to the dimensionless velocity u^+ and the dimensionless distance y^+.

The dimensionless distance y^+ from the wall is defined by the following relation:

$$y^+ = \frac{\rho u_t y_P}{\mu} = \frac{\rho C_{\mu}^{1/4} \left(k|_{y\to 0}\right)^{1/2} y_P}{\mu}, \tag{3.39}$$

where, y_P is the distance from a cell center point to the wall and the turbulent velocity u_t is defined from the wall shear stress τ_w.

$$u_t = \sqrt{\tau_w/\rho}\,. \tag{3.40}$$

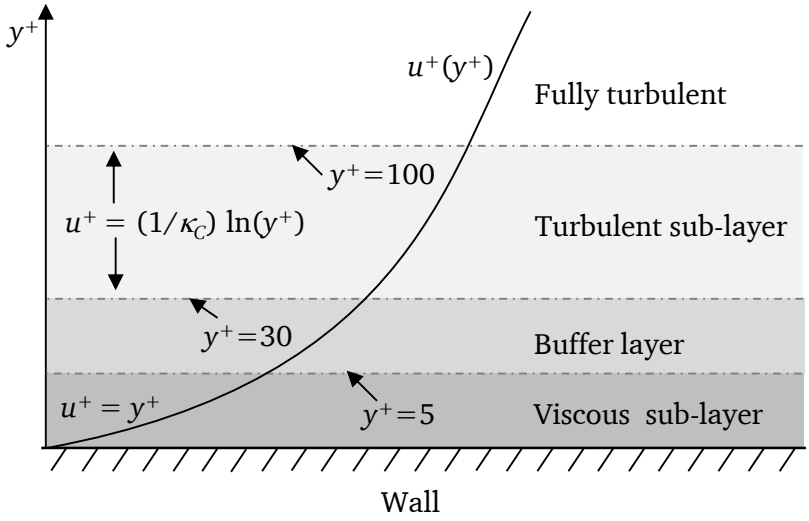

Figure 3.10: Schematic of the inner region of a fully developed turbulent boundary layer [151]

The layer immediately adjacent to the wall is called the viscous sub-layer ($0 < y^+ < 5$). In this region, turbulent fluctuation is negligible and the viscous forces are dominant. The flow is laminar while the molecular viscosity plays a major role in calculating the momentum and heat transfer. The velocity gradient is sharp in this region, and the velocity distribution close to the wall indicates the linear relationship [148]:

$$u^+ = y^+, \tag{3.41}$$

$$u^+ = \frac{uC_\mu^{1/4}\left(k|_{y\to 0}\right)^{1/2}}{\tau_w/\rho}. \tag{3.42}$$

The region ($5 < y^+ < 30$) between the laminar viscous sub-layer and the logarithmic layer is called the buffer region. In this region, the effects of molecular viscosity and turbulent stresses are in equilibrium. Beyond this buffer region, which is further away from the wall, turbulent fluctuations dominate. Inertial forces dominate the region extending away from $y^+ > 30$. This region is called the log-law region [151]. In this fully turbulent region, the dimensionless mean velocity u^+ distribution can be expressed using the Logarithmic Law:

$$u^+(y^+) = \frac{\bar{u}}{u_t} = \frac{1}{\kappa_C} ln(y^+) + C^+. \tag{3.43}$$

Here, κ_C denotes the von Karman constant ($\kappa_C \approx 0.42$), and C^+ is the integration constant, which is estimated from measurements to be at a value of 5.0.

3.3.4 Low Reynolds number k-ε model

There are two approaches to modeling the near wall region. In the first approach, the viscosity-affected inner region is not resolved completely. Instead, the empirical formulas are used to assume the variables such as velocity, pressure, and temperature in the near wall region (turbulence boundary layer). Such types of empirical formulas are called 'wall functions' and represent the local profiles of the velocity in the boundary layer to formulate turbulent kinetic energy and turbulent dissipation energy. These wall functions are applied on a grid point within the logarithmic region ($y^+ > 30$) and used to bridge the turbulent regions with the viscous sub-layer. The standard wall functions are used to approximate the turbulence quantities near the walls mostly in single-phase flows [85]. The major drawback of this approach is that the boundary layer next to the wall region is not solved because the whole film can be inside this unresolved region. Therefore, the standard k- ε model with wall functions cannot be considered for two-phase wall liquid film flows with heat transfer. An alternative type of modeling known as the Low-Reynolds number model makes it possible to resolve the boundary layer in the viscous sub-layer.

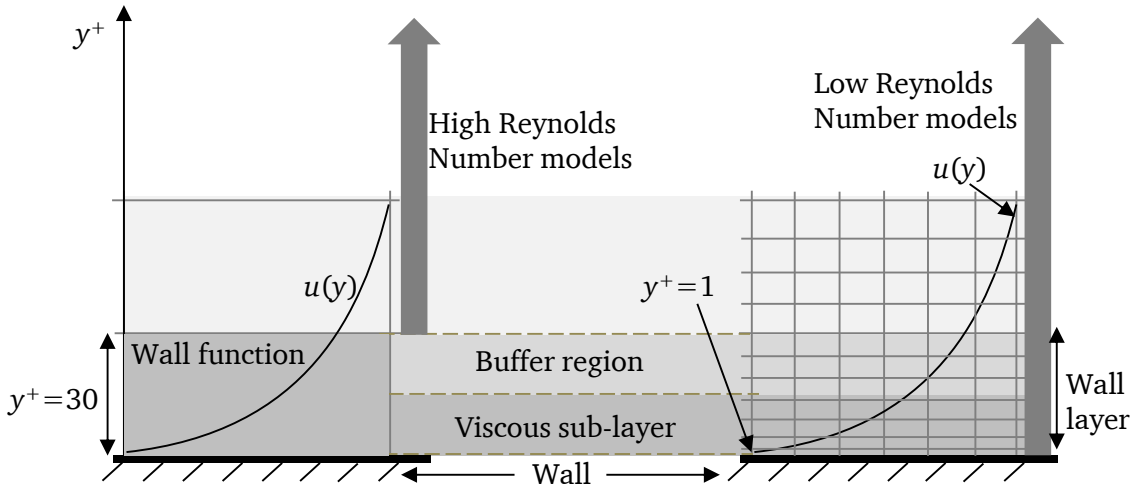

Figure 3.11: Schematic of the mesh density with respect to the first computational cell in the turbulent boundary layer for the RANS simulation. The wall function approach (left) for high Reynolds number model and the near wall grid refinement approach for Low-Reynolds number model (right) [148]

In the Low-Reynolds number model, the viscosity-affected near-wall region is completely solved up to the viscous sub-layer. This approach requires a very fine grid resolution next to the wall zone. Hence, the first near wall element typically maintained a value of $y^+ \sim 1$. A schematic representation of both approaches is presented in Figure 3.11. In order to predict the velocity field in the turbulent boundary layer, including the viscous sub-layer for the near wall flows, damping functions are utilized. These damping functions are typically used to modify of source terms in the transport equation and in the turbulent viscosity expression.

The basic structure of such low Reynolds number models is the same as that of the k- ε model and differs only in the tuning of the damping functions f_1, f_2, and f_μ. The major change is the

introduction of the damping function f_μ introduced to mimic the direct effect of the molecular viscosity on the shear stress:

$$\mu_t = \rho C_\mu f_\mu \frac{k^2}{\varepsilon}. \tag{3.44}$$

An overview of various low-Reynolds number models is reported in the works of Rodi and Mansour [118] as well as Patel et al. [112]. Low-Reynolds turbulence models employed in this work are the models by Lam and Bremhorst [81]. The damping function for the eddy viscosity f_μ is calculated as:

$$f_\mu = \left[1 - exp\left(-0.0165 \frac{\rho k^{1/2} y_P}{\mu}\right)\right]^2 \left(1 + 20.5 \frac{\mu\varepsilon}{\rho k^2}\right). \tag{3.45}$$

The transport equation used for the turbulent kinetic energy has the same form as in the k- ε model and is determined by Equation (3.37). The transport equation for the turbulent dissipation is:

$$\frac{\partial(\rho\varepsilon)}{\partial t} + \frac{\partial(\rho\bar{u}_j\varepsilon)}{\partial x_j} = \frac{\partial}{\partial x_j}\left[\left(\mu + \frac{\mu_t}{\sigma_k}\right)\frac{\partial\varepsilon}{\partial x_j}\right] + C_{1\varepsilon} f_1 \frac{\varepsilon}{k}\mu_t \left(\frac{\partial\bar{u}_i}{\partial x_j} + \frac{\partial\bar{u}_j}{\partial x_i}\right)\frac{\partial\bar{u}_i}{\partial x_j} - f_2 C_{2\varepsilon}\rho\frac{\varepsilon^2}{k}. \tag{3.46}$$

The damping terms f_1 and f_2 are determined from the following equation:

$$f_2 = 1 - exp\left[-\left(\frac{\rho\mu^2}{\mu\varepsilon}\right)^2\right], \tag{3.47}$$

$$f_1 = 1 + \left(\frac{0.05}{f_\mu}\right)^3. \tag{3.48}$$

The model constants in the above equations are listed in Table 3.2.

The summary of governing equations considered in this research is listed in Table 3.3. The numerical methods, discretization techniques of partial differential equations, and the solution algorithm applied in current numerical simulations are described in the following chapter.

Table 3.3: Summary of governing equations for gas-driven liquid film flows

Continuity equation	$\frac{\partial \rho}{\partial t} + \frac{\partial (\rho \bar{u}_i)}{\partial x_i} = 0$
Momentum equation	$\frac{\partial \rho \bar{u}_i}{\partial t} + \frac{\partial (\rho \bar{u}_i \bar{u}_j)}{\partial x_j} = \frac{\partial}{\partial x_j}\left[\underbrace{(\bar{\mu} + \bar{\mu_t})}_{\mu_{eff}} \left(\frac{\partial \bar{u}_i}{\partial x_j} + \frac{\partial \bar{u}_j}{\partial x_i} \right) \right] - \frac{\partial}{\partial x_i}\left(\bar{p} + \frac{2}{3}\rho k \right) + \rho g_i + F_{si}$ $F_s = \sigma \kappa \vec{n} = \sigma \left(\nabla \cdot \frac{\nabla \gamma}{\lvert \nabla \gamma \rvert} \right) \nabla \gamma$
Energy equation	$\frac{\partial (\rho C_p \bar{T})}{\partial t} + \frac{\partial (\rho C_p \bar{u}_i \bar{T})}{\partial x_j} = \frac{\partial}{\partial x_j}\left(C_P \left[\frac{\mu}{Pr} + \frac{\mu_t}{Pr_t} \right] \frac{\partial \bar{T}}{\partial x_j} \right)$
VOF equation	$\frac{\partial \gamma}{\partial t} + \nabla \cdot (\bar{u}\gamma) + \nabla \cdot \left(u_C \gamma (1-\gamma) \right) = 0 \qquad (0 \le \gamma \le 1)$ $\emptyset = \gamma \emptyset_L + (1-\gamma)\emptyset_G$: $\emptyset$ is a variable.
k equation	$\frac{\partial (\rho k)}{\partial t} + \frac{\partial (\rho \bar{u}_j k)}{\partial x_j} = \frac{\partial}{\partial x_j}\left[\left(\mu + \frac{\mu_t}{\sigma_k} \right) \frac{\partial k}{\partial x_j} \right] + \mu_t \left(\frac{\partial \bar{u}_i}{\partial x_j} + \frac{\partial \bar{u}_j}{\partial x_i} \right) \frac{\partial \bar{u}_i}{\partial x_j} - \rho \varepsilon$ $\mu_t = \rho C_\mu f_\mu \frac{k^2}{\varepsilon}$
ε equation	$\frac{\partial (\rho \varepsilon)}{\partial t} + \frac{\partial (\rho \bar{u}_j \varepsilon)}{\partial x_j} = \frac{\partial}{\partial x_j}\left[\left(\mu + \frac{\mu_t}{\sigma_k} \right) \frac{\partial \varepsilon}{\partial x_j} \right] + C_{1\varepsilon} f_1 \frac{\varepsilon}{k} \mu_t \left(\frac{\partial \bar{u}_i}{\partial x_j} + \frac{\partial \bar{u}_j}{\partial x_i} \right) \frac{\partial \bar{u}_i}{\partial x_j} - f_2 C_{2\varepsilon} \rho \frac{\varepsilon^2}{k}$ $f_\mu = \left[1 - exp\left(-0.0165 \frac{\rho k^{1/2} y_P}{\mu} \right) \right]^2 \left(1 + 20.5 \frac{\mu \varepsilon}{\rho k^2} \right)$ $f_2 = 1 - exp\left[-\left(\frac{\rho \mu^2}{\mu \varepsilon} \right)^2 \right]$ $f_1 = 1 + \left(\frac{0.05}{f_\mu} \right)^3$

4

Numerical Method, Procedure and Accuracy

This chapter describes the analysis of the numerical accuracy and the solver algorithm considerations in the context of two-phase flows. Moreover, the numerical methodologies implemented in the solver code are briefly described. The flow-governing equations are discretized to obtain a linear system of equations, which can be solved by the CFD solver. Since discretization plays a significant role in simulation results, the details of each term discretization in the governing equations are presented.

4.1 Numerical method

The errors introduced in the numerical solutions of the fluid flow and heat transfer problems are mainly due to approximated solutions. Therefore, the corresponding issue of accuracy becomes an important consideration. The main sources of errors dealing with numerical solutions are discretization and physical modeling errors. The former are due to the difference between the exact solution of the modeled equations and a numerical solution with a limited time and space resolution. They arise because the governing equations are numerically approximated. These errors tend to accumulate through computational processes that may yield unphysical CFD solutions. Physical modeling errors occur because of the uncertainty in the formulation of the mathematical models and simplifications of the models. For example, turbulence modeling requires huge computational resources if it is to be simulated directly, so the models are frequently simplified to reduce the computational load. However, physical modeling errors are examined through validation studies. Validation represents the final stage of determining whether the accuracy of a model corresponds to the real physical flow problem that is solved. Further details of validation procedures in the case studies are described in Chapter 5.

First, the main focus is placed on the finite volume discretization of governing equations obtained through numerical methods. It is important that interpolation schemes associated with the discrete

approximations are employed for the partial differential equations. Accordingly, the interpolation schemes utilized in the numerical solver are also briefly described.

4.1.1 Finite volume discretization and schemes

For a numerical solution of the governing transport equations, the computational domain is divided into a number of finite control volumes. This process of discretization of partial differential equations into an algebraic set of equations and solving it iteratively is obtained by using the finite volume approach [38]. This is the most common method for single and multi-phase flow simulations [30, 150]. For unsteady flow problems in which the solution is transient in nature, the time is divided into a set of discrete time steps, with each step describing a discrete spatial solution at that particular instance of time. In CFD, numerous discretization methods for numerical simulation of governing partial differential equations are available [38, 148]. The numerical methods and their implementation in the OpenFOAM solver code are described in the works of Jasak and Rusche [67, 122].

The computational domain is represented by the mesh covering the space of interest subdivided into a number of control volumes. Figure 4.1 shows two generalized adjacent control volumes of a computational domain bounded by a set of faces, with each face shared by a neighboring control volume. The points P and N represent the centroids of each control volume and its neighbor, respectively. S_f represents the surface normal vector of the common face of both cells, and d denotes the connecting vector between the points P and N [67]. Control volume faces are divided into two groups, namely internal faces and boundary faces coinciding with the boundaries of the domain.

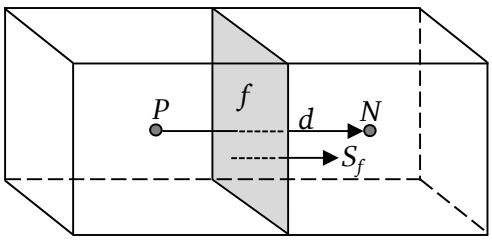

Figure 4.1: A typical control volume representation of finite volume discretization and geometric parameters [67, 141]

Discretization of governing transport equations

The discretization of conservative equations is explained based on the following generic transport equation (4.1). For a transport variable φ (mass, velocity, temperature and turbulent energy), the standard generic form of the transport equation is given by the following expression:

$$\underbrace{\frac{\partial(\rho\varphi)}{\partial t}}_{I} + \underbrace{\nabla\cdot(\rho u\varphi)}_{II} = \underbrace{\nabla\cdot\left(\Gamma_\varphi\nabla\varphi\right)}_{III} + \underbrace{S_\varphi(\varphi)}_{IV}. \tag{4.1}$$

Here, ρ denotes the density of the fluid, t is the time, and u is the fluid velocity vector. The term Γ_φ is a diffusion coefficient. The first term (I) on the left-hand side of Equation (4.1) is the temporal term describing the rate of change in the variable φ. The second term (II) is the convective flux of φ due to the fluid velocity u, and the first term (III) on the right side denotes the rate of transport due to diffusion. All other force terms (pressure and force of gravity) and sources (surface tension) defined per unit volume are expressed by the source term (IV). The Equation (4.1) is a second order equation since the diffusion term includes a second order derivative of φ in space. The order of the discretization should be equal to or higher than the order of the governing equation to achieve acceptable accuracy.

The discretization in the finite volume method is formulated by integrating Equation (4.1) over a control volume V_P at the point P over a time interval $[t, t+\Delta t]$, which can be expressed as:

$$\int_t^{t+\Delta t}\left[\frac{\partial}{\partial t}\int_{V_P}\rho\varphi dV + \int_{V_P}\nabla\cdot(\rho u\varphi)dV - \int_{V_P}\nabla\cdot\left(\rho\Gamma_\varphi\nabla\varphi\right)dV\right]dt = \int_t^{t+\Delta t}\left[\int_{V_P}S_\varphi(\varphi)dV\right]dt. \tag{4.2}$$

In the finite volume method, the surface integrals are estimated by a sum of fluxes across all control volume faces. Finally, to determine the fluxes, cell face values of variables are calculated by interpolation using cell center values at neighboring cells. This leads to a kind of interpolation of various discretization schemes within the control volume approach, among which the upwind scheme is commonly used for convection terms and central differencing for diffusion terms. A detailed description of the finite volume method and various discretization schemes can be found in [148].

Convective term: The discretization of the convective term in Equation (4.1) yields:

$$\int_{V_P}\nabla\cdot(\rho u\varphi)dV \approx \sum_f S_f\cdot(\rho u)_f\varphi_f = \sum_f m_F\varphi_f, \tag{4.3}$$

where subscript f implies the value of the variable in the center of the face. In the above expression, m_F represents the mass flux ($S_f\cdot(\rho u)_f$) through the surface S_f of the control volume. It is assumed that the corresponding values are the interpolated values of ρ and u on the surfaces of the control volume, and are multiplied by one another. Equation (4.3) also requires the value of the variable φ on the control volume surface. In order to interpolate the field variable φ, several schemes are available. The choice of interpolation scheme is an important factor regarding the boundedness and the accuracy of the solution.

According to the Central Differencing (CD) scheme, a linear variation of φ between P and N (see Figure 4.2) and the face value is calculated from the following rule:

$$\varphi_f = f_x\varphi_P + (1-f_x)\varphi_N. \tag{4.4}$$

The interpolation factor f_x, is defined as the ratio of the distances and $\overline{fN}$ and $\overline{PN}$. This central differencing method has a second order accuracy even on unstructured grids [38, 67]. However, this method may lead to unphysical oscillations such that the boundedness of the solution is no longer possible [111]. An alternative interpolation method guaranteeing said boundedness is called the Upwind Differencing (UD) scheme, but this method is only first order of accuracy [38]. According to this scheme, φ_f is defined based on the direction of the flow through the face and the relation given by:

$$\varphi_f = \begin{cases} \varphi_P & \varphi_f \geq 0 \\ \varphi_N & \varphi_f < 0 \end{cases}. \tag{4.5}$$

This scheme is solution-bounded but the order of accuracy is reduced and the solution can become distorted [67]. The Blended Differencing (BD) scheme combines both CD and UD schemes and represents an attempt to preserve both boundedness and accuracy of the solution [122]. It is a linear combination of both the schemes CD and UD:

$$\varphi_f = (1 - \gamma_{BD})(\varphi_f)_{UD} + \gamma_{BD}(\varphi_f)_{CD}. \tag{4.6}$$

In the above expression, γ_{BD} is the blending coefficient and varies between 0 and 1. This term is maintained constant for all faces of the mesh [38]. The blending coefficient determines the amount of numerical diffusion that will be introduced. This scheme reduces to UD for $\gamma_{BD} = 0$. In the present work, the BD scheme is utilized as introduced by Jasak et al. [68] based on the Normalized Variable Approach which allows for a bounded solution at high time-steps [43, 90]. A detailed investigation and evaluation of interpolation methods can be found in the thesis by Jasak [67].

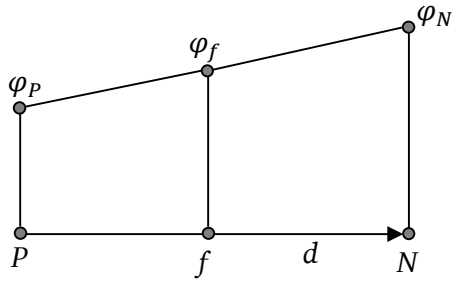

Figure 4.2: Schematic for the interpolation [67]

Diffusion term: The discretization of the diffusive term is described as below:

$$\int_{V_p} \nabla \cdot (\rho \Gamma_\varphi \nabla \varphi) dV \approx \sum_f (\rho \Gamma_\varphi)_f S_f \cdot (\nabla \varphi)_f. \tag{4.7}$$

In the above expression, $S \cdot (\nabla \varphi)_f$ is defined for orthogonal meshes and formulated as follows:

$$S_f \cdot (\nabla\varphi)_f = |S_f| \cdot \frac{\varphi_N - \varphi_P}{|d|}. \tag{4.8}$$

The discretization of the gradient of φ according to Equation (4.8) on the orthogonal grid has second order accuracy. The gradient term can be identified in the respective control volume center of the adjacent cells (4.9) and then interpolated to the control volume surface area (4.10) (see Figure 4.1).

$$(\nabla\varphi)_P = \frac{1}{V_P}\sum_f S_f \varphi_f, \tag{4.9}$$

$$(\nabla\varphi)_f = f_x(\nabla\varphi)_P + (1 - f_x)(\nabla\varphi)_N. \tag{4.10}$$

The discretization of the gradient of φ according to Equations (4.9) and (4.10) with non-orthogonal grids is accurate up to the second order. However, this discretization is similar to CD in the convective term. In addition, the truncation error is greater than that in Equation (4.10), which cannot be applied to non-orthogonal meshes [67]. In order to have lower truncation errors in the formulation (4.10), it is recommended to split the product $S_f \cdot (\nabla\varphi)_f$ into two parts:

$$S_f \cdot (\nabla\varphi)_f = \underbrace{D_f \cdot (\nabla\varphi)_f}_{i} + \underbrace{k_f \cdot (\nabla\varphi)_f}_{ii}. \tag{4.11}$$

In Equation (4.11), i and ii represent the orthogonal and non-orthogonal parts, respectively. The vectors D_f and k_f are related as:

$$S_f = D_f + k_f \ . \tag{4.12}$$

The vector D_f represents the orthogonal component and it is chosen in such a way that it is parallel to the line d, connecting the centers of the control volume (see Figure 4.3). Jasak examined the various decomposition methods of the term S_f in terms of orthogonal and non-orthogonal components [67]. In order to determine D_f and k_f directly, the discretized form of the expression $S_f \cdot (\nabla\varphi)_f$ can be stated as follows:

$$S_f \cdot (\nabla\varphi)_f = |\Delta_f| \cdot \frac{\varphi_N - \varphi_P}{|d|} + k_f \cdot (\nabla\varphi)_f. \tag{4.13}$$

The term $S_f(\varphi)$ can be determined by Equation (4.12). The possible approaches to correct the non-orthogonality utilized in OpenFOAM are the minimum correction approach, the orthogonal correction approach and the over-relaxed approach [67, 141].

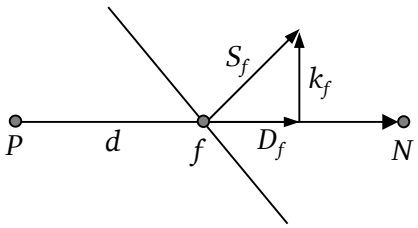

Figure 4.3: Schematic representation of vectors d and S on a non-orthogonal mesh [67]

Source term: The source term $S_\varphi(\varphi)$ in Equation (4.2) can be a general function of φ. The source term is first linearized into the following form [111]:

$$S_\varphi = S_{expl} + S_{impl}\varphi, \tag{4.14}$$

where S_{expl} and S_{impl} are dependent on φ. The volume integral of the source terms is calculated as:

$$\int_{V_p} S_\varphi(\varphi)dV = S_{expl}V_P + S_{impl}\varphi_P V_P. \tag{4.15}$$

The term S_{expl} is treated explicitly, i.e. it appears on the right side in the resulting system of equations. The term S_{impl} is treated implicitly or explicitly depending on the sign. If $S_{impl} < 0$, the expression is treated implicitly since the matrix becomes diagonally dominant, thus improving the convergence behavior. In the case of $S_{impl} > 0$, the term is treated explicitly.

Temporal discretization

Using the spatial discretization of the various terms introduced in the previous section, the temporal term from the transport Equation (4.1) can be discretized in the following form:

$$\left(\frac{\partial \rho\varphi}{\partial t}\right)^n = \frac{\rho^n\varphi^n - \rho^{n-1}\varphi^{n-1}}{\Delta t}, \tag{4.16}$$

where φ^n represents the values at time $t + \Delta t$, and φ^{n-1} represents the values at the previous time step at time t. This form of temporal discretization is known as the Crank-Nicolson method, which is of second order of accuracy in time. The backward differencing method is also of second order accuracy in which three time levels are used for the discretization of the time derivative. This relation is expressed as:

$$\left(\frac{\partial \varphi}{\partial t}\right)^n = \frac{\frac{3}{2}\varphi^n - 2\varphi^{n-1} + \frac{1}{2}\varphi^{n-2}}{\Delta t} \tag{4.17}$$

with

$$\varphi^{n-2} = \varphi(t - \Delta t). \tag{4.18}$$

The discretized form of the backward differencing transport equation is expressed as:

$$\frac{\frac{3}{2}\varphi^{n} - 2\varphi^{n-1} + \frac{1}{2}\varphi^{n-2}}{\Delta t} V_P + \left[\sum_f m_F \varphi_f^n - \sum_f \left(\rho\Gamma_\varphi\right)_f S \cdot (\nabla\varphi)_f^n\right] = \left[S_{expl} V_P + S_{impl}\varphi_P^n V_P\right]. \tag{4.19}$$

The backward differencing scheme is considerably easier to implement than the Crank-Nicolson method. Moreover, the Crank-Nicolson method requires inner-iterations during each time step to evaluate the flux term [67]. Therefore, the backward differencing scheme is utilized in this work because of its boundedness on the solution.

Adaptive time step control

In transient two-phase flow simulations, the stability of the solution procedure is often controlled by using an adaptive time step. Applying adjustable time steps enables accurate calculations and reduces computational time. Therefore, it is an important consideration in numerical simulations.

The time step is adjusted at the beginning of the iteration loop using the Courant number Co relation, which is evaluated from the following expression:

$$Co = \frac{\left|u_f \cdot S_f\right|}{d \cdot S_f} \Delta t. \tag{4.20}$$

A local Courant number Co_0 is evaluated using the values of u_f and Δt from the previous time step and the new time step Δt^n is computed from the following expression:

$$\Delta t^n = min\left\{min\left[min\left(\frac{Co_{max}}{Co_0}\Delta t_0, \left(1 + \lambda_1 \frac{Co_{max}}{Co_0}\right)\Delta t_0\right), \lambda_2 \Delta t_0\right], \Delta t_{max}\right\}, \tag{4.21}$$

where Co_{max} and Δt_{max} are predefined limit values for the time step and Courant number. The factors λ_1 and λ_2 are used to avoid time step oscillations by damping the increased time step, and the values are set to 0.1 and 1.2 respectively. The maximum Courant number Co_{max} is maintained at a value of around 0.2 while setting up the initial conditions [12, 13]. However, during the simulation an intermediate time-step value (Δt_{ini}^*) is determined from an initial value of the time step (Δt_{ini}) evaluation by the equation:

$$\Delta t_{ini}^* = min\left(\frac{Co_{max}\Delta t_{ini}}{Co_0}; \Delta t_{max}\right). \tag{4.22}$$

Based on the above expression, the time step is adjusted smoothly by maintaining the maximum local Courant number Co_{max}. Hence, the value of Δt_0 in Equation (4.21) is an intermediate time-step [67].

4.1.2 System of linear equations and convergence

The complete discretization of the generic transport equation (4.2) leads to a linear algebraic equation for each control volume. The following is the general algebraic form of an arbitrary discretized transport equation,

$$a_P \varphi_P^n + \sum_N a_N \varphi_N^n = R_P, \tag{4.23}$$

where a_P and a_N are coefficients associated with the faces of the control volume P and its neighbor N, respectively. The coefficients a_P include the contribution from all terms of φ_P^n, including the temporal derivative, convection and diffusion terms, while the coefficients a_N represent the corresponding terms of each of the neighboring control volumes. The term R_P denotes explicit contributions to the system of boundary conditions and explicit source terms. In order to solve for φ_P^n, since its value depends on the neighbor values, a linear algebraic system of equations with a general form is obtained:

$$[A][\varphi] = [R]. \tag{4.24}$$

In the above expression, the diagonal entities of the square matrix $[A]$ are defined as a_P and off-diagonal elements as a_N. The matrix $[\varphi]$ is the vector containing the values of φ at each cell center, and the matrix $[R]$ is the vector containing all the explicitly discretized terms expressed for each control volume. This system of equations is solved by iterative methods, starting with an initial estimate and then continuing to improve the approximation of the solution until the residual tolerance is met. Iterative or convergence errors occur due to the difference between a fully converged solution of a finite number of grid points and a solution that has not fully achieved convergence. The CFD code solves the discretized equations iteratively at a given time step in transient methods. Moreover, the convergence rate of iterative methods depends on the magnitude of the coefficients in the matrix $[A]$. This research study uses the Conjugate Gradient iterative solution algorithm proposed by Hestens and Steifel [57] to solve the system of algebraic equations. The Incomplete Cholesky preconditioned Conjugate Gradient (ICCG) solver algorithm is employed for symmetric matrices, while the Bi-CGStab algorithm is adapted for asymmetric systems of equations [146].

4.2 Numerical solution

The momentum and continuity equations constitute four equations, with the three velocity components and pressure as the unknowns. However, the continuity equation is a kinematic

condition for velocity fields and cannot be used to determine pressure. The linear system of equations in flow-related problems is not directly resolved. Nonetheless, it is possible to resolve the coupling of the equations with each other. Subsequently, the equations must satisfy both the continuity and momentum equations. A pressure correction procedure is introduced for the coupling between pressure and velocity [66].

4.2.1 Pressure-velocity algorithm

In order to derive the pressure equation, a semi-discretized form of the momentum equation obtained using Equation (4.23) is expressed as follows [13, 66]:

$$a_P u_P = H(u) - \nabla p. \tag{4.25}$$

The term $H(u)$ consists of two parts: the “transport part” which includes the matrix of coefficients for all neighbor cells multiplied by corresponding velocities; and the ’source part’ composed of the source terms of the transient term and all other source terms apart from the pressure gradient. The above equation can also be solved for the velocity u_P using the following relation at the cell center dividing by a_P:

$$u_P = \frac{H(u)}{a_P} - \frac{\nabla p}{a_P}. \tag{4.26}$$

From the above relation, the velocity at the cell face can be interpolated and obtained as:

$$u_f = \left(\frac{H(u)}{a_P}\right)_f - \left(\frac{1}{a_P}\right)_f (\nabla p)_f. \tag{4.27}$$

In order to derive the pressure equation, the discrete incompressible continuity equation is expressed as:

$$\sum_f S_f u_f = 0. \tag{4.28}$$

Using Equations (4.27) and (4.28), the following form of the pressure equation is obtained:

$$\nabla \cdot \left(\frac{1}{a_P} \nabla p\right) = \sum_f S_f \left(\frac{H(u)}{a_P}\right)_f. \tag{4.29}$$

The final form of the discretized incompressible Navier-Stokes equations is:

$$a_P u_P = H(u) - \sum_f S_f (p)_f. \tag{4.30}$$

$$\sum_f S_f \left[\left(\frac{1}{a_P} \right)_f (\nabla p)_f \right] = \sum_f S_f \left(\frac{H(u)}{a_P} \right)_f . \tag{4.31}$$

The face fluxes F_F are computed using u_f from Equation (4.27):

$$F_F = S_f \cdot u_f = S_f \cdot \left[\left(\frac{H(u)}{a_P} \right)_f - \left(\frac{1}{a_P} \right)_f (\nabla p)_f \right]. \tag{4.32}$$

The face fluxes are guaranteed to be conservative by satisfying Equation (4.29).

4.2.2 Solution algorithm

The algebraic system of equations resulting from the discretization of a conservation equation is solved sequentially. To solve the discretized volume fraction equation, an explicit time scheme is used, while other transport equations rely on an iterative solver. The pressure-velocity treatment for transient flow calculations employs the Pressure Implicit with Splitting of Operators (PISO) algorithm, originally proposed by Issa [66]. The numerical algorithm sequence at a specified time step is implemented in the solver as presented in Figure 4.4.

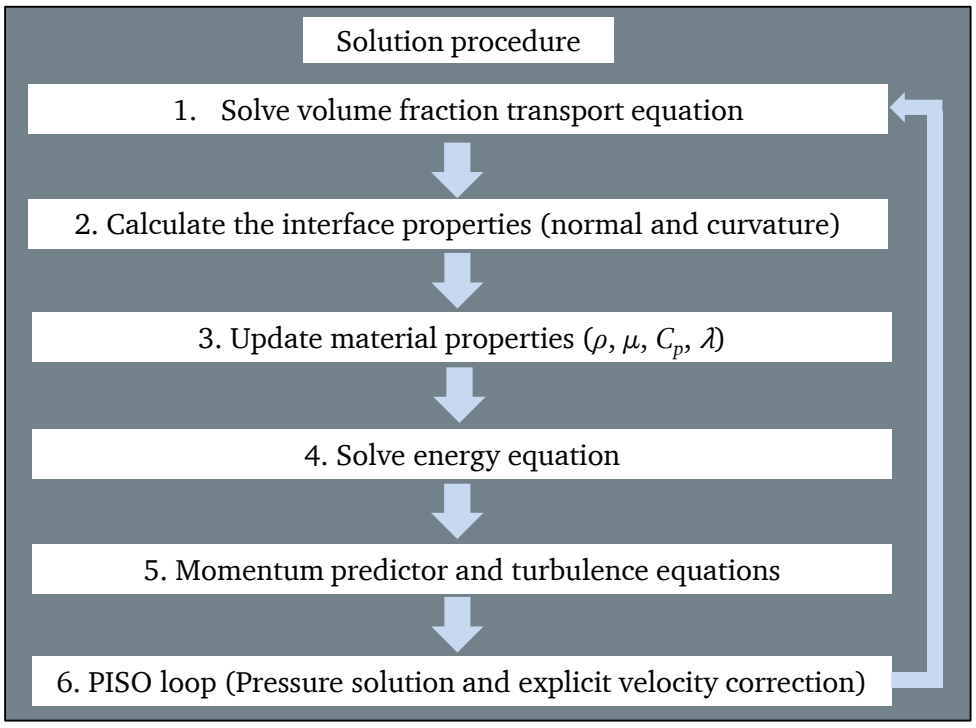

Figure 4.4: Graphical description of the numerical algorithm

4.3 Boundary and initial conditions

To solve a two-phase flow problem, the specification of initial and boundary conditions is necessary. Mathematical or numerical descriptions of the boundary conditions are divided into two groups: The first type are the Dirichlet boundary conditions, prescribing a fixed value of a respective variable on the boundary, while the second type of boundary conditions are the von Neumann boundary conditions with the gradient of the variables in the normal direction to the boundary. The choice of the numerical boundary condition depends on the flow variables and on the physical influence of each boundary in the flow domain. In the following, the fundamental treatment of flow boundaries applied in this work is briefly explained.

Boundary conditions

Inlet flow: The velocity field and all other scalars are described at the inlet region by a Dirichlet boundary condition. The condition at the inflow boundary requires at least one velocity component to be given for the solution of the governing equations. At the inlet boundary, the velocity in the x-direction of the Cartesian frame of coordinates is given by:

$$u = u_{in} \text{ and } v = w = 0, \tag{4.33}$$

where u_{in} can either be a constant value or a velocity profile of the gas and liquid phases at the inlet. The volume fraction occupied by the fluid is also required for the two-phase flow simulation. For the pressure force on the inlet boundary, a von Neumann boundary condition with a vanishing normal derivative is applied. Similarly, the boundary conditions are also imposed at the inlet boundary in the y and z directions. For the two-phase flow system with heat transfer, it is also common procedure to impose the Dirichlet boundary condition at the inlet.

$$T = T_{in}. \tag{4.34}$$

For turbulent two-phase flows, experimentally verified quantities can be applied at the inlet boundaries for the turbulent scalar variables. The specification of the inlet turbulent kinetic energy can be assumed by relating the inlet turbulence to the turbulence intensity. Approximate values for the turbulent kinetic energy and dissipation can be determined from the following expressions:

$$k_{in} = \frac{3}{2}(u_{in}I)^2, \tag{4.35}$$

$$\varepsilon_{in} = C_{\mu}^{3/4}\frac{(k_{in})^{3/2}}{l}, \tag{4.36}$$

where I is the turbulent intensity level and l is the characteristic length scale.

Outlet flow: In the outlet region, a type of von Neumann boundary condition is specified with a vanishing normal derivative for all variables except for the pressure. The velocity component at the

outlet boundary is assumed to be fully developed and remains unchanged in the flow direction. The outlet condition for the velocity is given as:

$$\frac{\partial u}{\partial n} = \frac{\partial v}{\partial n} = \frac{\partial w}{\partial n} = 0, \tag{4.37}$$

where n is the direction normal to the surface. This type of von Neumann boundary condition is equally applicable to the volume fraction and temperature. The pressure boundary condition is specified by a Dirichlet boundary condition.

Solid walls: The no-slip condition, which is a Dirichlet boundary condition, is prescribed for the velocity and the von Neumann boundary conditions with zero gradients, and it is used for the pressure and volume fraction. For heat transfer problems, the wall temperature T_W is applied on the wall as Dirichlet boundary condition. Fourier's law of heat conduction can be employed to provide a necessary boundary condition at the wall based on the known wall heat flux. According to Fourier's law, the boundary condition at the wall becomes:

$$\frac{q_W}{\lambda} = -\left[\frac{\partial T}{\partial n}\right]_W. \tag{4.38}$$

In the above boundary condition, q_W refers to the specified wall heat flux. For adiabatic boundary condition, the temperature gradient is assumed to be zero at the boundary and referred to as the insulated boundary. The boundary conditions for turbulent quantities depend on the grid resolution near the wall in the normal direction.

Symmetric boundary: A symmetric boundary condition can be imposed on a plane with symmetric behavior in the flow field and it is a type of von Neumann boundary condition with a vanishing normal derivative of velocity.

Initial conditions

The values of the dependent variables $\varphi = u, p, T, k, \varepsilon$, at the initial instant of time $t = 0$, have to be provided at all cells of the computational domain. The volume fraction γ has to be defined in the solution domain based on the definition of the initial film thickness h.

4.4 Numerical procedure

The methodology adopted to perform the numerical study is summarized and illustrated by the flowchart in Figure 4.5. The numerical flow setup, solution, and post-processing is achieved by using various types of software and tools, with Table 4.1 summarizing the main programs and tools utilized in the present thesis. Computations are performed on a 2 × Quad core processor machine with 2 × 3.16 GHz speed and 16 × 2048 MB memory. Each calculation takes up to 50 hours to complete 1 second of simulation time. The transient simulations are executed so that numerical stabilization can be achieved.

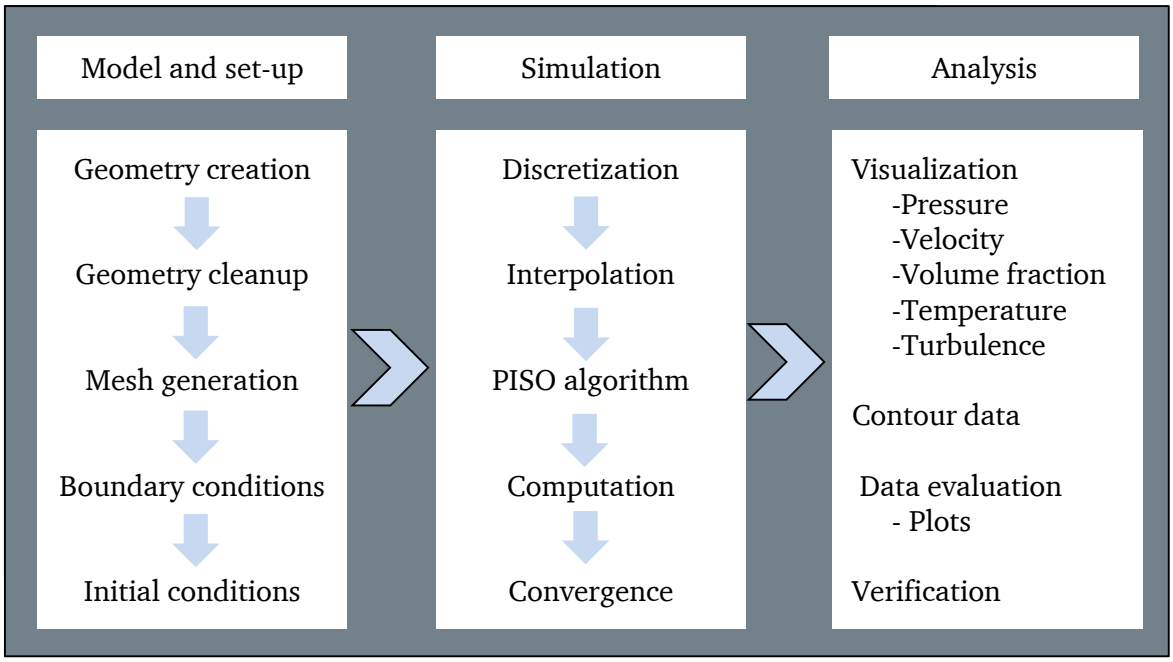

Figure 4.5: Graphical description of the flowchart summarizing the numerical methodology

Table 4.1: Summary of tools utilized in the current work

Pre-processing			Solver	Post-processing
CAD model	Meshing	Sub-routines	OpenFOAM	OpenFOAM (Paraview) ANSYS MS-Excel
Catia ANSYS	OpenFOAM ICEMCFD	MATLAB		

Although the open source package has been proven accurate in many studies of isothermal two-phase flows, an additional energy equation is further included in the solver code. For validating the source code, a forced convection heat transfer in a rectangular channel is considered. More detailed descriptions for theoretical study and comparisons with experiment data are provided in the following section. With the information mentioned above related to numerical methodology, it is necessary to validate the solver by theory, experiments, and published data applicable to this study. The following chapter deals with the results obtained from the VOF method and their comparison with the in-house measured data. A thorough analysis and discussion of the results of the test cases are also included in Chapter 5.

4.5 Numerical accuracy

In order to begin the simulation, it is necessary to analyze the numerical accuracy and determine the optimum mesh density. In this work, two-dimensional rectangular channel two-phase flow simulations are initially run to estimate the accuracy of the numerical method and the VOF model. To evaluate the accuracy of the numerical model, the analytical film thickness of a shear-driven liquid film is considered. The details of the analytical film thickness derivation are discussed in Chapter 5. This test consists of two immiscible fluids, where the liquid phase represents water, and the gas phase represents air. The water and air properties at a pressure of 1 bar are considered. The liquid and gas are assumed to be incompressible and initially at rest. The computational domain is considered with the dimensions of 0.12 m in length and 0.01 m in depth. The domain is initially discretized with 340 cells in the horizontal direction and 30 cells in the vertical direction. This test case is further simulated at different mesh resolutions. In this uncertainty problem, the liquid is initially considered at a height of the theoretical film thickness in the computational domain.

For consistent comparisons, the fractional error E_e for the simulation test cases is defined by the following relation [47]:

$$E_e = \frac{|h_e^N - h_e^A|}{h_e^A}, \tag{4.39}$$

where h_e^A is the analytical film thickness, and h_e^N is the numerically simulated film thickness.

The results of the numerical simulations in terms of the gas-liquid interface position for all the mesh resolutions are summarized in Table 4.2. The fractional error for the computational mesh size of 600 x 60 is significantly lower. The results of the numerical simulations of two-phase flow 2D simulations for higher liquid Reynolds numbers (Re_L = 295 and 350) at a gas Reynolds number of Re_G = 7800 are summarized in Table 4.3. A good accuracy is obtained with a relative error contained within 6-7% of the analytical solution for the mesh size of 600 x 60.

Table 4.2: Mesh resolution and results of two-phase shear-driven flow 2D problem for Re_L = 160 and Re_G = 7800

Mesh Resolution (x-y)	Theoretical film thickness (m)	Computed film thickness (m)	Fractional error (-)
240 x 30	0.001388	0.001054	0.240634
360 x 40	0.001388	0.001267	0.087176
480 x 50	0.001388	0.001288	0.072046
600 x 60	0.001388	0.001364	0.017291

Table 4.3: The results of two-phase shear-driven flow problem at $Re_G = 7800$ and mesh resolution of 600 x 60

Liquid Reynolds number (-)	Theoretical film thickness (m)	Computed film thickness (m)	Fractional error (-)
295	0.0017574	0.001635	0.0696
350	0.0018722	0.001755	0.0626

5

Results and Discussions

The present research uses the OpenFOAM CFD software, based on an open source framework, for numerical simulations. The numerical methodologies described in the previous chapter are applied to calculate the flow field at specified gas-liquid stratified flow conditions. This chapter is divided into two sections: The first deals primarily with the results used for the validation of the VOF model, while the second contains the simulations describing the hydrodynamics of two-phase turbulent flow and its implications for heat transfer. Finally, the analysis of a wavy liquid film sheared by an accelerated gas flow is discussed.

5.1 Numerical validation

The selection of a suitable solver is the key step in the current work. To validate the existing VOF method in the OpenFOAM solver, the exact solution to the problem is used. Initially, for the validation of the numerical model, a simple two-phase fluid flow without heat transfer is considered. Next, an analytical solution of the two-dimensional incompressible momentum and continuity equations for a fully developed laminar liquid film driven by incompressible gas flow is theoretically determined. The simulated result of the VOF technique and CSF model is then compared with the analytical velocity profiles of the gas and liquid phases

5.1.1 Analytical velocity profiles of the gas-liquid phases

The two-dimensional incompressible momentum and continuity equations for a hydro-dynamically developed laminar liquid film driven by incompressible co-current gas flow are solved analytically. The derived analytical velocity profiles allow studying the accuracy of the computational results.

In the literature, Bird et al. [14] derived laminar velocity profiles by assuming a known liquid height, eliminating one of the unknown parameters of the solution. However, the initial film

thickness is unknown and solved analytically in this study. During the analytical solution, the inlet mass fluxes or Reynolds numbers are assumed as inlet parameters in a channel.

A schematic view of the geometrical configuration of a shear-driven film model is shown in Figure 5.1. A channel of height H and length L with a stratified flow of liquid and gas is considered (see Figure 5.1). The liquid height h from the lower wall is treated as an interface between the gas and liquid phases. At this interface, the density and viscosity of both phases vary but the velocity and shear stresses are assumed to be continuous. The derivation of the analytical problem is taken to be two-dimensional. It is assumed that the undisturbed flow field in the channel is fully developed, i.e. only x components of velocities exist both in the liquid and in the gas phase, and these velocities depend on a y component. No-slip boundary conditions are imposed at the channel walls, while tangential stress continuity and velocity continuity conditions are set at the gas-liquid interface. The flow parameters of liquid and gas are defined as the ratio of mass flow rate per unit length (Γ_L and Γ_G) to dynamic viscosities (μ_L and μ_G) of the liquid and the gas, respectively.

The following assumptions are made in deriving the analytical velocity profile:

(i) The flow is laminar without interfacial waves

(ii) Physical properties are constant inside the domain

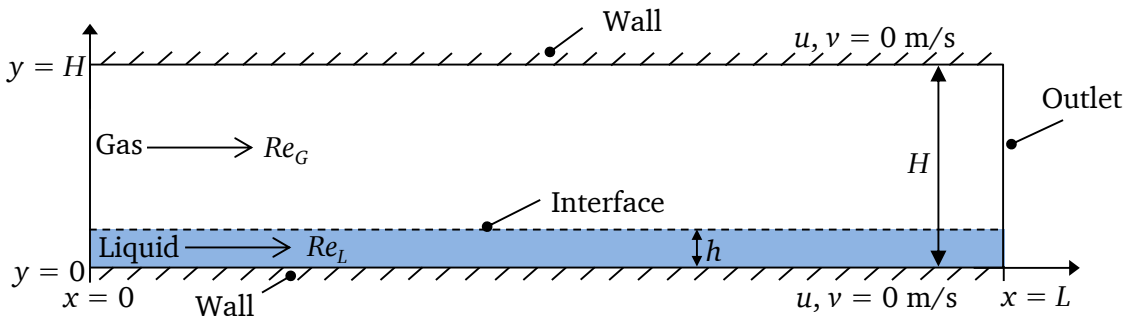

Figure 5.1: Schematic view of the computational domain for the numerical simulation

The equation of laminar motion for incompressible and Newtonian fluid is expressed as:

$$\frac{\partial p}{\partial x} = \frac{\partial}{\partial y}\left[\mu \frac{\partial u}{\partial y}\right]. \tag{5.1}$$

The right hand side of Equation (5.1) is only dependent on the y coordinate due to assuming a fully developed flow. The term $\partial p/\partial x$ is a function of the x coordinate and does not change in the axial coordinate. Therefore, the stream-wise pressure gradient is seen as constant:

$$\frac{\partial p}{\partial x} = \text{constant}\,. \tag{5.2}$$

At the liquid height h, the viscosities of the gas and liquid phases can be expressed as:

$$\mu = \begin{cases} \mu_G & y > h \\ \mu_L & y < h \end{cases}, \tag{5.3}$$

where subscripts G and L denote the gas and liquid phases, respectively. Further assumptions on the continuous stress τ at the interface are given as:

$$\lim_{y \to h^+} \tau = \lim_{y \to h^-} \tau \tag{5.4}$$

therefore,

$$\lim_{y \to h^+} \mu_G \frac{\partial u}{\partial y} = \lim_{y \to h^-} \mu_L \frac{\partial u}{\partial y}. \tag{5.5}$$

The resulting velocity field after applying the boundary conditions for a given mass flow rate per unit perimeter (Γ_L and Γ_G) and liquid and gas properties (viscosities and densities) are derived in the following form:

$$u_L(y) = \frac{6\Gamma_L}{\rho_L(2h^3 - 3C_2h^2)}(y^2 - C_2 y), \qquad 0 < y < h \tag{5.6}$$

$$u_G(y) = \frac{\Gamma_G}{\rho_G C_1}(y^2 - H^2) - C_2(y - H), \qquad h < y < H \tag{5.7}$$

$$C_1 = \left[-\frac{2H^3}{3} + C_2\frac{H^2}{2} - \frac{h^3}{3} + H^2 h + C_2\frac{h^2}{2} - C_2 Hh \right] \tag{5.8}$$

$$C_2 = \left[\frac{\mu_L(H^2 - h^2) + \mu_G h^2}{\mu_L(H - h) + \mu_G h} \right] \tag{5.9}$$

The above equations of the velocity profiles are a system of two non-linear equations that can be solved numerically. To that end, numerical MATLAB sub-routines were developed and used to solve the initial film thickness for a developed laminar flow at specified inlet conditions. The code of this numerical sub-routine is provided in the Appendix.

5.1.2 Computational 2D model

To evaluate the proposed VOF technique for gas-driven liquid films, a two-dimensional rectangular channel is considered, as shown in Figure 5.1. The geometry of the 2D computational domain is created using the open-source geometry creation sub-routine function. The VOF technique requires hexahedral elements to allow the code to be run with available computational resources, for which reason hexagonal meshes have been used in the OpenFOAM computational model. The grid-independent study has been carried out to determine the ideal number of grid cells for the study. The mesh in the region of the interface must be fine enough that the curvature of the interfacial

region is well resolved. Figure 5.2 shows a computational domain of the 2D model with the hexahedral mesh adopted in the simulations. The 2D computational channel (100 mm x 20 mm) would require 60 elements in the wall normal direction and 1000 elements in the flow directions.

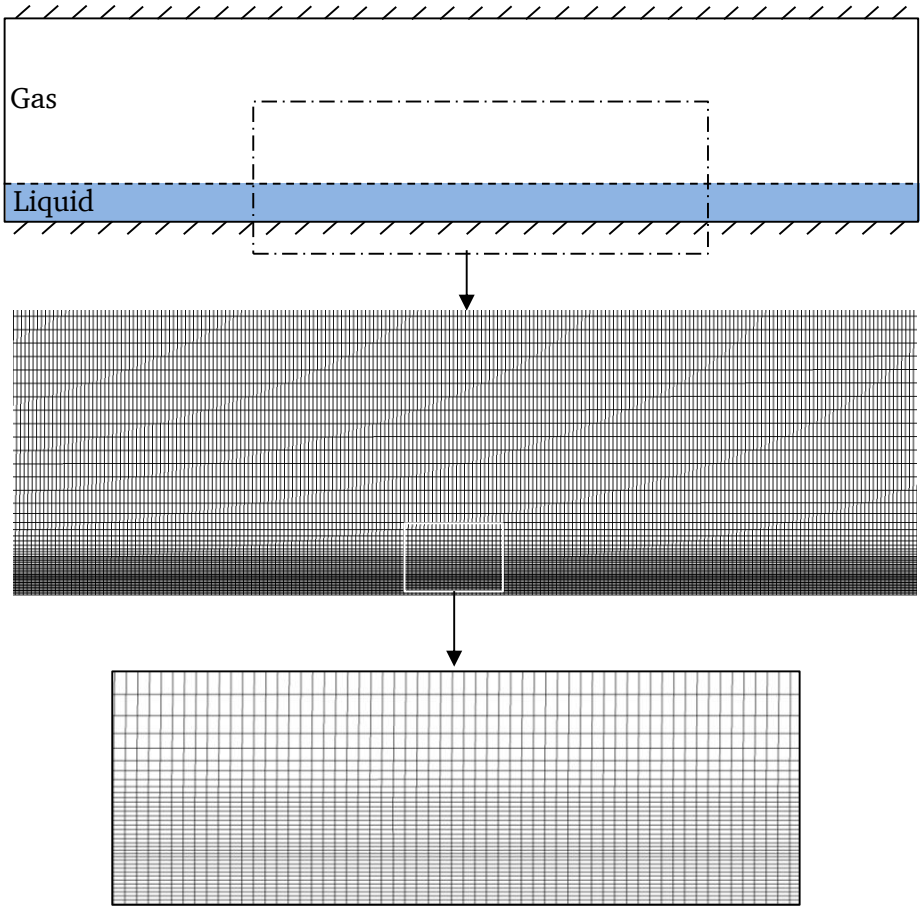

Figure 5.2: Computational mesh details

The liquid and gas are introduced from the left of the channel as shown in Figure 5.1. Gas flows co-currently on to the liquid surface resulting in changes to the film thickness. The physical properties, pressure p, the fractional volume of fluid γ, and the velocity field u, are defined at the boundaries. The volume fraction coefficient is assumed to be one at the liquid inlet and zero at the gas inlet, since pure liquid and pure gas enter the channel through these boundary surfaces. At the walls and the outlet boundary, γ has zero gradient since its value does not change at these boundaries. No boundary conditions are imposed at the gas-liquid interface, as this is not a computational boundary in the VOF method. For pressure, a zero gradient boundary condition is applied at all boundaries except for the outlet, where the pressure is fixed as a constant outlet pressure value. Moreover, the fluids are incompressible, and thus the pressure does not depend on density and temperature. Accordingly, the absolute value of the pressure is not of interest, but rather the pressure changes or the pressure gradient across the channel, which are still calculated via the PISO algorithm. However, pressure is considered as constant ($p = 0$) on the specified reference value at the outlet boundary. For velocity, the no-slip condition is set in the upper (top wall) and in the lower (bottom wall) boundary.

The applied boundary conditions for the flow parameters for numerical computation are listed in Table 5.1. Equations (5.6) and (5.7) yield the velocity profile for the inlet gas and liquid phases.

The simulation is initialized with a liquid film of thickness h all along its length, and the gas occupies the rest of the computational domain (Figure 5.1). The initial liquid stream velocity is provided by Equation (5.6) everywhere in the channel, while the gas stream velocity is given by Equation (5.7). Fluid properties considered at room temperature are listed in Table 5.2.

Table 5.1: Boundary conditions for numerical simulation

Boundary face	γ (-)	p (N/m^2)	u (m/s)
Gas inlet	0	$\partial p / \partial n = 0$	$u_G(y)$
Liquid inlet	1	$\partial p / \partial n = 0$	$u_L(y)$
Top wall	$\partial \gamma / \partial n = 0$	$\partial p / \partial n = 0$	0
Bottom wall	$\partial \gamma / \partial n = 0$	$\partial p / \partial n = 0$	0
Outlet	$\partial \gamma / \partial n = 0$	$p = 0$	$\partial u / \partial n = 0$

Table 5.2: Transport properties of the fluids

Fluid	Density (kg/m^3)	Viscosity (kg/m s)	Surface tension (N/m)
Water	998	9.8×10^{-4}	7.2×10^{-2}
Air	1.2	1.8×10^{-5}	

Grid independence test

The liquid film thickness is very thin compared to the width of the gas domain. The simulation result must be able to accurately capture the interface in both the normal and flow directions. Furthermore, coarsening the mesh both along the stream-wise direction would introduce numerical errors, particularly if high inlet gas velocities were used in the stream-wise directions. In order to study the phenomena occurring between the liquid phase and the gas phase, the mesh has to be very fine around the interface. It is further important to note that, when considering the viscous effect near wall boundaries, the mesh should also be refined in the transverse direction of the bottom wall. Errors during the capturing of the interface and the occurrence of numerical diffusion causing any discontinuities in the flow field are mainly due to the density difference at the interface, as well as the surface tension force between gas and liquid. Such disadvantages cannot be avoided in current simulations. However, they can be significantly minimized by optimizing the mesh.

For the validation test case, an appropriate mesh resolution is achieved by carrying out grid independence studies with successive grid refinement. The mesh structure shown in Figure 5.2 was refined further in the stream-wise and transverse directions (1000 x 100 elements in the x and y direction, respectively). Initially, simulations are performed for a coarse mesh, observing few

numerical deviations. The interface is distorted and smeared due to numerical diffusion (see Figure 5.3), caused by a coarse mesh size. Mesh refinement can minimize this issue. The results are almost consistent with grid refinement, and the interface is nearly smooth when compared with other coarse mesh cases. The velocity profiles of gas and liquid from the results of each simulation are compared to determine the grid independence.

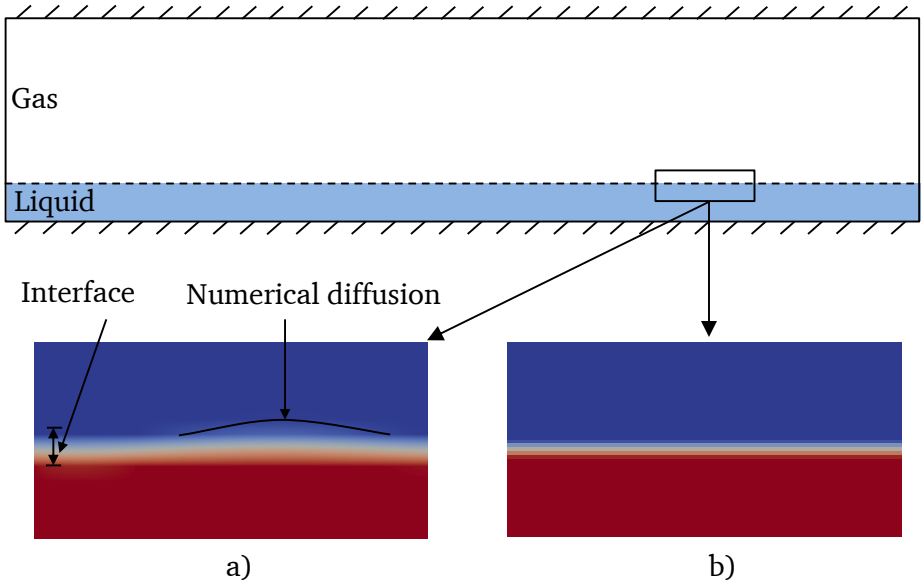

Figure 5.3: Computational mesh: a) coarse mesh b) fine mesh

5.1.3 Verification with theoretical solution

For the present study, the 'interFoam' solver in OpenFOAM and a combination of a Eulerian fixed mesh representations are used to capture the interface in the isothermal case [106]. The structure of OpenFOAM code allows new sub-models to be incorporated into the overall code structure. In the numerical computations, parabolic velocity profiles, given in Equations. (5.6) and (5.7), are imposed as boundary conditions for both the liquid and gas flows at an inlet. These velocity profiles are also considered as an initial condition in the computational flow domain. Figure 5.4 presents a comparison between theoretical data and the simulation results for the velocity profiles of gas and liquid films, yielding excellent agreement between the two. The semi-parabolic profile of a liquid film in the simulation results is similar to the derived theoretical velocity field in falling liquid films as observed by Nusselt [105]. Figure 5.4 illustrates that the VOF model is capable of predicting smooth surface liquid behavior. In conclusion, Figure 5.4 further demonstrates that CFD simulation with the VOF model can predict liquid flow behavior. Thereby, it proves the viability of the VOF model for analyzing such a liquid flow system. Additionally, it shows that the results from the simulation are acceptable and confirms the solver code for further simulations.

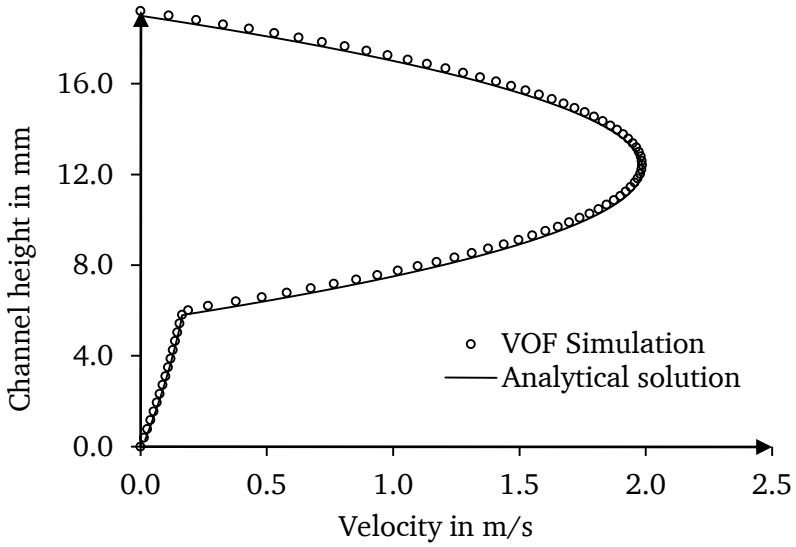

Figure 5.4: Comparison of velocity profiles at a longitudinal mid-section of the channel of a laminar flow in a channel

5.1.4 Qualitative comparison with the literature data on shear-driven wavy film

The velocity profile, which is determined analytically, is used to the provide initial velocity field throughout the computational domain. At the channel inlet, the velocity profile is given by Equations (5.6) and (5.7). Table 5.1 summarizes the imposed boundary conditions. The initial fluid domain is filled with a liquid phase of thickness h, while the gas phase covers the remaining domain. The initial liquid and gas velocities are assumed through the developed velocity profiles. The inlet artificial perturbation $u_{L,f}$ with frequency f_L and amplitude A_L is given as:

$$u_{L,f} = u_L(y)[1 + A_L \sin(2\pi f_L t)] \tag{5.10}$$

The two-phase VOF model implemented in OpenFOAM has been validated by comparison with simulation results as reported by Valluri et al. [143]. Flow velocities are maintained at a very low value with liquid and gas Reynolds numbers of 29.1 and 0.03, respectively. The fluid properties for the simulations are set at a density ratio of ρ_L/ρ_G =1, μ_L/μ_G = 30; a surface tension of $\sigma = 1.74 \times 10^{-6}$ N/m and the perturbation frequency of $f = 0.05$ Hz were selected. Valluri et al. [143] studied the spatio-temporal dynamics of undulations in an immiscible gas-liquid stratified laminar flow inside a 2D channel using the MAC method along with the diffuse-interface method with liquid inflow perturbation. Figure 5.5 compares the results of the current VOF simulation with that by Valluri et al. [143], finding a good qualitative agreement.

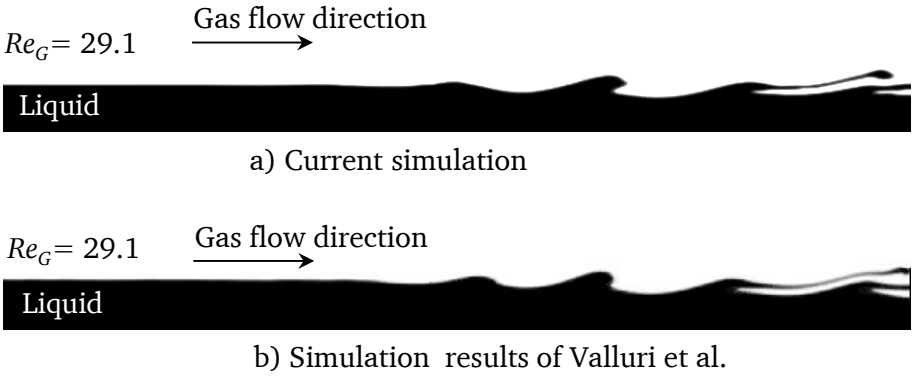

Figure 5.5: Comparison of the interface profiles between (a) the current VOF simulation with (b) the simulation results of Valluri et al. [143] at Re_L= 0.03 and Re_G= 29.1

Figure 5.6 presents the volume fraction distribution in the 2D channel with wave evolution and pressure contours in the liquid phase. In this figure, pressure changes from red to blue are indicated from the inlet to the outlet. This means that the pressure is highest at the inlet and lowest at the outlet region. It should be mentioned here that the regions of the gas phase in the following figures are blanked in order to highlight the liquid phase condition. The contour of the liquid volume fraction at 0.5 is shown in black color. The wavy film regions are shown in three different positions at a downstream distance from x = 70 mm to 150 mm (Figure 5.7 to Figure 5.10).

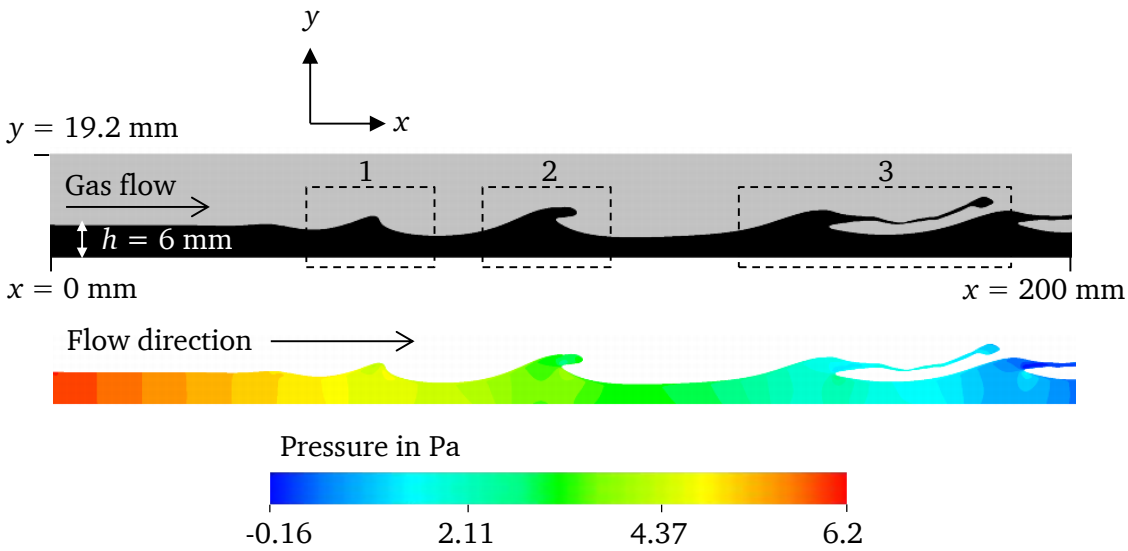

Figure 5.6: Volume fraction distribution in two-dimensional channel (top) and pressure distribution in the liquid phase (bottom). The upper layer (gas phase) and lower layer (liquid phase) are in the ratios of ρ_L/ρ_G =1 and μ_L/μ_G = 30

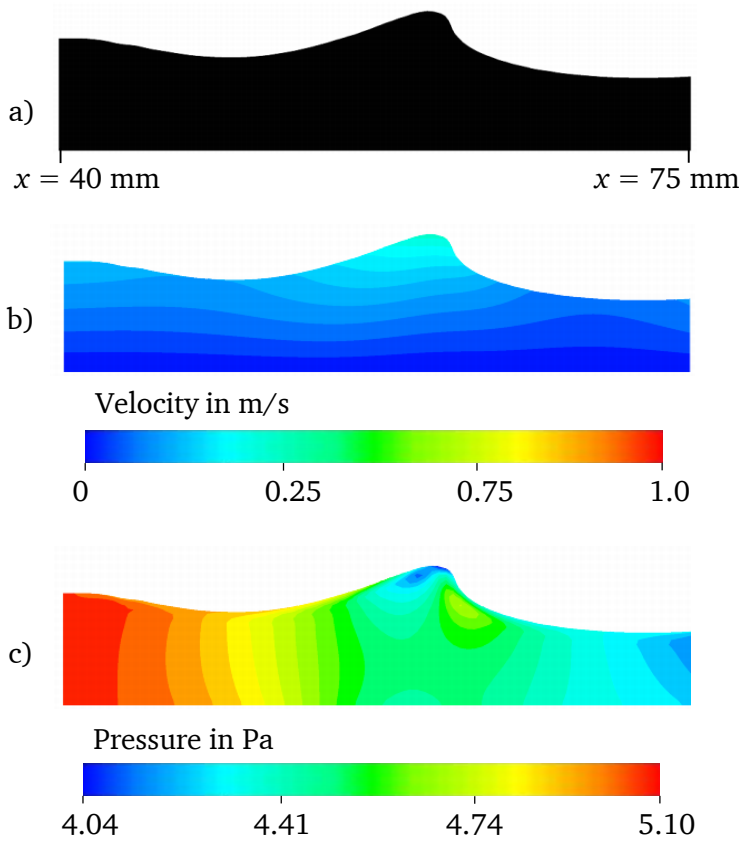

Figure 5.7: a) Liquid volume fraction, b) velocity distribution, c) pressure contours in the liquid phase at position 1 with reference to Figure 5.6

It is observed from Figure 5.6 that a ligament is formed at 70 mm from the inlet. This ligament is seen in box 2 and zoomed in on in Figure 5.8 along with the velocity and pressure distribution. From the figure, it can be noted that this ligament is stretched by the surrounding phase. The zoomed view of the root and tip of the ligament with the pressure distribution is presented in Figure 5.9. The pressure inside the ligament is lowered, causing a sharp gradient at its root (see Figure 5.9). This pressure gradient drives the fluid from the lower layer into the ligament. The low pressure at the tip is connected with the high velocity in this region (K-H mechanism). The acceleration in the ligament tip leads to the ligament stretching, similar to the findings of Boeck et al. [16]. During this process, the height of the wave at the root of the ligament slowly increases (see Figure 5.10). The velocity in the ligament rises gradually, reaching its maximum velocity at the ligament's tip. As the acceleration occurs in this location, due to the increased momentum, the ligament stretches towards the crest of the downstream wave. Accordingly, the stretching of ligaments is affected significantly by downstream waves [144].

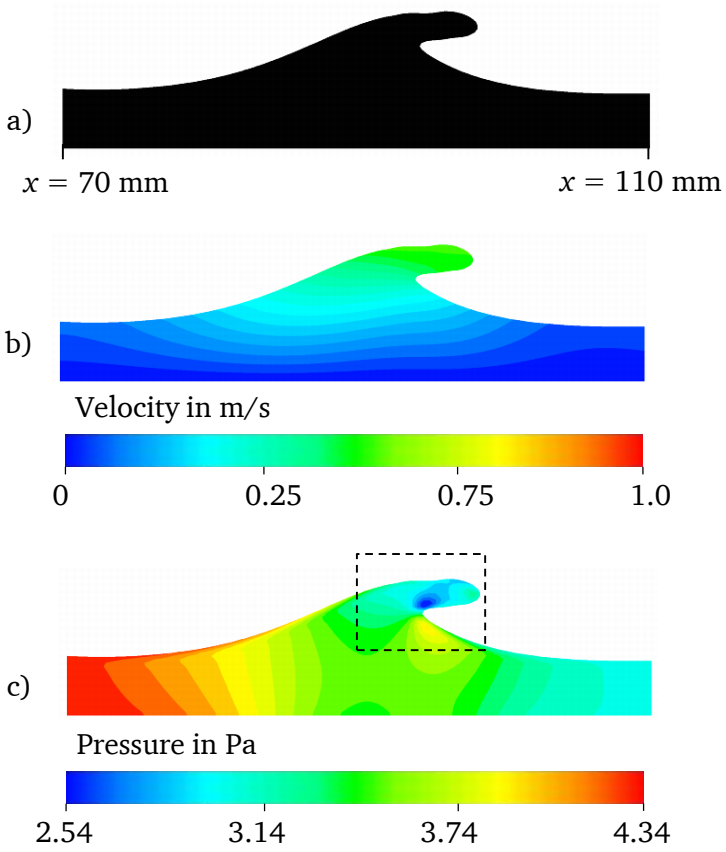

Figure 5.8: a) Liquid volume fraction, b) velocity distribution, c) pressure contours in the liquid phase at position 2 (box-2) with reference to Figure 5.6

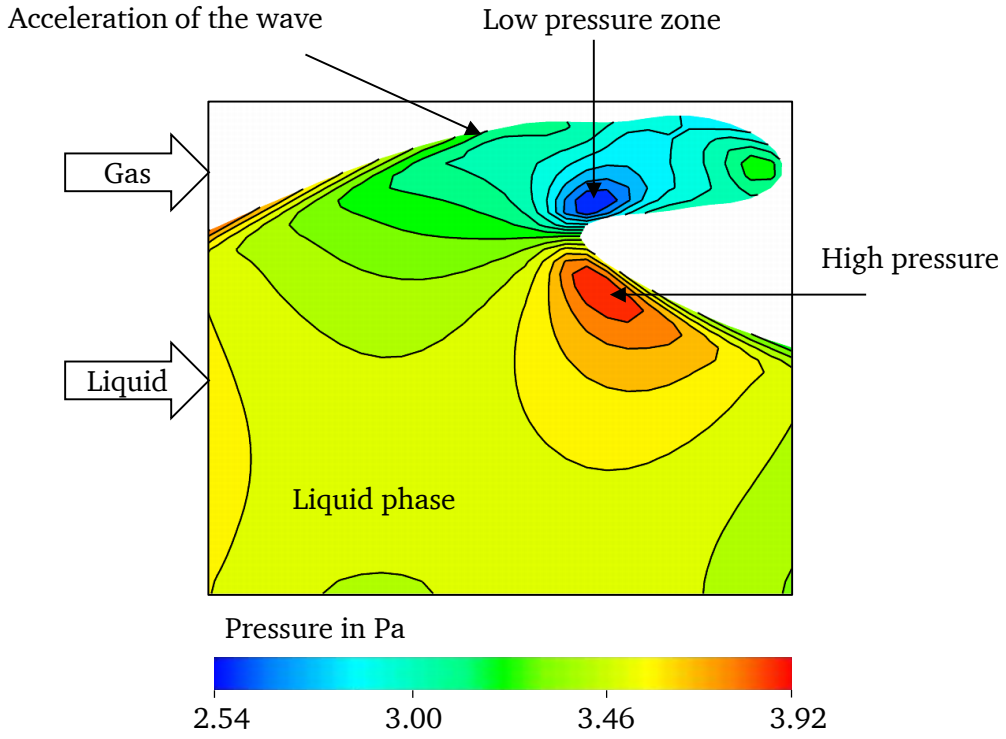

Figure 5.9: Pressure contours in the liquid phase at the accelerating wave position (zoom of the wave tip with reference to Figure 5.8)

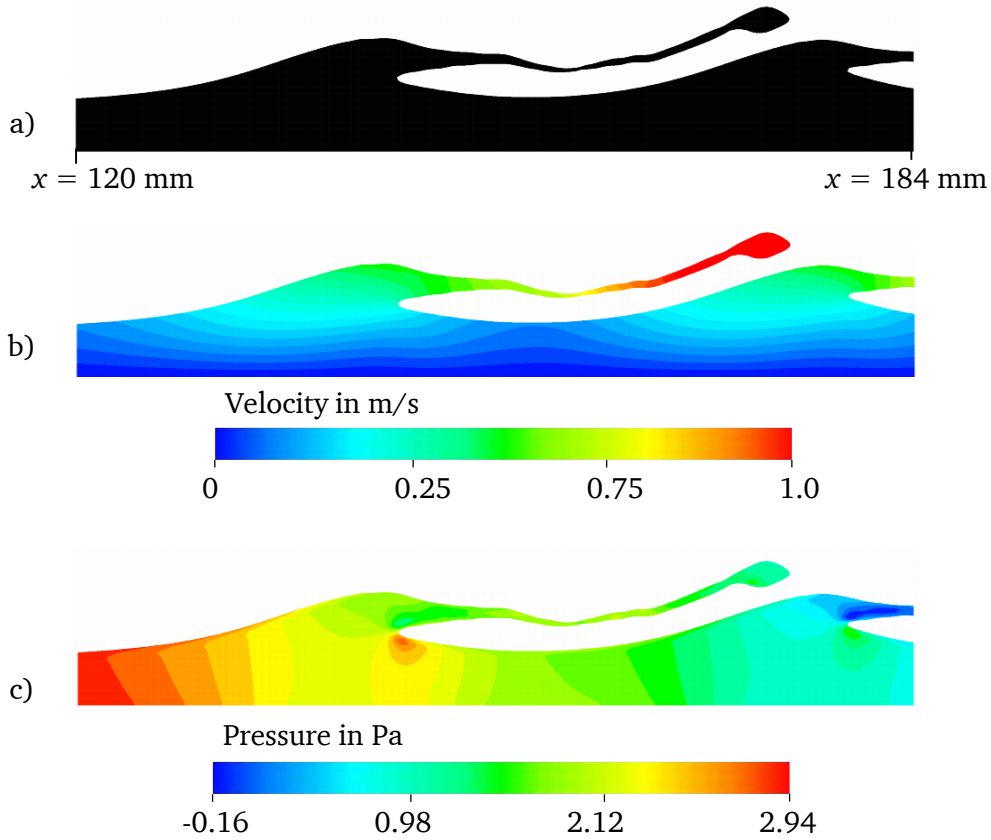

Figure 5.10: a) Contours of the liquid volume fraction, b) velocity distribution, c) pressure distribution in the liquid phase at position 3 with reference to Figure 5.6

5.2 Validation of two-phase convective heat transfer

The main objective in this work is to develop and further modify the solver code in capturing the complete features of the flow with heat transfer in gas-liquid flow applications. In this section, the numerical code regarding convective heat transfer is validated against the results reported by Frisk and Davis [40].

5.2.1 Theoretical and experimental details

Frisk and Davis [40] performed a theoretical and experimental study of heat transfer in a horizontal channel with co-current air flow over water on a heated flat bottom wall. In their study, the experimental results were shown to be in good agreement with their theoretical analysis of heat transfer in smooth laminar film. In the latter, the two-dimensional temperature field in a smooth horizontal liquid film flowing under the influence of the shear of a co-currently flowing gas is described by the convective diffusion equation,

$$u\frac{\partial T}{\partial x} = \alpha\left(\frac{\partial^2 T}{\partial y^2} + \frac{\partial^2 T}{\partial x^2}\right). \tag{5.11}$$

The details of the coordinates and a schematic of the considered system for the theoretical study is shown in Figure 5.11 [40]. The flow in the channel was assumed to be fully hydro-dynamically developed and thermally developing. The flow is a function of the pressure gradient (dp/dx) and the interfacial shear τ_i exerted by the turbulent gas phase on the liquid film. The velocity distribution in the liquid film, with a thickness of h is given by,

$$u = \frac{dp/dx}{2\mu}(y^2 - 2hy) + \frac{\tau_i y}{\mu}. \tag{5.12}$$

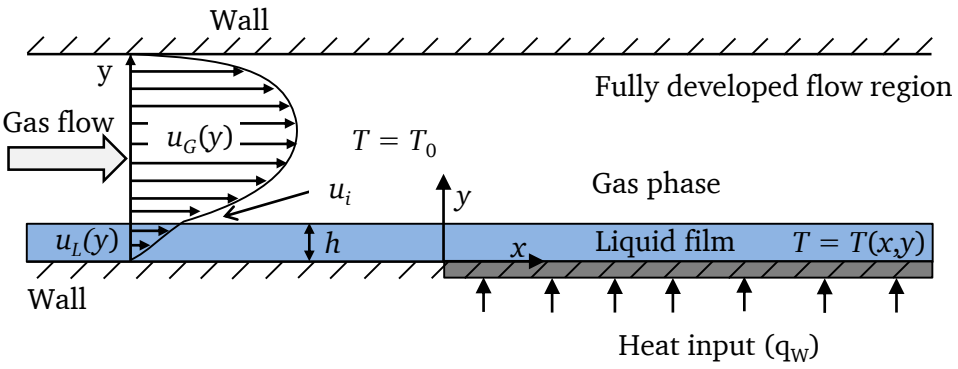

Figure 5.11: Schematic view of the system and coordinates adopted for theoretical study [40]

The dimensionless variables for temperature and spatial coordinates with the Peclet number ($Pe \equiv hu_{int}/\alpha$, u_{int} is the interfacial velocity) are defined in Equation (5.13) The experiments were performed by Frisk and Davis [40] under a constant wall heat flux q_w, and therefore the dimensionless temperature is normalized by the factor $q_w h/\lambda$ [40]. The detailed description of the theoretical solution of the temperature field and the resulting assumptions for the two-phase flow is reported in the work of Davis [27].

$$\zeta = \frac{y}{h}, \xi = \frac{x}{hPe} \; and \; \theta = \frac{(T - T_0)}{(q_w h/\lambda)}. \tag{5.13}$$

In the above equation T_0 is inlet temperature. For $Pe > 100$, the heat conduction in the flow direction is negligible. With dimensionless variables, the temperature Equation (5.11) reduces to,

$$\zeta\frac{\partial \theta}{\partial \xi} = \frac{\partial^2 \theta}{\partial \zeta^2}. \tag{5.14}$$

Equation (5.14) can be solved analytically as,

$$\theta = \theta_\propto + \sum_{n=1}^{\propto} A_n \psi_n(\zeta) exp(-\lambda_n^2 \xi), \tag{5.15}$$

where $\theta_\propto$ is the asymptotic temperature distribution, and the eigenfunctions are defined by the following expression,

$$\psi_n(\zeta) = K_1 E_n^{\frac{1}{3}} \sqrt{\zeta} J_{\frac{1}{3}}\left(\frac{2}{3} E_n \zeta^{\frac{3}{2}}\right) + K_2 E_n^{\frac{1}{3}} \sqrt{\zeta} J_{-\frac{1}{3}}\left(\frac{2}{3} E_n \zeta^{\frac{3}{2}}\right). \tag{5.16}$$

By applying the boundary conditions in the above expression, the coefficients K_1, K_2 and the eigenvalues E_n can be obtained. The term A_n in Equation (5.15) is solved using the usual orthogonality properties of $\psi_n(\zeta)$, and $\psi_m(\zeta)$, by way of the inlet conditions.

The corresponding experimental setup employed in the work of Frisk and Davis [40] is shown schematically in Figure 5.12. The test section was 6.1 m long, with a width of 35 cm, and a height of 2.61 cm. It was further connected to a turbo-compressor for air supply. The stream of water was passed through a rotameter in the channel near the air inlet. A copper block of 60.1 cm was inserted at the channel bottom for the heat supply. This copper block was divided into six sections as shown in Figure 5.12 [26]. Electrical strip heaters were installed below the copper block, and electrical power supplied to each section. This kind of arrangement was employed to maintain constant uniform heat flux through the wall.

In order to prevent a large increase in the mean fluid temperature across the test section, a low energy supply was maintained. This also ensured that the transverse temperature gradients in the film would be small enough to avoid instabilities due to buoyant forces, further eliminating the effects of variation on the physical properties of the heat transfer. The gas and liquid flow rates were set to attain the desired flow regime, and power was adjusted for a constant wall flux condition in the system. In order to avoid recirculation in the flow and maintain a smooth liquid film, soluble surfactants were used, with the result that liquid wave motion was suppressed during experiments.

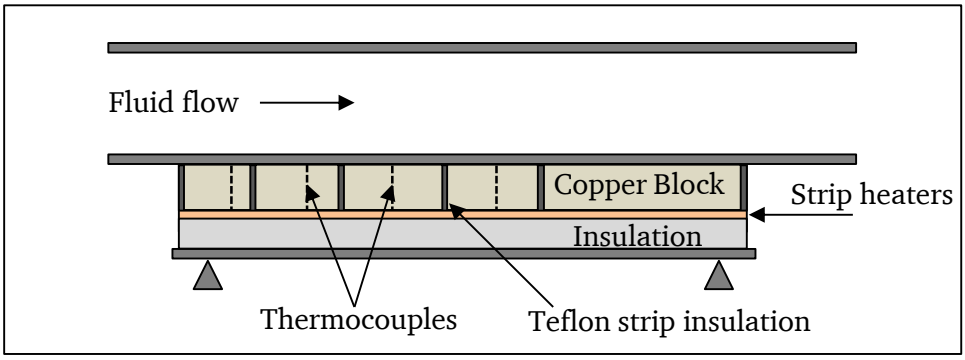

Figure 5.12: Experimental set-up for the heat transfer [40]

5.2.2 Validation

Computations are performed on a 2D grid as described in Section 5.1 for the Reynolds numbers $Re_L = 242$ and $Re_G = 14700$ as reported by Davis and Frisk [40] in their experiments. A homogeneous heat flux boundary condition is applied at the bottom surface as shown in Figure

5.13. The fine grid was selected mainly to ensure the quality of the expected results and proper convergence of the numerical simulation.

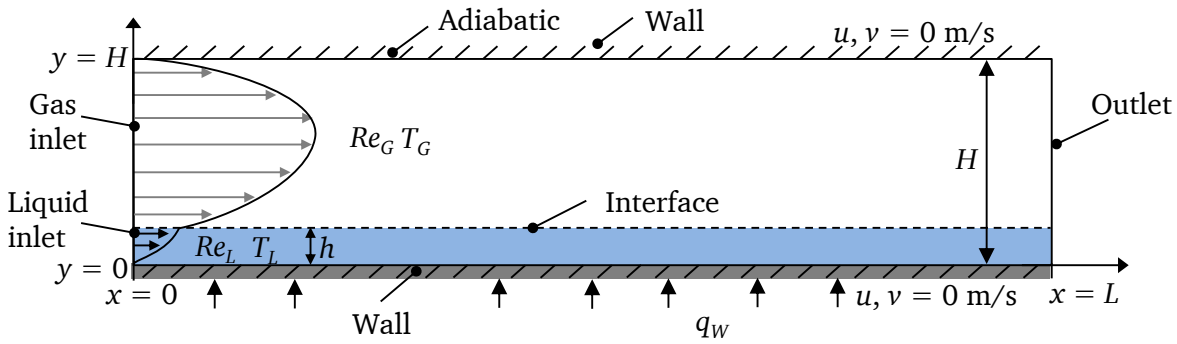

Figure 5.13: Schematic of the computational set-up with initial and boundary conditions for two-phase flow with heat transfer

The boundary conditions defined for the validation of the heat transfer case are provided in Table 5.1. The working fluids used during the simulations are water and air, whose physical properties are presented in Table 5.2 ($\sigma = 0.05$ N/m with surfactants), while thermal properties are listed in Table 5.3. In the case of heat transfer, both the phases enter the flow channel at room temperature ($T_0 = 294$ K). A constant temperature gradient is maintained at the wall, which can also correspond to a constant heat flux as derived from Fourier's law.

$$\left.\frac{\partial T}{\partial n}\right|_W = -\frac{q_W}{\lambda}. \tag{5.17}$$

The heat transfer boundary conditions applied during simulation are listed in Table 5.4. For the velocity, no-slip condition is applied at the wall boundaries of the channel. At the outlet boundary, the velocity gradient is assumed to be zero. In the computational domain, the initial film thickness and volume fraction regions are defined as the initial condition (see Figure 5.14). The computations are performed using the developed velocity boundary condition at the gas and liquid inlets.

Table 5.3: Thermal properties of the fluids

Fluid	Specific heat (J/kg K)	Thermal conductivity (W/m K)
Water	4076	0.605
Air	1006	0.026

Table 5.4: Temperature boundary conditions

Boundary face	Boundary value
Gas inlet	T_G =294 K
Liquid inlet	T_L =294 K
Top wall	$\frac{\partial T}{\partial y} = 0$
Bottom wall	$\frac{\partial T}{\partial y} = -\frac{q_W}{\lambda_L}$
Outlet	$\frac{\partial T}{\partial y} = 0$

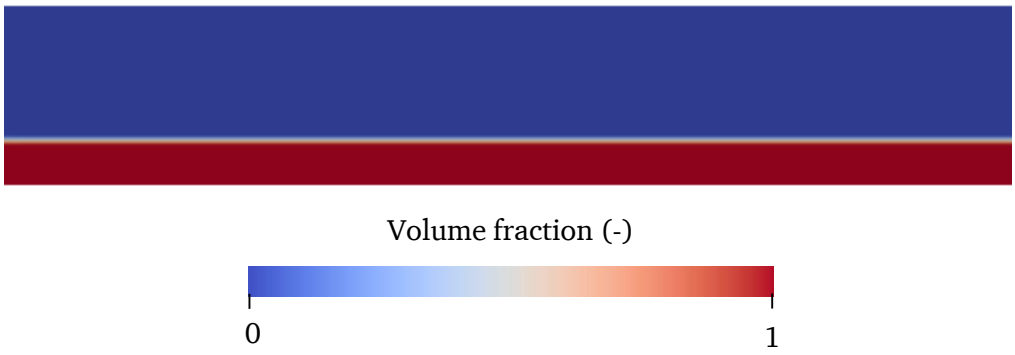

Figure 5.14: Initial conditions of initial film height with volume fraction contour

The Nusselt number used to compare experimental, theoretical and simulated data is defined by

$$Nu = \frac{q_w h}{k(T_w - T_0)}, \tag{5.18}$$

where q_w is the local heat flux, h is the film thickness, T_W is local wall temperature and T_0 is the inlet temperature.

In order to validate the numerical model, the Nusselt number has been plotted against the wall distance and compared with the predicted theoretical solution and experimental measurements. As seen from Figure 5.15, the heat transfer data is shown to be in very good agreement. The slight deviation can be attributed to the theoretical derivation being based on a laminar smooth film flow. Waves generated during the computation can affect the film thickness and the velocity at the interface region. Accordingly, the simulation results are slightly higher than those seen in the theoretical solution.

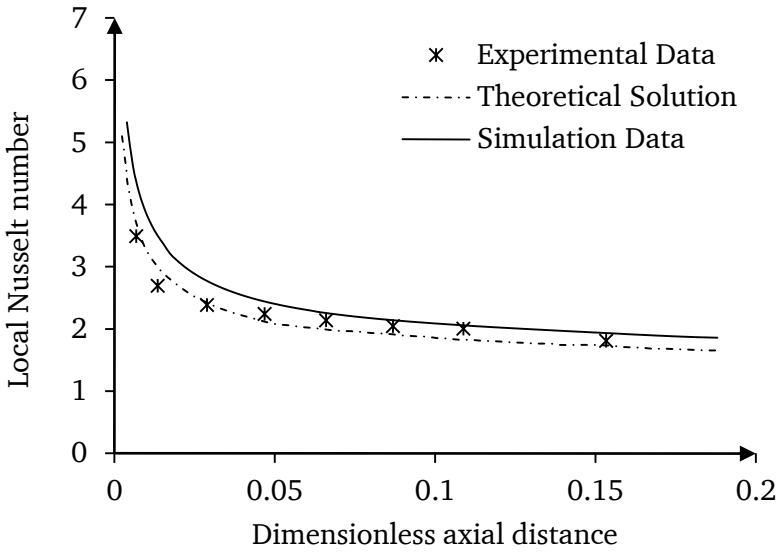

Figure 5.15: Validation of the current simulation (at $Re_G = 14700$, $Re_L = 242$) with the literature data of Davis and Frisk [40]

5.3 Heat transfer in a locally heated 2D channel

Figure 5.16 shows a Nusselt number variation at two different average liquid flow velocities at the fixed gas Reynolds number $Re_G = 15370$. It is obvious that the heat transfer is enhanced and that the Nusselt number values are higher for a liquid velocity of 1 m/s compared to lower velocity of 0.3 m/s. The presence of forced convection enhances the heat transfer process, resulting in an increase in the Nusselt number.

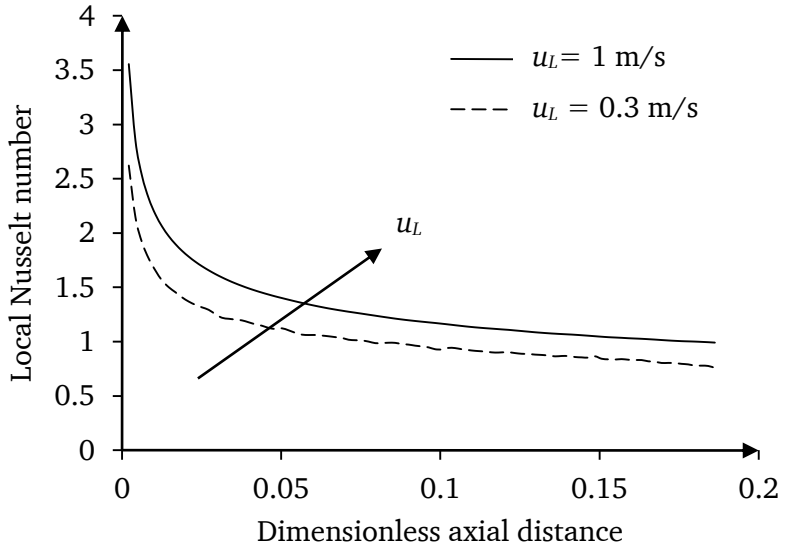

Figure 5.16: Effect of liquid loading on the Nusselt number at $Re_G = 15370$

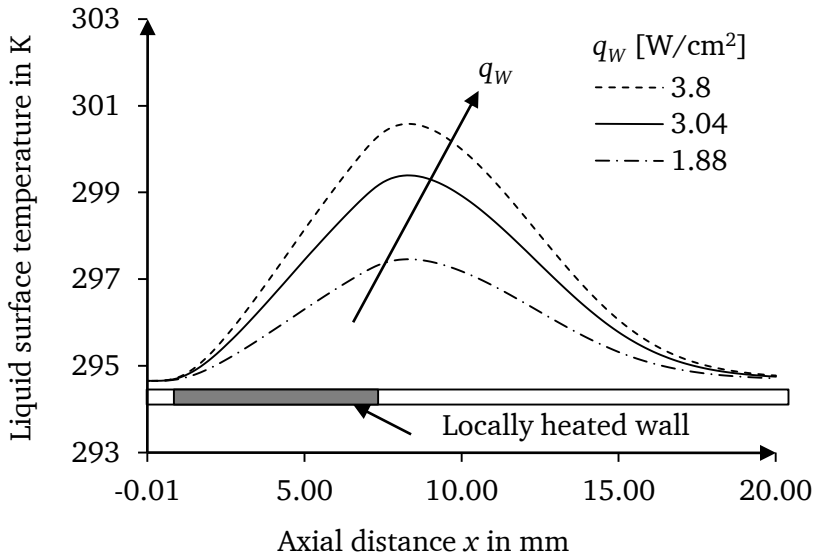

Figure 5.17: Liquid surface temperature distribution at Re_L = 8.5, Re_G = 531, q_W = 1.88, 3.04, 3.8 W/cm^2

The results presented below were obtained for a locally heated liquid film driven by the gas phase. The computed temperature distributions in the axial direction on the liquid surface are presented in Figure 5.17. The simulations were performed at Re_L = 8.5 and Re_G = 534 by varying the heat flux values. In this flow regime, the corresponding film thickness h was of 200 μm and the inlet temperature was at 294 K. The heat flux at the local heater was maintained at 1.88, 3.04, and 3.8 W/cm^2, respectively. Figure 5.17 shows a noticeable effect of the heat flux on the stream-wise temperature [44]. The temperature reduction along the stream-wise direction is due to heat transfer between the liquid surface and the gas phase. Figure 5.18 presents the wall temperature distribution that is a function of the x coordinate along the flow direction. Considering the heat flux boundary condition on the channel bottom, the wall temperature rapidly increases with growing distance from the bottom. A maximum value is reached at the end of the heater and followed by a decrease in temperature (see Figure 5.18) [44].

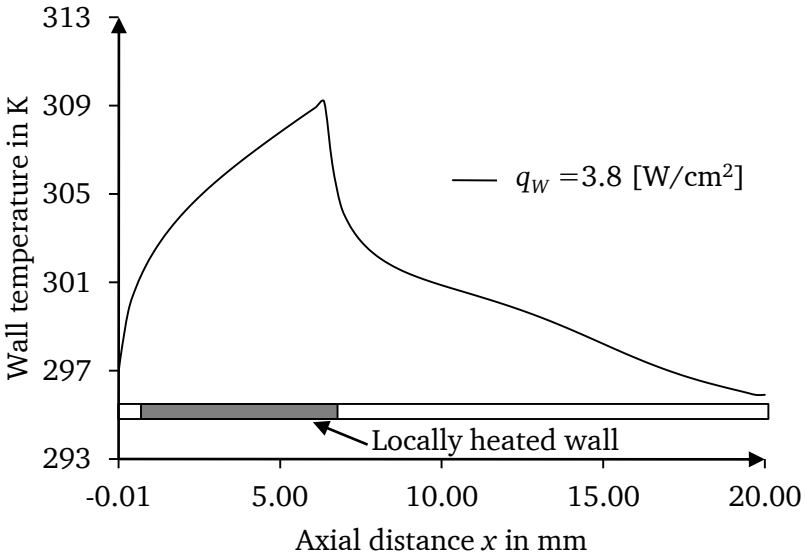

Figure 5.18: Wall temperature distribution in a locally heated shear-driven flow

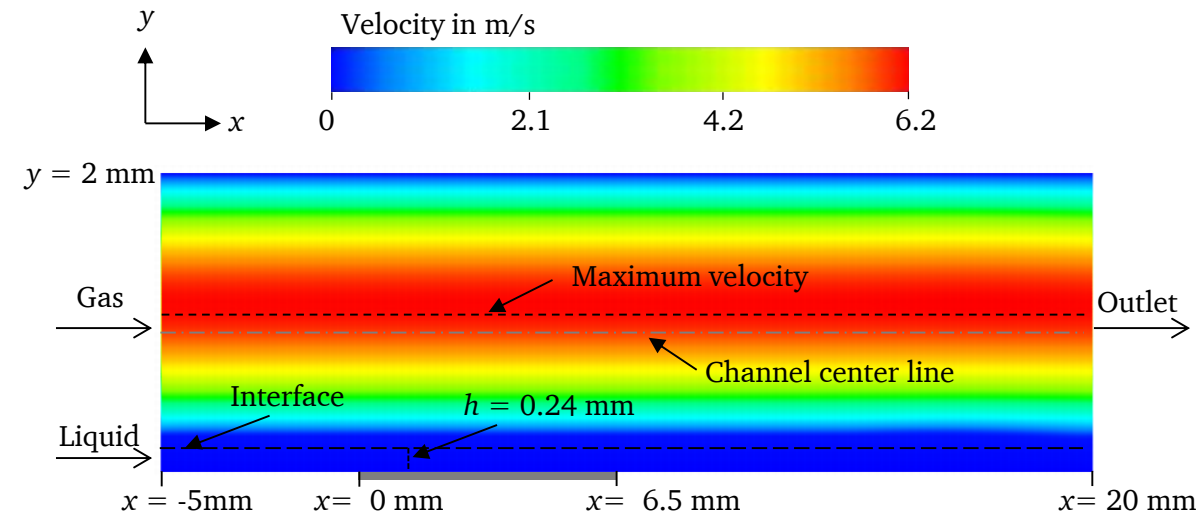

Figure 5.19: Velocity of magnitude in the gas-liquid phases of the stratified flow channel

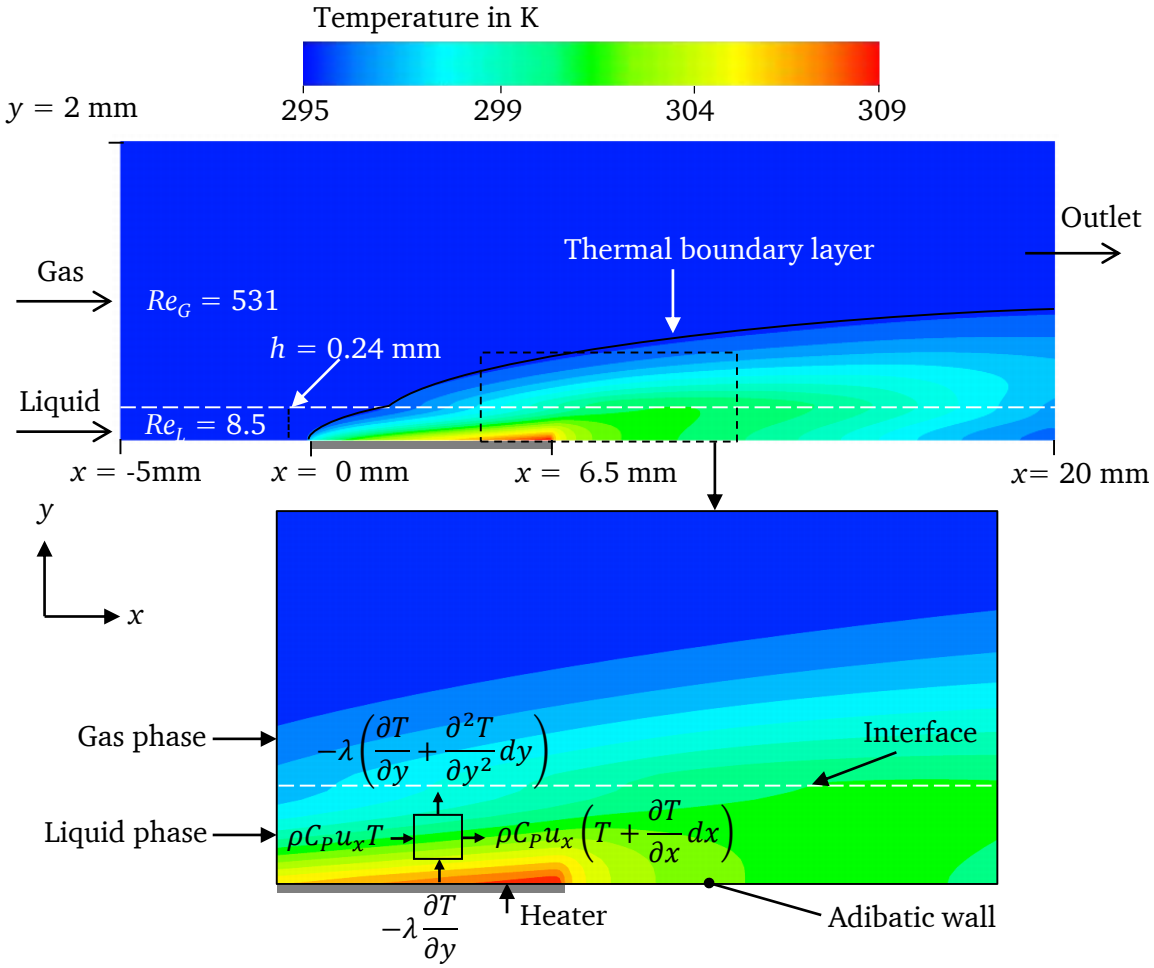

Figure 5.20: Temperature distribution in the gas-liquid phases at $Re_L = 8.5$, $Re_G = 531$ and a uniform heat flux $q_W = 3.8$ W/cm^2 (top). The zoomed contour of temperature distribution in the x-y plane (bottom). The white dashed line represents the gas-liquid interface. The black dashed line is the width of the thermal boundary layer

Figure 5.19 shows the magnitude of the velocity distribution in the 2D channel at $Re_L = 8.5$ and $Re_G = 531$. The black dashed line represents the gas-liquid interface with a film height of 0.24 mm. The maximum velocity in the channel is shifted above the centerline, because of the liquid film at the bottom of the channel. Figure 5.20 describes the temperature field in the 2D channel with a heat source of $q_W = 3.8$ W/cm^2 applied at the bottom of the channel. In this figure, the white dashed line indicates the gas-liquid interface, and the black dashed line represents the width of the thermal boundary layer. The thickness of the thermal boundary layer increases along with the distance from the wall. As can be seen in the figure, energy is transmitted from the wall to the liquid and further into the gas phase, increasing with the length of the channel.

5.4 Simulation of 3D geometry and comparison with in-house experimental data

Computational results of the shear-driven wavy film are compared with the experimental results in this section. Experiments have been performed in parallel with the current work in the framework of the Ph.D. project by Budakli [20]. In the experiments, the dynamics of the film thickness of shear-driven films were studied using the shadowgraphy method. Additionally, the gas velocity profile within a gas-liquid flow was also measured. This section presents and discusses the comparison of the numerical simulation results with the measurements of the hydrodynamic characteristics of a liquid film sheared by gas flow.

5.4.1 Experimental details

Figure 5.21 shows a schematic view of the experimental setup for the study of shear-driven thin liquid films. The liquid (water) is supplied from a reservoir by a frequency-controlled gear pump augmenting an absolute pressure up to 15 bar with a maximum mass flow rate of 0.025 kg/s. The inlet temperature of the liquid is controlled by electrically powered ceramic heaters. The liquid enters the test section through a film distributor head, creating a homogeneous thin film with an initial thickness of 425 μm in a ring-shaped channel. The liquid film flows along a surface of the 80 mm long heated tube with a diameter of 19 mm (see Figure 5.21). The tube is heated by a heating cartridge assembled in the tube center. This tube is located coaxially inside a 60 mm diameter channel. That way, an annular channel of 20 mm height is obtained. The thermocouples were inserted at a distance of 10 mm apart along the heated tube. For optical access, four quartz glass windows are provided on the channel. Air with an absolute pressure maximum up to 12 bar is supplied from a pressure vessel with a mass flow rate up to 700 kg/hr. The air stream passes in the channel along the thin film, thus accelerating the film flow.

To determine the average film thickness, the shadowgraphy method was used [54, 55]. The heated tube has been backlit with white light so that the shadows of the tube surface and the liquid film were projected onto the camera. The position of the wall-liquid interface was determined with a semi-automated program. Using the same method, the liquid-gas interface position was determined in each image recorded during the experiments. Finally, the film thickness for each image was calculated. The accuracy of these measurements was estimated to be ± 15 μm.

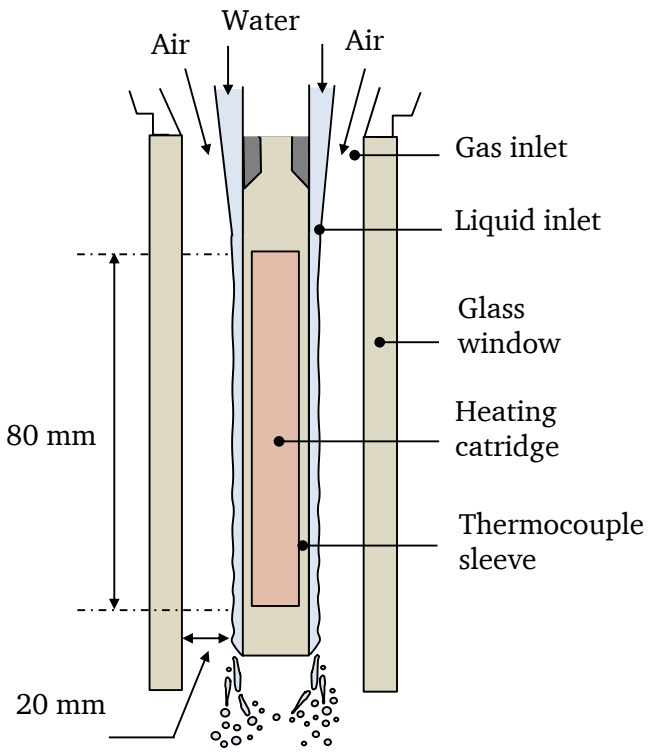

Figure 5.21: Schematic representation of the test section [20]

The liquid mass flow rate M_L was varied between 43 and 125 kg/hr with an uncertainty of $\pm 0.15\%$, and the gas mass flow rate M_G ranged between 48 and 450 kg/hr with an uncertainty of $\pm 1.5\%$. The experimental parameters set during the measurements such as the Reynolds numbers of the gas and liquid are provided in Table 5.5. In all the experiments, the inlet gas and liquid temperatures were maintained at a constant value of 24°C. The temperatures were measured at the positions $x = 35, 45, 55,$ and 65 mm from the liquid inlet using thermocouples, while the film thickness was measured only at a position of $x = 35$ mm. The gas velocity profiles were measured using the Pitot tube at $Re_G = 4\text{x}10^4$ and $Re_L = 525$ at $x = 30$ mm from the liquid inlet. In order to measure the average velocity in the channel, experiments were only run for an isothermal condition and at a pressure of 3 bar. Due to the experimental constraints, the minimal distance between the wall and the measurement point could only be set 5 mm away from either side of the wall. The accuracy of the velocity measurements was estimated to be ± 0.12 % of the reading [20]. The Reynolds numbers of the gas and liquid are defined using the following relations [20]:

$$Re_G = \frac{M_G}{P_G \mu_G}, \tag{5.19}$$

$$Re_L = \frac{M_L}{P_L \mu_L}, \tag{5.20}$$

where M_G and M_L are the mass flow rates of the gas and liquid phases, respectively, while μ_G and μ_L are the dynamic viscosities of the gas and liquid. The circumferential perimeters of the test channel, P_G and P_L, are calculated using the following definitions:

$$P_G = \pi d + 4a + c\,, \tag{5.21}$$

$$P_L = \pi d. \tag{5.22}$$

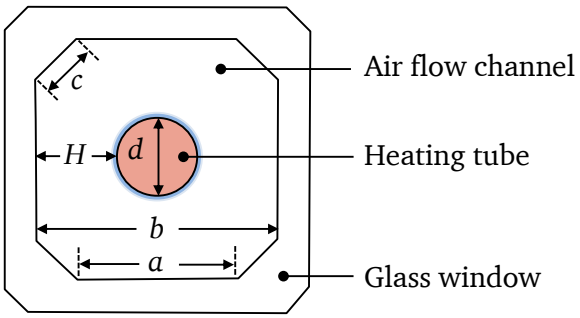

Figure 5.22: Schematic cross-sectional top view of the experimental set-up [21]

Table 5.5: Experimental parameters

Re_L	Re_G	q_W (W/cm^2)
375	10^4	
525	4×10^4	20
650	7×10^4	

5.4.2 Numerical model

Geometry and numerical grid

The initial film thickness (~500 μm) considered during the experiments was very small compared to the channel diameter (~20 mm). Capturing such a small film thickness requires a very fine grid. This increases the demand on computations immensely, making practical three-dimensional computations (Figure 5.23) extremely time consuming. Therefore, in this work, a three-dimensional model of one-eighth (45° sector) of the test channel has been used in order to simplify the model and save computation time. Figure 5.24 presents the three-dimensional computational domain, representing a one-eighth part of the experimental fluid domain. A one-eighth part was chosen since the geometrical cross-section in the experimental rig was octahedral in shape (see Figure 5.22).

Modeling the two-phase flow using the low Reynolds number k-ε turbulence model requires a very fine grid resolution near the wall. The non-dimensional distance of the first grid center from the

wall y^+ should be of a unity order. Since the y^+ value depends on the fluid flow solution, it can only be confirmed after solving with the estimated value from Equation (3.42).

Therefore, the refinement of the mesh to achieve the low y^+ value is an iterative process. The procedure consists of initially producing an arbitrary mesh, refining the mesh near the wall region and then repeating the process using the new mesh. The meshing tool (meshing routine function and snappy hex-mesh tool) used for this project did not have any sophisticated geometry nor meshing capabilities for complex models, and therefore the commercial tool Ansys-ICEMCFD was utilized for the creation of hexahedral elements. The mesh created in Ansys-ICEMCFD was exported to OpenFOAM for further simulation [106].

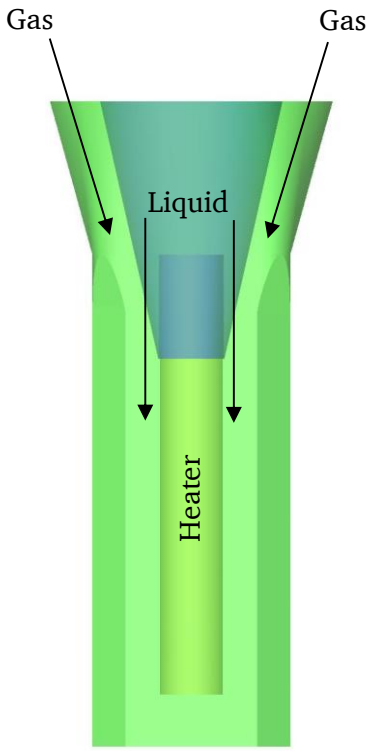

Figure 5.23: Computational CAD model for the two-phase flow simulation (3D fluid domain geometry)

The design and distribution of the hexahedral control volumes in a numerical domain is very important. Moreover, the control volumes need to be small enough to be able to resolve the significant length scale of the flow. In general, a more complex flow with large gradients needs more mesh elements but leads to high computational expenses and requires longer simulation time. A meshing strategy is adopted to generate a denser mesh where large gradients are expected and to decrease the total number of mesh elements in areas where the flow calculation is less sensitive to the grid size.

The first grid point from the wall in the y-direction is defined based on the y^+ value; therefore, several different meshes were used ranging from 150,000 to approximately 300,000 elements, depending on the flow conditions. Figure 5.25 illustrates a cut section of this mesh through the shear-driven film flow channel. The mesh density in the gas phase's middle region is maintained

coarse to reduce the overall number of mesh elements. For the near wall region and at the interfacial area, the refinement leads to greater influence on the results. Therefore, a very high mesh density is set near the wall region and in the interfacial domain. The grid elements used in this computation are hexahedral. The near-wall region up to 1 mm is uniformly meshed with a higher number of elements, and the mesh elements in the gas phase are adjusted by a varying aspect ratio.

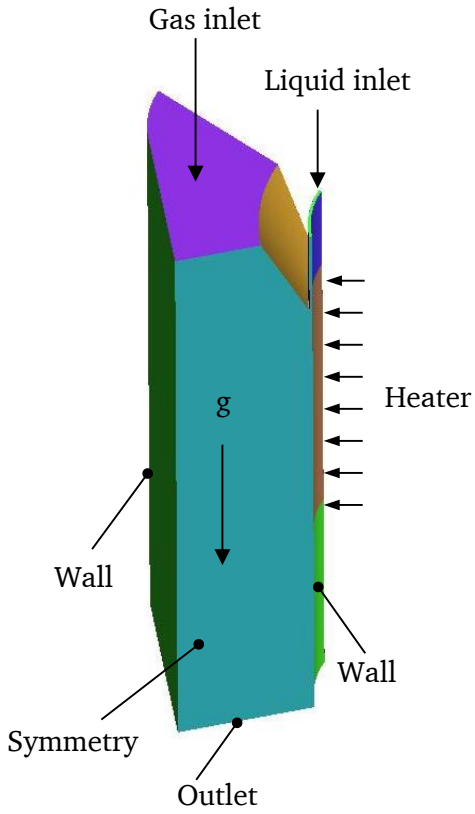

Figure 5.24: Three-dimensional computational model of a 45° sector and the boundary conditions

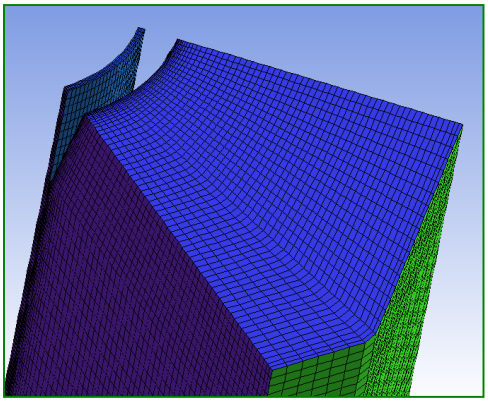

Figure 5.25: Computational grid view of the Ansys ICEM-CFD mesh used for 3D simulations

Boundary conditions

Setting the boundary conditions is a sensitive part of numerical simulations, as they are key factors determining the simulation results. The boundaries of the flow channel are shown in Figure 5.24. The front side of the channel, where the fluid enters the domain, is divided into two parts, namely the liquid inlet and the gas inlet, respectively. The exit of the channel, where the fluid leaves the channel, is named the outlet. The left and right boundaries (cut section) of the channel are considered as symmetry planes, while the remaining surfaces are represented as wall boundaries. The complete boundary conditions are listed in Table 5.1, excluding the velocities. The velocities correspond to the gas and liquid mass flow rates measured during the experiments. In this study, the gas and liquid Reynolds numbers were varied between 10^4 – 7x10^4 and 300 – 650, respectively. Table 5.6 lists the velocities corresponding to the different gas and liquid Reynolds numbers.

Table 5.6: Inlet velocities for the gas and liquid phases

Fluid	Reynolds number	u_x (m/s)
Gas	10^4	2.3
	4×10^4	8.3
	7×10^4	15.2
Liquid	375	0.6
	525	1.0
	650	1.4

The present study uses a low Reynolds number k-ε model for turbulent simulations. Therefore, two additional boundary conditions are defined for the turbulent kinetic energy k and the dissipation rate of the turbulent kinetic energy ε, respectively. The turbulent kinetic energy (k) and dissipation rate (ε) at the inlet are applied based on the following equations:

$$k = \frac{3}{2}(|\bar{u}|I)^2, \tag{5.23}$$

$$\varepsilon = C_\mu^{3/4} \frac{k^{3/2}}{l}. \tag{5.24}$$

where $C_\mu = 0.09$. A turbulent intensity $I = 10\,\%$ and a turbulent length scale l up to 7 % of the hydraulic diameter are imposed [148]. The turbulent boundary conditions are specified in Table 5.7. The inlet conditions of the turbulent properties depend on the Reynolds numbers of the gas and liquid, and they are listed separately in Table 5.8.

Table 5.7: Turbulent boundary conditions

Boundary	Value
Gas and liquid inlet	Values from Equations (5.23) and (5.24)
Outlet and symmetry	$\partial k / \partial n = 0$ and $\partial \varepsilon / \partial n = 0$
Walls	$k = 0$ and $\varepsilon = 0$

Due to the no-slip condition on the wall boundaries, the turbulent kinetic energy is considered to be zero at the walls of the flow channel. However, during the computation, an equation might be divided by the value of k, which is zero. Thus, the magnitude of k at the wall boundaries is fixed with a small value in order to avoid errors during computation. The gradient of the turbulent kinetic energy is zero at the outlet boundary. For the dissipation rate of the turbulent kinetic energy, a zero value is assumed at the walls.

Table 5.8: Turbulent properties at the inlet for the gas and liquid phases

Fluid	Reynolds number	ε (m^2/s^3)	k (m^2/s^2)
Gas	10^4	0.12	0.021
	4×10^4	5.39	0.258
	7×10^4	34.36	0.878
Liquid	375	0.01	1.4×10^{-3}
	525	0.55	4.1×10^{-3}
	650	1.07	6.7×10^{-3}

For the initial conditions, all the cells in the domain were set to a uniform pressure value of 0 Pa (constant relative pressure) and a temperature of 294 K. The volume fraction $\gamma = 1$ is maintained up to the level of the initial film thickness, and velocities are kept uniform in the channel. The gravitational acceleration acts in a stream-wise direction (positive x direction). In the numerical simulations, air and water were chosen as working fluids corresponding to the in-house experiments [20]. The inlet temperatures of water and air are maintained at 294 K. The temperature gradient derived from the uniform wall heat flux is imposed on the "heater" wall, which is calculated using the value of $q_W = 20\ \mathrm{W/cm^2}$. The boundary conditions specified in the simulations are listed in Table 5.1 and Table 5.4. While thermo-physical properties in the simulations are specified in Table 5.2 and Table 5.3, these properties are obtained at 1 bar pressure and at a temperature of 294 K. In order to simulate the turbulent heat transfer, the turbulent Prandtl number is chosen with a value of 0.9 [121].

Transient simulations are performed until the wall temperature reaches a quasi-stationary behavior. During simulation, wall temperatures at various positions on the x coordinates are stored against simulation time. Figure 5.26 shows the temperature variation during transient computation. The wall temperatures first increase up to 0.1 s and stabilize after 0.2 s. The wall

temperatures saturate from 0.25 s to 0.5 s, and therefore, transient simulations for all cases are performed until 0.3 s.

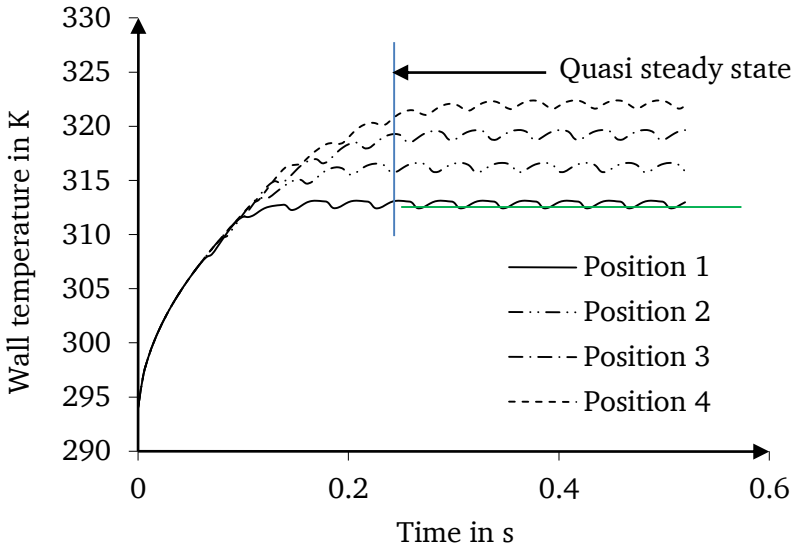

Figure 5.26: Transient temperature evolution during computation

5.4.3 Comparison of velocity profile, film thickness and wall temperature

The validation of the numerical method with the experimental data is undertaken by comparing the measured liquid film thickness, the wall temperature distribution, and the velocity distribution in the gas with the numerically predicted values.

Average film thickness

Figure 5.27 shows a comparison of the predicted average film thickness with that of the thickness measured at 35 mm from the liquid inlet for three experimental runs. These runs correspond to different Reynolds numbers of the liquid. In this figure, filled diamond shapes and empty triangles represent the experimental and computational results, respectively. It can be seen from Figure 5.27 that the computed average film thickness at $Re_L = 375$ is 10% higher than the average film thickness measured using the shadowgraphy method. One reason for this disagreement can be attributed to the slight deviation from a symmetric film distribution over the tube circumference in the experiment. Moreover, there are significant fluctuations in the instantaneous film thickness measurement.

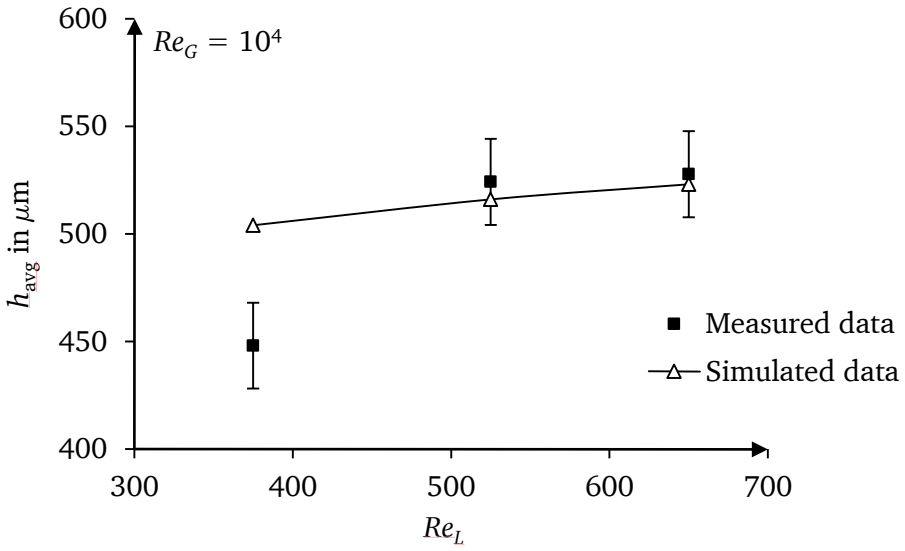

Figure 5.27: Average film thickness distribution at various liquid Reynolds numbers

Velocity profile

Figure 5.28 presents the measured (circles) and predicted (curve) axial air velocity profiles at a distance of 30 mm from the liquid inlet. In general, the predicted results exhibit reasonable agreement with the experimental data. The velocity profile in the liquid phase follows a semi-parabola distribution, and the location of the maximum velocity appears at the interface.

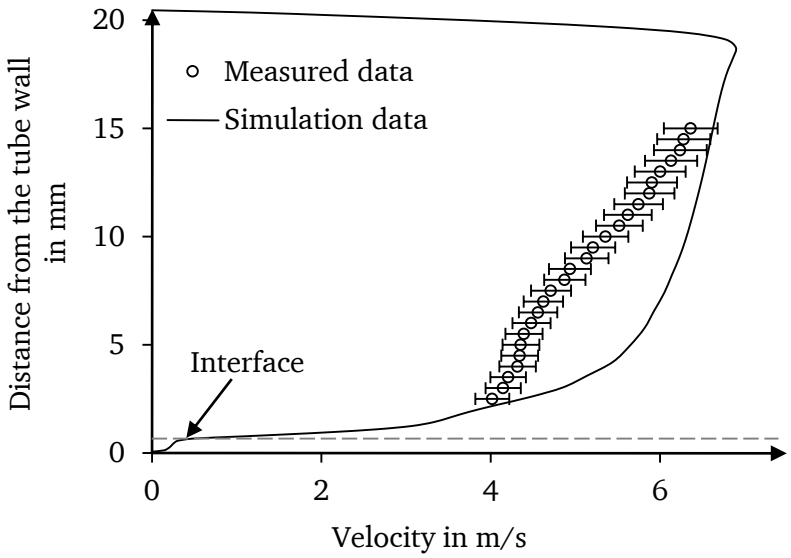

Figure 5.28: Measured and simulated velocity profiles at $Re_L = 525$ and $Re_G = 4\times10^4$ at a position $x = 30$ mm

The discrepancies seen in Figure 5.28 can be attributed to the non-uniform distribution of the air velocity at the entrance of the channel (Figure 5.23). This deviation may also be due to the assumption of the 45° sector of geometry considered in the numerical model (Figure 5.24). This is likely due to the inlet region's real geometry, where the inlet flow passes with the swirling gas within the flow field of the channel. Flow visualization experiments also revealed fluctuations in the liquid film thickness due to large waves, which may be the dominant phenomenon in wavy films. The co-current interfacial shear increases the turbulent intensities in the liquid film, and its effect on the velocity variation in the gas flow field is especially significant. The liquid film becomes turbulent and wavy, leading to a flat velocity profile in a significant portion of the gas, clearly visible in Figure 5.28. The effect of the interfacial waviness on the stream-wise velocity fluctuations and the heat transfer enhancement will be discussed in Section 5.5.

Wall temperature distribution

The simulated wall temperature distribution is plotted against the axial distance in Figure 5.29. The experimental data are plotted using the filled diamond shapes, and the computed results are plotted by a continuous line with triangles. The temperature of the wall increases in the downstream direction.

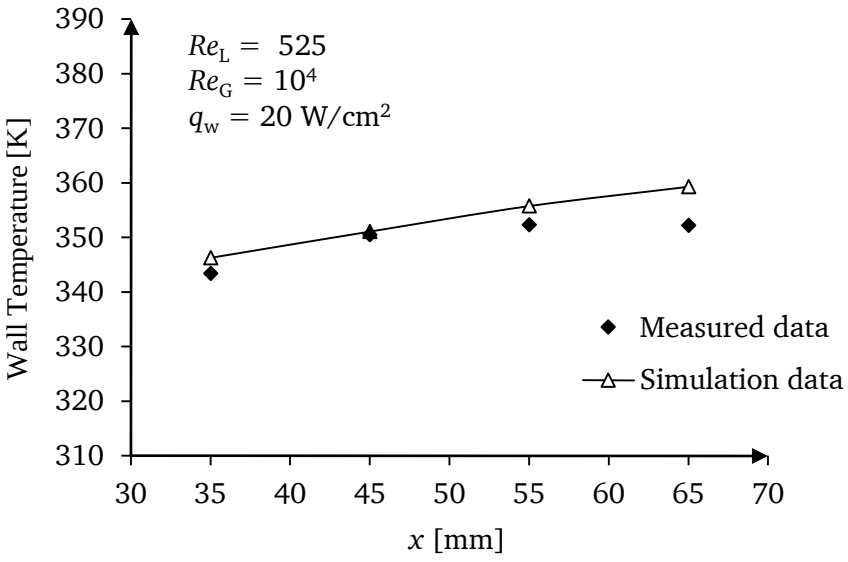

Figure 5.29: Comparison of the computed wall temperature distribution with measurements ($Re_G = 10^4$, $Re_L = 525$ and $q_W = 20$ W/cm^2)

The agreement between the experimental and numerical data is rather good. However, starting from a certain position, the measured wall temperatures stay unchanged with increasing distance from the entrance. In this region at the bottom of the channel, the numerical simulations over-predict the experimental data on the wall temperatures. The discrepancy can be attributed to two phenomena: Firstly, heat losses were not taken into account in the simulations, only a uniform wall heat flux is assumed at the tube wall. During experiments, convection between the setup and

the ambient air could have resulted in heat losses. Additional heat losses may have resulted from axial conduction in the tube and in the heating cartridges. Secondly, the evaporation of water into the flowing air was not included in the model. In this study, the complex structure of the geometry is modified to maintain the structured hexahedral elements. Figure 5.30 shows the downstream of the channel flow with the curved portion at the outlet region. Therefore, the geometry also affects the variation in pressure near the channel's outlet region. This variation in pressure also influences the heat transfer in the channel.

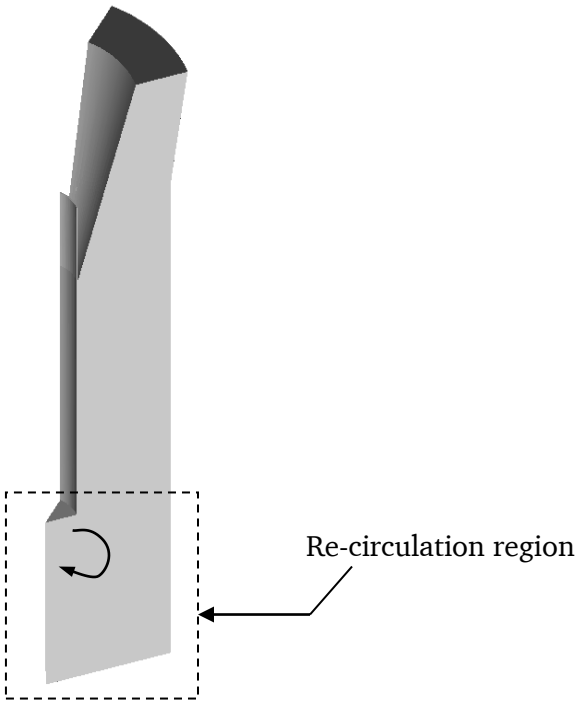

Figure 5.30: Three-dimensional model of 45° sector with the bottom zone which is not included in the computational domain

5.4.4 Three-dimensional results analysis

Figure 5.31 refers to the simulated 3D model at an air velocity of 20 m/s ($Re_G = 8 \times 10^4$), a water speed of 1 m/s ($Re_L = 525$), and $q_W = 20$ W/cm^2. The simulations are performed with the inlet film thickness of 500 μm. The velocity contour plot is presented for the central y-z section plane ($x = 0$ mm). Figure 5.32 illustrates the source of disturbance of the film flow. Figure 5.33 shows the liquid volume fraction distribution at different positions in the 3D channel. The close-up view of three locations with the liquid film volume fractions is also visualized in this figure.

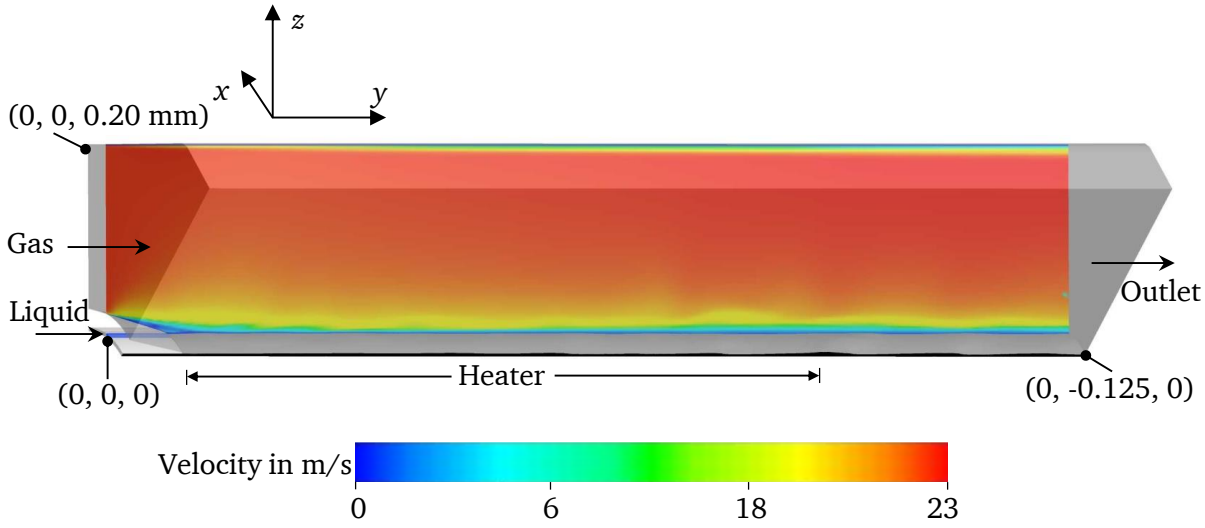

Figure 5.31: Velocity magnitude distribution of air and water on an iso-surface (y-z mid plane) in the 3D channel at u_G = 20 m/s and u_L = 1 m/s in the 3D simulation

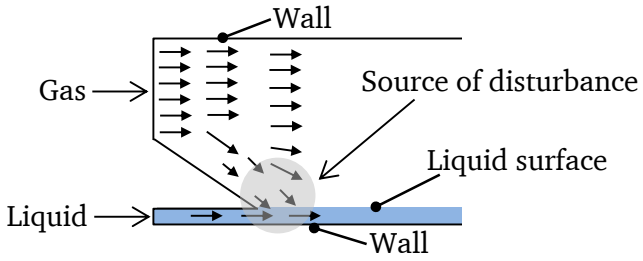

Figure 5.32: Schematic of the source of the disturbance for the liquid film

Figure 5.34 shows the variation of the liquid film in three section planes in the 3D model. It can be seen that the wave amplitude increases up to 720 μm in plane-3 while there are low amplitude waves in the plane 2. The location of the maximum amplitude position is different in these three plane cross-sections. In addition, the shapes of the interface at three locations are different, and they influence the degree of the flow pattern in the channel. The interface is clearly three-dimensional with significant variation in the span-wise direction. The waves are most prominent in planes 1 and 3, decreasing towards the middle of plane 2.

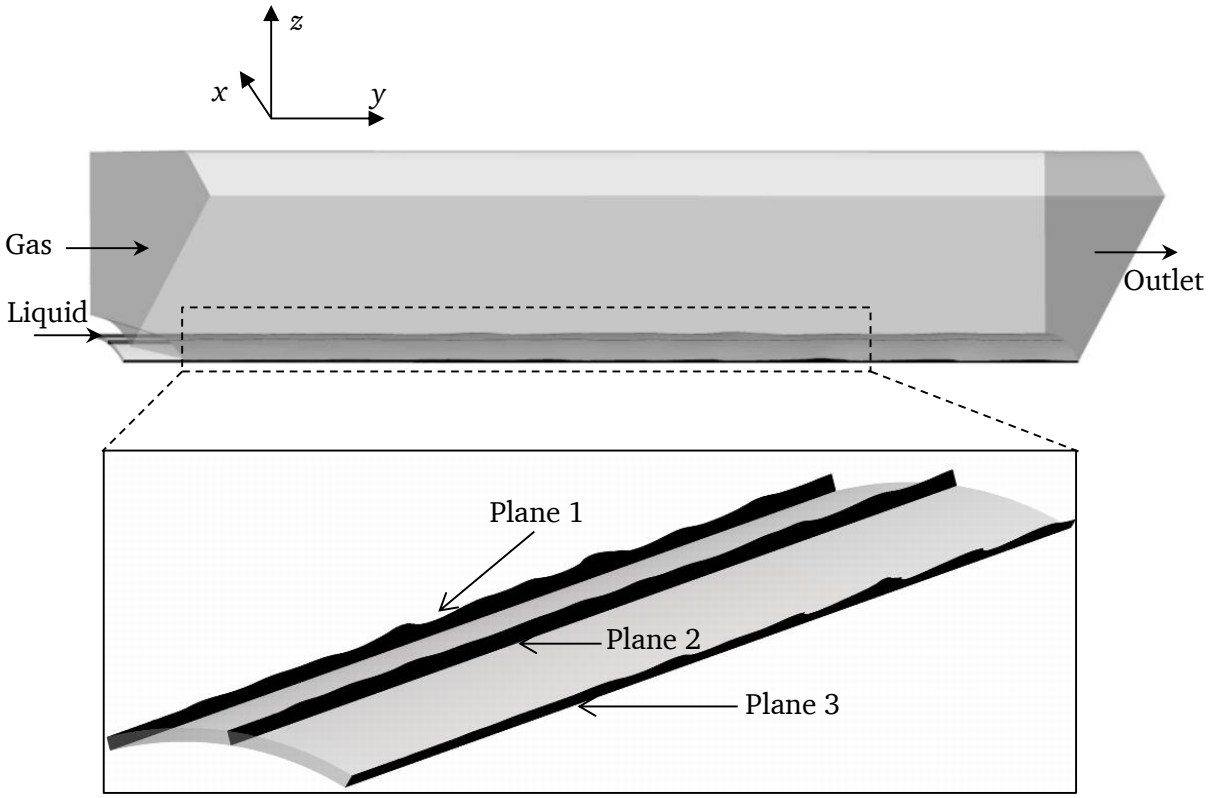

Figure 5.33: Liquid volume fraction distribution at three different locations in the 3D channel

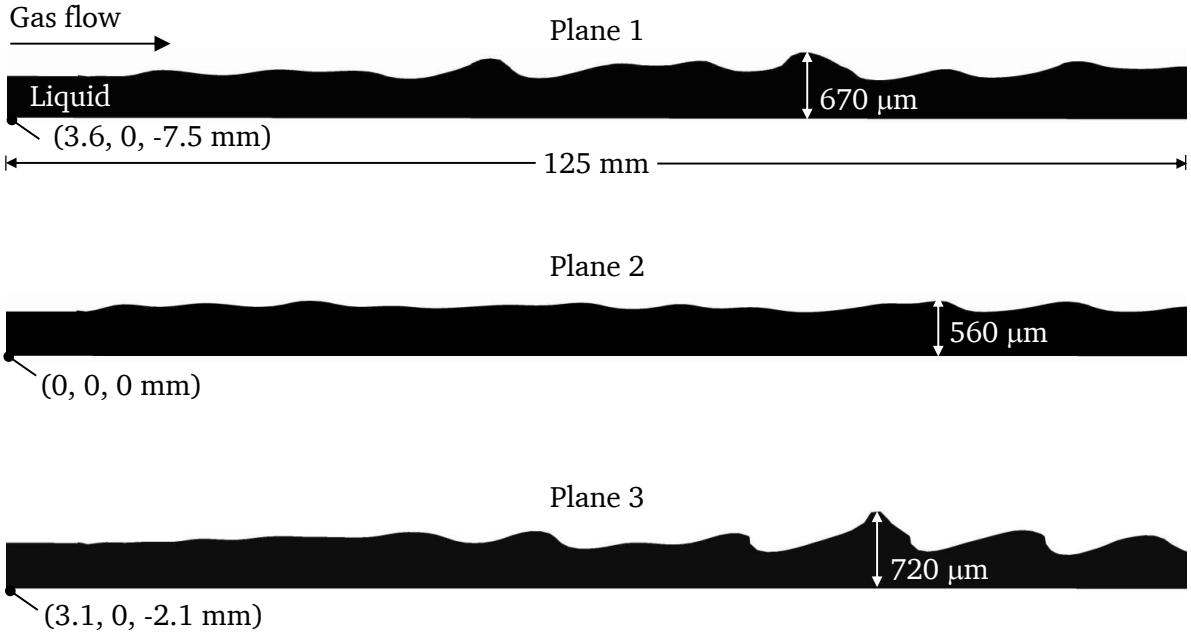

Figure 5.34: Liquid volume fraction distribution at three planes in the 3D channel with the details of locations and amplitudes (scaled)

Figure 5.35 shows the influence of the 3D wavy film on the liquid surface velocity and the wall temperature fields. The velocity field on the iso-surface of the liquid film is computed at a volume fraction of 0.5. The zoom views (right side of Figure 5.35) of the clipped planes are presented to get a clearer view inside the 3D channel. The span-wise wave pattern in the flow region shows the intermediate peaks of the liquid film (see Figure 5.35). The higher velocities are located on the upper regions of the wavy film. The span-wise temperature distribution is affected by wave-induced mixing in the liquid film.

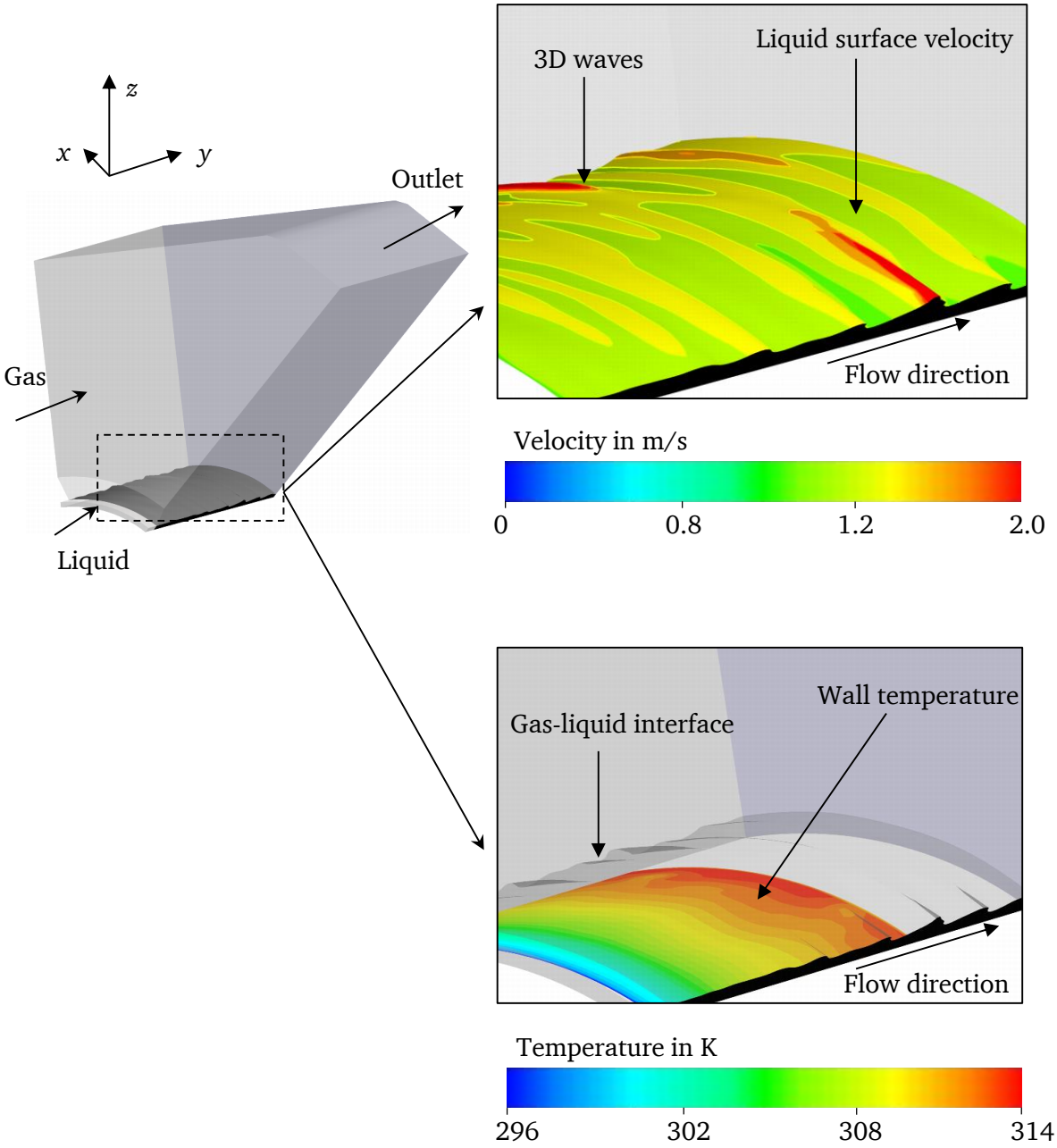

Figure 5.35: Liquid superficial velocity magnitude distribution (right top) and wall temperature distribution (right bottom) in the 3D channel at $Re_G = 8x10^4$ and $Re_L = 525$, $q_W = 20$ W/cm^2

Figure 5.36 depicts the flow pattern in 3D view at 85 mm from the inlet of the 3D channel. The cross-section plane (x-z) is orthogonal to the flow direction. This positioning is used to clearly show the gas phase velocity variation in the span-wise direction (azimuthally). It is observed that the gas velocity is non-homogeneous due to the wavy surface (roughness) of the liquid film. The gas velocities are higher along the crests of the large waves and lower along trough regions. As a conclusion, it is to be emphasized that both three-dimensionality and wave interactions strongly affect the flow structure throughout the entire flow channel.

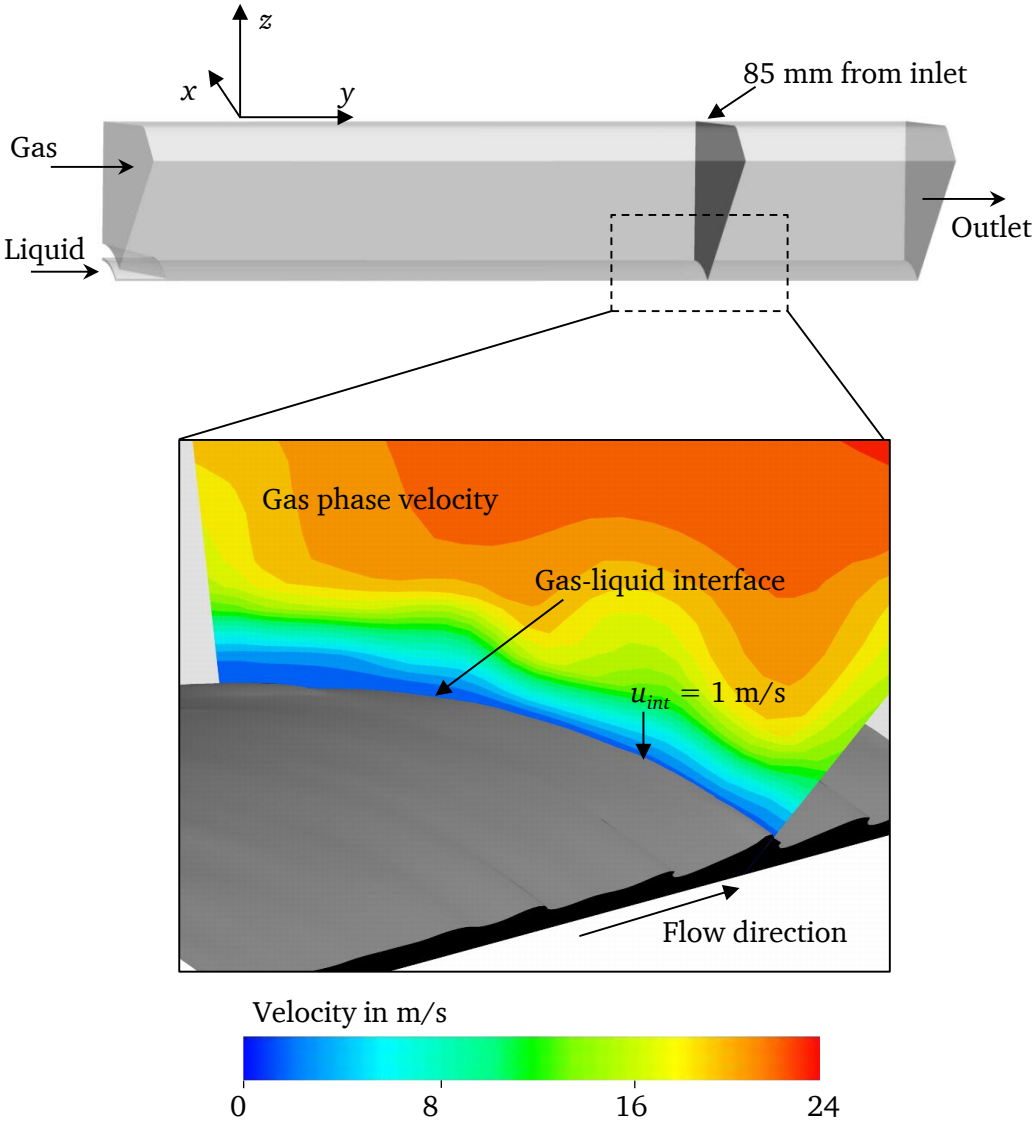

Figure 5.36: Gas phase velocity magnitude distribution (bottom) at 85 mm from the inlet on the x-z plane section in the 3D channel at $Re_G = 8\text{x}10^4$ and $Re_L = 525$

5.5 Parametric analysis

This section discusses the computational results of a parametric study on gas-liquid flows. The influence of the wavy film flow on the heat transfer for thin liquid films driven by a gas is investigated. Numerical simulations were carried out for the shear-driven wall liquid film at various inlet flow parameters. In order to evaluate the influence of the gas and liquid Reynolds numbers on the hydrodynamics and heat transfer in shear-driven liquid films, a series of simulations is performed in a two-dimensional flow geometry (Figure 5.37). The reference pressure was chosen as 1 bar. The new configuration is considered for parametric study to reduce computational efforts, as the computational domain used to validate the numerical model through comparison with experiments is less suited for parametric study due to special geometrical features (see Figure 5.23). For all computations, the simulation time was maintained up to 0.3 s when the temperature reached a quasi-steady state.

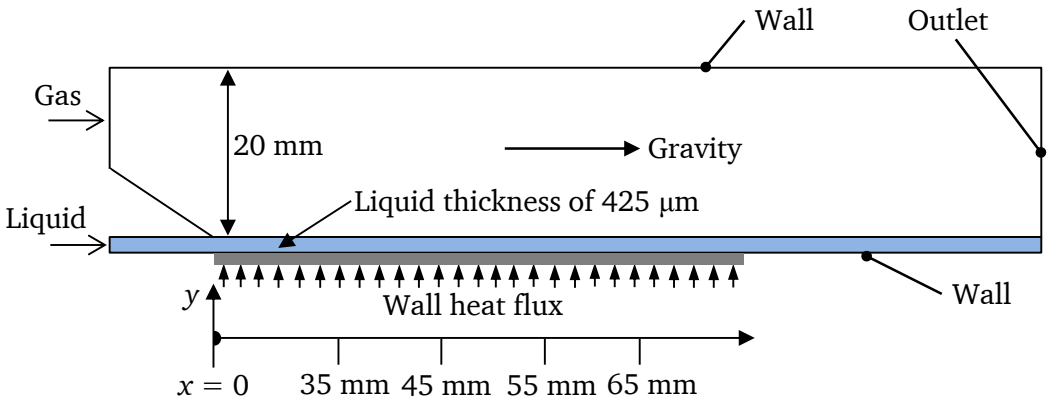

Figure 5.37: Two-dimensional computational domain with initial and boundary conditions for parametric analysis

5.5.1 Effect of the gas and liquid Reynolds number on heat transfer

The study on the variation of the wall temperature in a channel is performed for various values of gas Reynolds numbers by maintaining a constant liquid flow rate. Figure 5.38 presents the simulation results for the wall temperature distribution for a fixed liquid film flow rate ($Re_L = 525$) and the set gas Reynolds numbers $Re_G = 10^4$, $Re_G = 4\times10^4$ and 7×10^4. The wall heat flux is kept constant at 20 W/cm^2. It can be seen from Figure 5.38 that the wall temperature decreases with increasing gas flow rates, indicating enhanced heat transfer because of forced convection. For a particular liquid Reynolds number, a rising gas flow rate results in the shear increasing at the interface, the flow accelerating within the liquid film, and the convective heat transport intensifying in the system. The higher gas velocity leads to a decrease in the film thickness and an increase in the liquid velocity. As a result, convection heat transfer between the wall and the liquid intensifies. Moreover, the raised average gas velocity corresponds to the increase of the convective heat transport between the liquid and the gas. As seen in Figure 5.38, the axial temperature gradient becomes less steep with increasing gas Reynolds numbers.

The effect of the liquid Reynolds number on the wall temperature profile is illustrated in Figure 5.39. The plotted wall temperature data has been simulated for three different liquid Reynolds numbers (Re_L = 375, 525 and 650) at a fixed value of the gas Reynolds number ($Re_G = 10^4$) and at a uniform wall heat flux (q_W = 20 W/cm^2). Figure 5.39 shows that as Re_L decreases, the wall temperature rises at each axial position. The strong influence of the inlet liquid Reynolds number on the temperature profiles can be seen in Figure 5.39. Temperatures on the wall are lower for higher liquid Reynolds numbers. This change in temperature can be attributed to the intensification of the convective heat transport when increasing the liquid mass flow rate. For a fixed Re_G and increasing Re_L, the liquid velocity increases additionally cause the heat transfer to intensify.

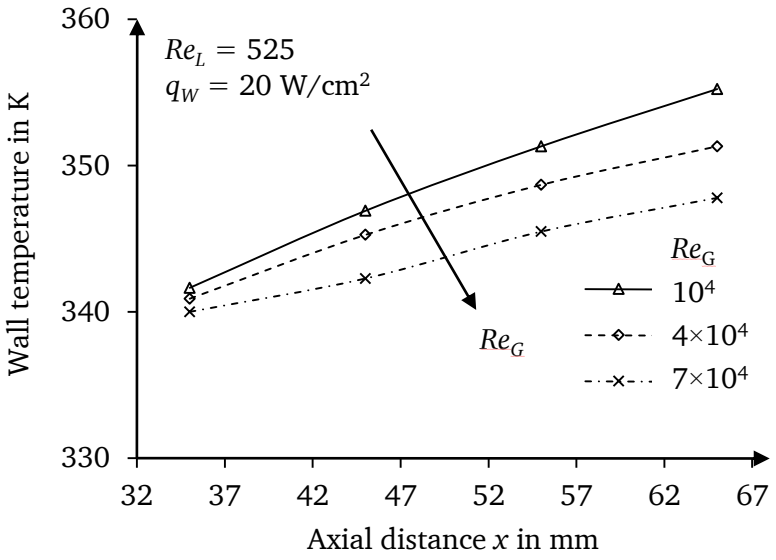

Figure 5.38: Wall temperature distribution in stream-wise position at Re_L = 525, q_W = 20 W/cm^2

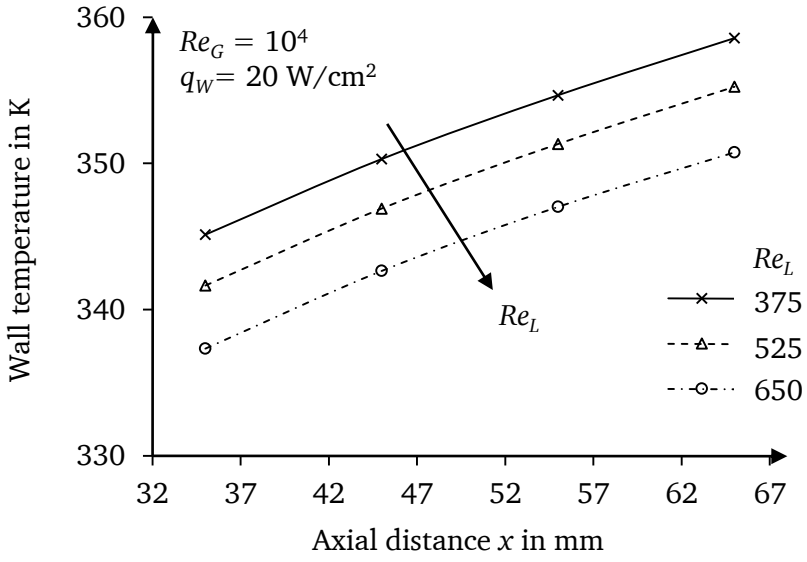

Figure 5.39: Wall temperature distribution in stream-wise position at Re_G = 10^4, q_W = 20 W/cm^2

Figure 5.40 represents the velocity profiles at x = 40 mm from the inlet in the region $0<y<1$ mm at different liquid Reynolds numbers and the constant gas Reynolds number $Re_G = 10^4$. One part of each velocity profile adjacent to the wall corresponds to the liquid, and another part corresponds to the gas. The liquid-gas interface is characterized by a jump of the velocity gradient. It can be observed that the velocity profile in the liquid film expresses a semi-parabola profile, while the maximum velocity appears to be located at the interface. As shown, an increase in the liquid mass flow rate leads to the average liquid velocity rising, and ultimately to the film thickness growing. The liquid film thickness increases due to a rise in the mass flow rate for high liquid Reynolds numbers [95, 96].

Figure 5.41 shows the velocity profiles for $Re_G = 7\text{x}10^4$ and $4\text{x}10^4$ at constant Re_L. The film thickness can also be determined from the velocity profile, with a sudden change in the velocity gradient located at the interface region. The velocity speeds up rapidly above the liquid surface. The boundary layer's velocity can be seen to increase with a rising Re_G, which is due to the higher velocity gradient, leading to higher shear forces. Simultaneously, the height of the liquid film also lowered due to waviness.

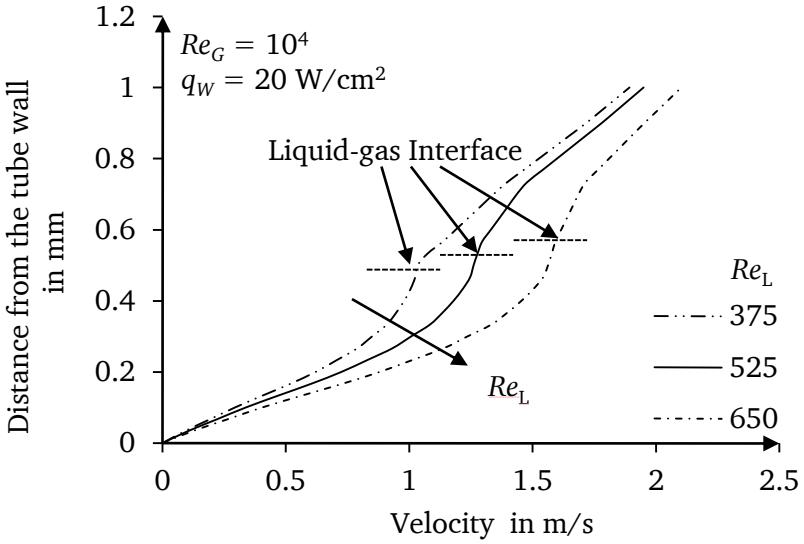

Figure 5.40: Velocity profiles (x-component) at x = 40 mm at $Re_G = 10^4$, $q_W = 20$ W/cm^2

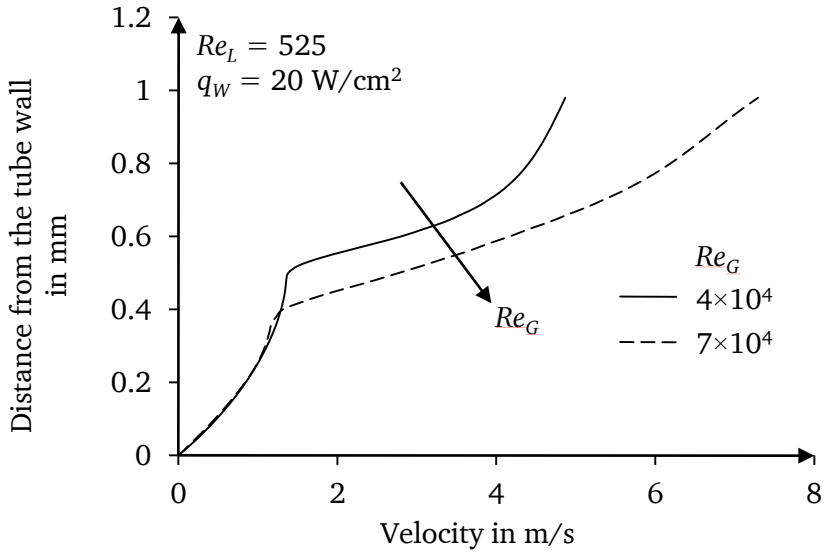

Figure 5.41: Velocity profiles at a distance from the inlet and at $x = 55\ mm$ and $Re_L = 525$

5.5.2 Temporal variation of film thickness

The results obtained in the previous sections demand a detailed investigation of instantaneous film thickness calculated in the present study. This would allow for a better understanding of the transient effects of the film thickness fluctuations, which would provide further insights into the hydrodynamics of shear-driven films. Figure 5.42 shows the computed temporal variation of the instantaneous film thickness at $x = 35$ mm. The simulations have been performed at the constant liquid Reynolds number $Re_L = 650$ and three different values of gas Reynolds numbers.

At a gas Reynolds number of 10^4, a regular wave pattern region with a small amplitude and an interface covered by regular two-dimensional waves is observed. This kind of flow is determined mainly by the liquid viscosity and the surface tension. With an increasing gas Reynolds number up to $Re_G = 4\times10^4$, the wave amplitude significantly increases. As the Reynolds number rises, an increase in the frequency of waves is noticeable due to the high velocities. Accordingly, the velocity fluctuations strengthen in both the gas and liquid phases. Large-amplitude waves with irregular amplitudes in the liquid phase are seen in Figure 5.42. The instabilities occur on the liquid film due to the shear force at the interface by the velocity difference (at $Re_G = 4\times10^4$) which is exhibited across it. This leads to Kelvin–Helmholtz instability, a kind of instability which causes waves to be generated on the liquid surface.

At a higher gas Reynolds number ($Re_G = 7\times10^4$), irregular and large amplitude waves are present. Furthermore, at a high gas Reynolds number, the intense shearing effect on the surface of the liquid layer leads to velocity fluctuations, increasing the interfacial wave amplitude. At high gas velocities, two-dimensional waves appear at the interface of a co-current gas-liquid flow (see Figure 5.42). These two-dimensional wavy films are similar to the results reported in [6].

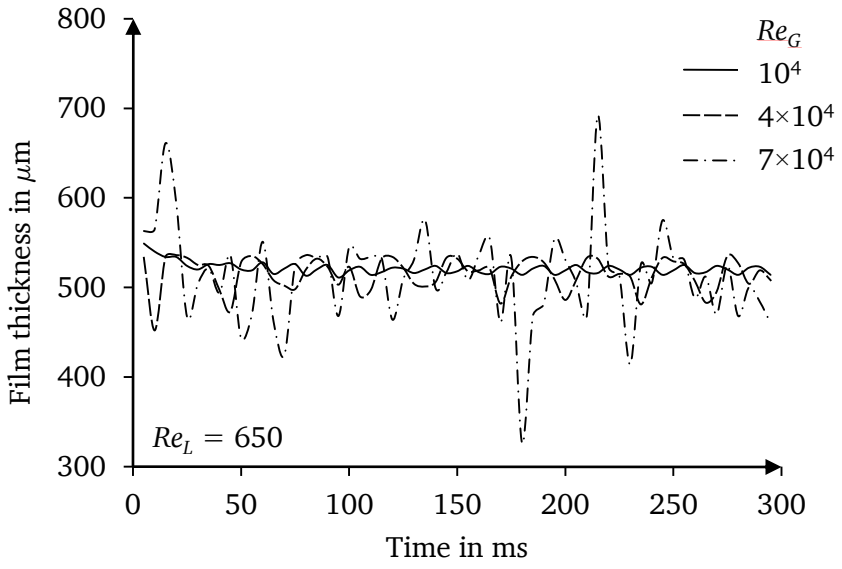

Figure 5.42: Temporal variation of film thickness at position $x = 35$ mm

5.5.3 Effect of input flow parameters on two-phase flow patterns

Figure 5.43 shows the wavy film contours (dark black color) at $Re_L = 525$ and three different values of the gas Reynolds number. The instabilities are generated due to the high interfacial shear force caused by the gas flow. These instabilities lead to the development of wavy film flow. The waves are amplified in the stream-wise direction. It can be observed from Figure 5.43 that the liquid film is smooth over the most part of the domain at lower gas Reynolds numbers, while it is characterized by the wavy irregular amplitude at higher gas Reynolds numbers. At a gas Reynolds number of $Re_G = 10^4$, the gas flow has no obvious effect on the liquid film near the inlet, with no fluctuations at 50 mm from the liquid inlet as depicted in Figure 5.43. At a low gas Reynolds number, the film surface is fairly smooth. Interfacial waves start developing further downstream at $x = 75$ mm from the liquid inlet. In the wavy region, interfacial waves affect the hydrodynamics of the film.

Figure 5.43 illustrates that increasing the gas velocity ($Re_G = 7\times10^4$) will intensify the drag force in the interfacial region. In addition, the drag force further decreases the interface velocity, as presented in Figure 5.46. At a higher gas Reynolds number, the co-current interfacial shear strengthens the turbulent intensities significantly. The successive waves of different amplitudes result from the high shear force at the interface. A comparison of the film thickness at various gas Reynolds numbers indicates drastic changes in the hydrodynamic structures of the liquid film due to the co-current interfacial shear. In fact, while the interfacial shear is applied to the film, the wave amplitude is altered due to the local turbulence and mixing. Therefore, the liquid film behaves as a turbulent film even at a gas Reynolds number of 10^4. Miya et al. [100] reported similar observations in horizontal films driven by a co-current gas flow. Dukler [31] proved the evidence related to associating turbulence with the local Reynolds number in two-phase flows. Brauner [19] also mentioned that turbulence might be initiated in the liquid film even at a low Reynolds number, with turbulence dominating in the wave region, while the thin substrate film would be laminar. These large and irregular waves are beneficial for convective heat transport in

liquid films. The difference in the wavy structure between the cases $Re_G = 10^4$ and $Re_G = 7\times10^4$ demonstrate enhanced heat transfer for the higher gas Reynolds number as shown in Figure 5.44.

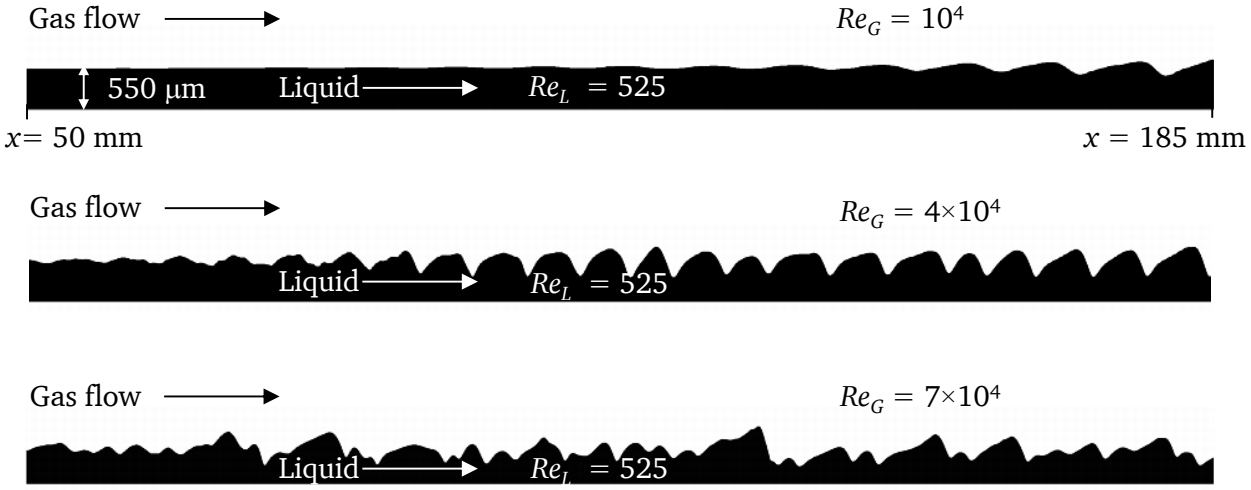

Figure 5.43: Volume fraction contours of the two-phase flow at $Re_L = 525$ for three different gas Reynolds numbers

The computational results on the interfacial wave characteristics have clearly indicated that the fluctuation amplitude changes as a function of the magnitude of co-current interfacial shear applied at the gas-liquid interface.

5.5.4 Flow and temperature field in a wavy film region

The interfacial wave form and the internal flow structure of wavy liquid film at the position of $x = 52$ mm from an inlet are analyzed in detail. Figure 5.44 shows the liquid film (volume fraction) for the gas flow over a thin liquid film at $Re_G = 7\times10^4$ and $Re_L = 525$ at a time instant $\tau = 0.33$ s. In this flow regime, the liquid film is smooth in a short section adjacent to the entrance and wavy in the rest of the domain. The velocity fluctuations in the smooth liquid film were almost negligible. It should also be noted that no external fluctuations have been imposed on the film in order to induce the development of waves.

The appearance and growth of waves on the film surface is caused by the force exerted on the liquid by the gas at the entrance region. In this region, the liquid velocity field and the film thickness vary with their distance from the inlet. Figure 5.44 illustrates the flow behavior of wavy film and the effect of large waves on the gas velocity field. Co-current shear contributes to retarding the interface velocity, which plays a significant role in the wave hydrodynamics.

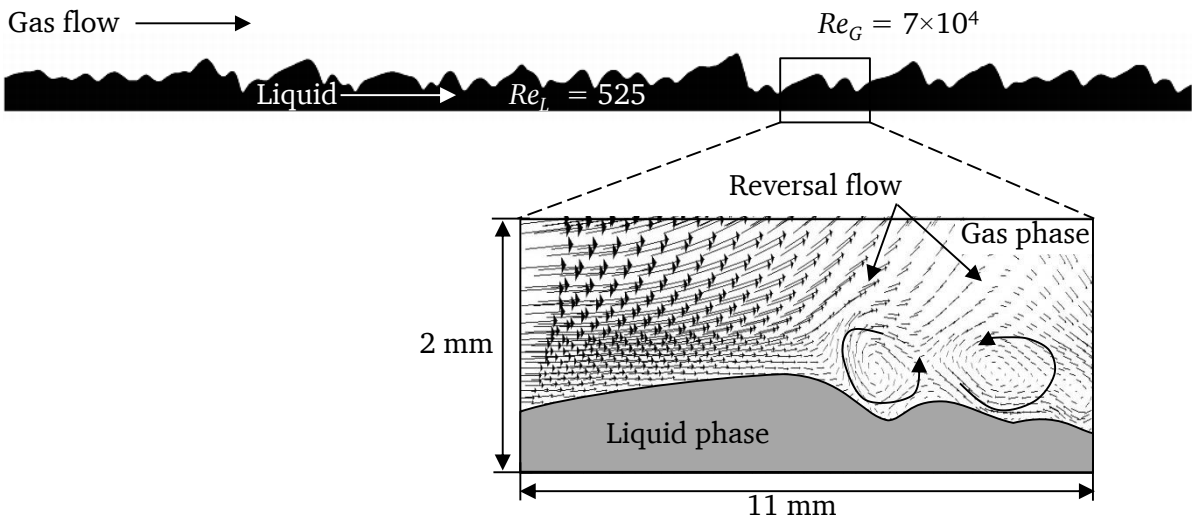

Figure 5.44: Volume fraction contours (top) and velocity vectors(bottom)

The variation of wave amplitudes at the gas-liquid interface is due to the co-current interfacial shear. The computed velocity profiles provide an indication of flow reversal in the liquid film at the capillary region of the wave, and a reduction in film velocity was observed within a region very close to the gas-liquid interface. This indicates that the velocities of the gas and liquid deviate from the parabolic form in some parts of a wavy film region. The waviness has a definite effect on the velocity profiles of the liquid, causing them to deviate from the parabolic form (see Figure 5.46). The velocity vectors indicated by the velocity magnitude in the gas phase are shown in a section (Figure 5.44) including circulation zones preceding a large wave. These recirculation zones affect the heat transfer in the two-phase flow domain.

Temperature field

The film thickness and velocity profile in the film have a significant effect on the temperature distribution in the two-phase flows. The temperature profiles along the y-axis at two different positions are plotted in Figure 5.45, where the reference positions are also indicated. The film thickness values at positions 1 and 2 are 520 and 302 μm, respectively. The first position ($x = 52$ mm) corresponds to the backside of a large wave, while the second position ($x = 58$ mm) corresponds to a circulation zone in the vicinity of a small-amplitude wave (Figure 5.44).

The most consequential effect of the intermediate surface waves is a significant reduction in local film thickness (see Figure 5.43) at the intermediate wave-front region between consecutive solitary waves. In Figure 5.44, the liquid film near the wall approaches its minimum value at the intermediate wave where the film thickness is smallest before growing back to the film height at the solitary capillary wave front upstream. This repeated process is due to the presence of intermediate waves between solitary waves, giving rise to the region of fluctuating wall temperature (see Figure 5.45). The temperature profile differs at both the positions 1 and 2. The wall temperature is about 8 K lower at position-2 (Figure 5.45), which is a clear manifestation of the local intensification of cooling.

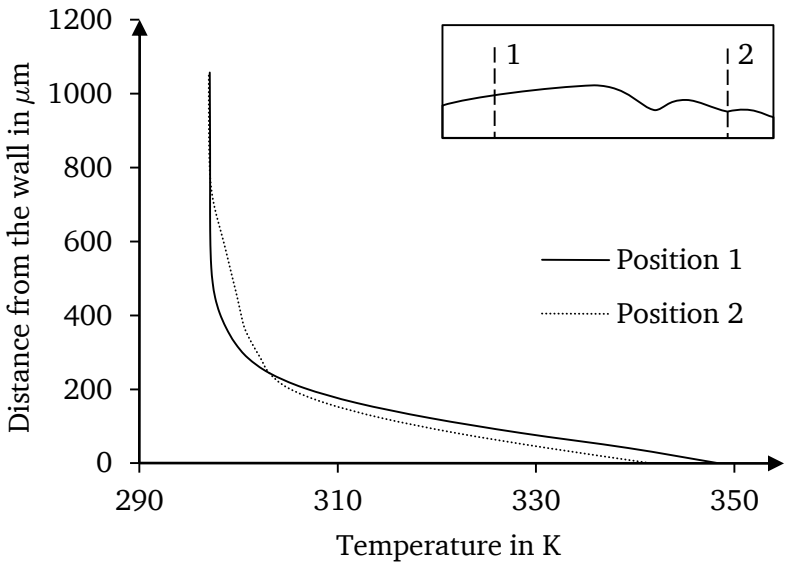

Figure 5.45: Transverse temperature profile at two axial positions

Velocity profile

It is of great interest to study individual velocity profiles directly with the fluctuating gas-liquid interface to further evaluate the effect of waves on the hydrodynamics, and particularly their velocity profiles. In this regard, the film thickness fluctuation and the associated velocity profiles are evaluated in detail. Figure 5.46 illustrates the x velocity profiles at both axial positions, clearly showing an increase in the liquid flow velocity through the wave. The velocity field in the wave region indicates that there is no recirculation in position 1, while a recirculation zone can be seen in position 2 with an amplitude of half of the mean film thickness. Therefore, the local heat transport intensification can be attributed to the additional fluid mixing resulting from the circulation.

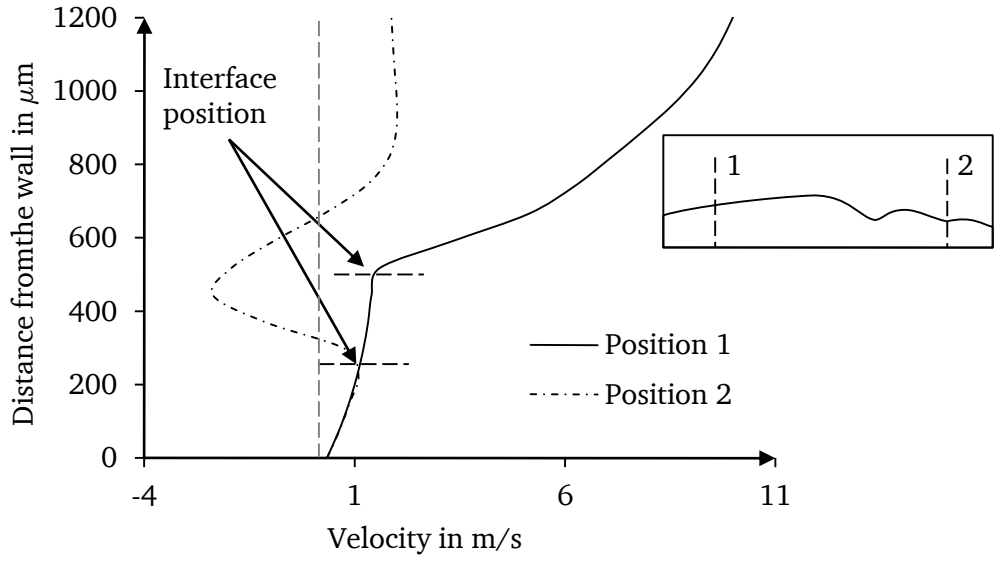

Figure 5.46: Velocity (x-component) profile at two axial positions

The velocity profiles around the wave indicate that the gas flow separates from the downstream side of the wave. This suggests that shear forces on the interfacial waves dominate the heat and momentum transport of liquid films in a co-flowing two-phase flow. These observations clearly demonstrate the viability of simulation techniques for understanding the underlying physics for such a gas-driven liquid films system.

5.5.5 Detailed analysis of the two-phase flows

In this section, simulated interfacial waves at an axial distance from the inlet of heated length are discussed for different gas and liquid Reynolds numbers. Figure 5.47 - Figure 5.49 illustrate the effect of gas velocity on the characteristics of interfacial wavy film for a constant liquid Reynolds number of 525. The gas Reynolds number varies between 10^4 to $7x10^4$, and the wall heat flux is kept constant as 20 W/cm^2. The initial liquid film thickness of 500 μm is maintained at the liquid inlet.

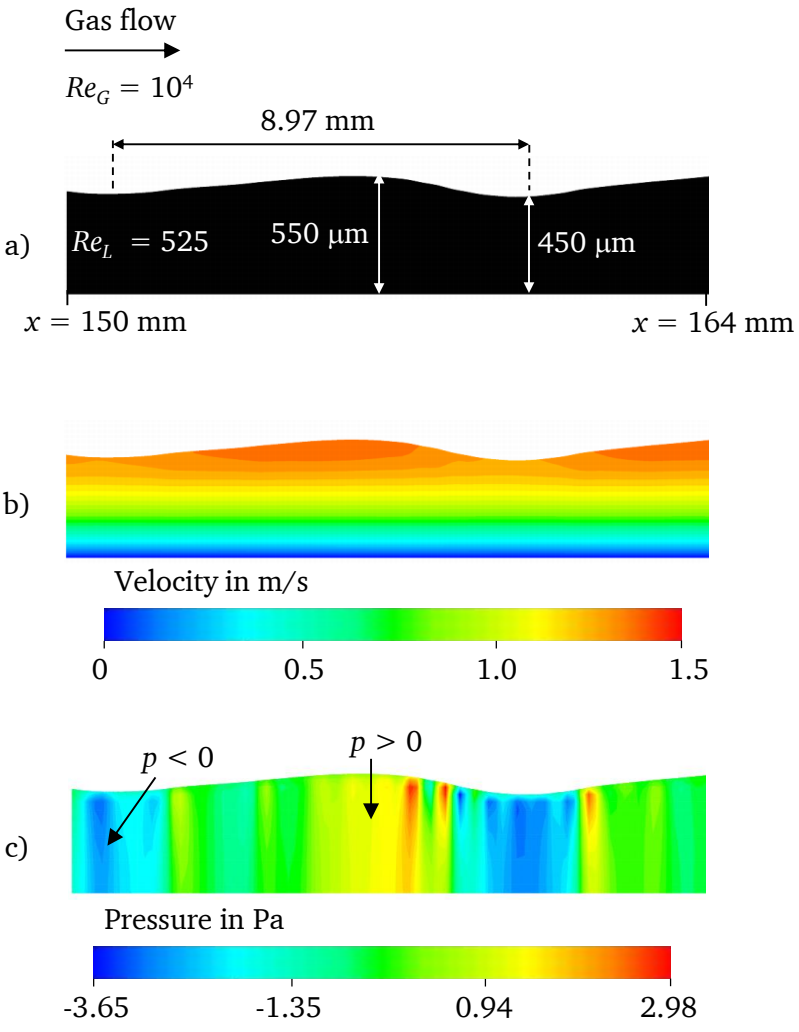

Figure 5.47: a) Liquid film profile b) velocity magnitude distribution c) pressure distribution at $Re_L = 525$ and $Re_G = 10^4$

Figure 5.47 presents a simulated film profile, velocity magnitude distribution, and pressure contours at Re_L = 525 and Re_G = 10^4. The film thickness varies between 550 μm and 450 μm, forming a wave of a length of 8.97 mm. Lower amplitudes of 450 μm and regular pattern waves are noted. It can be seen that the velocity in the film increases with a growing distance from the wall, reaching its maximum value at the peak of the wavy region. The pressure is high in the region of high film thickness and low in the region of low film thickness.

Figure 5.48 shows the wavy liquid film, velocity, and pressure distribution at Re_G = 4x10^4. The wave amplitude rises by increasing the gas velocity. The maximum thickness of 610 μm and minimum thickness of 320 μm are computed in a sinusoidal form of wave. The wave length shortens as the gas velocity increases. This figure shows a similar sequence for a growing sinusoidal wave train where pressure increases at the leading sinusoidal wave's front. Therefore, the downward and upward concavity at the wave crest and the preceding trough give rise to local negative and positive pressure gradients, respectively.

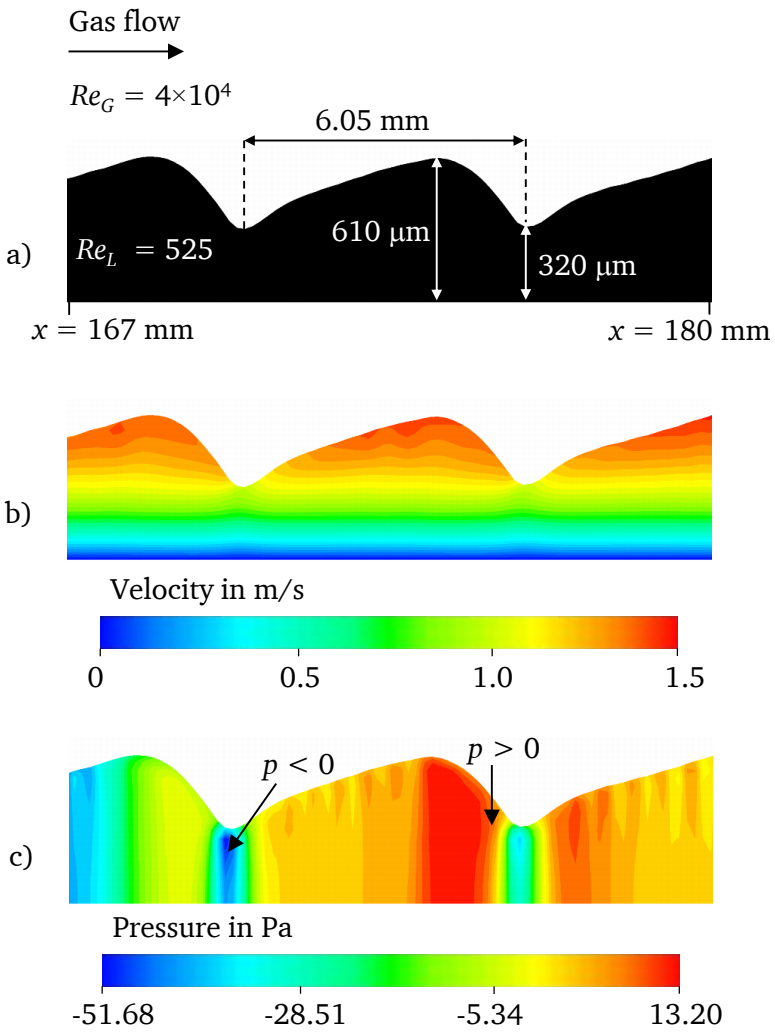

Figure 5.48: a) Liquid film profile b) velocity magnitude distribution c) pressure distribution at Re_L = 525 and Re_G = 4x10^4

The gas shear force influences the interface near the inlet region, and the amplitude of the wave starts growing due to instabilities while forming as a solitary wave in the stream-wise direction.

This solitary wave further develops into small capillary waves. As the solitary capillary waves continue downstream in the flow direction, the preceding capillary waves interact and generate small amplitude waves. These lead to the film thickness reducing at the wave front of the capillary waves; therefore, the overall mean film thickness is reduced. The propagation of the wavy film is due to the effect of viscous forces and surface tension forces.

Figure 5.49 shows the shape of a solitary wave preceded by small capillary ripples, the velocity field, and the pressure distribution at a high gas Reynolds number of $7x10^4$. As expected, an increase in the gas flow rate causes the interface to be subjected to a higher shear force on the liquid film. This shear force leads to a solitary wave forming along the stream-wise distance and capillary waves gradually developing ahead of the wave. The maximum film thickness of the large solitary wave is 739 μm, twice the film thickness of the capillary wave. The number of capillary waves increase as the wave continues downstream. The lowest pressure zone and the minimum thickness are observed in the wave front region (see Figure 5.49). This figure demonstrates that the preceding capillary waves give rise to intermediate waves between consecutive solitary waves. The amplitude of such an intermediate waves is less than that of the capillary waves.

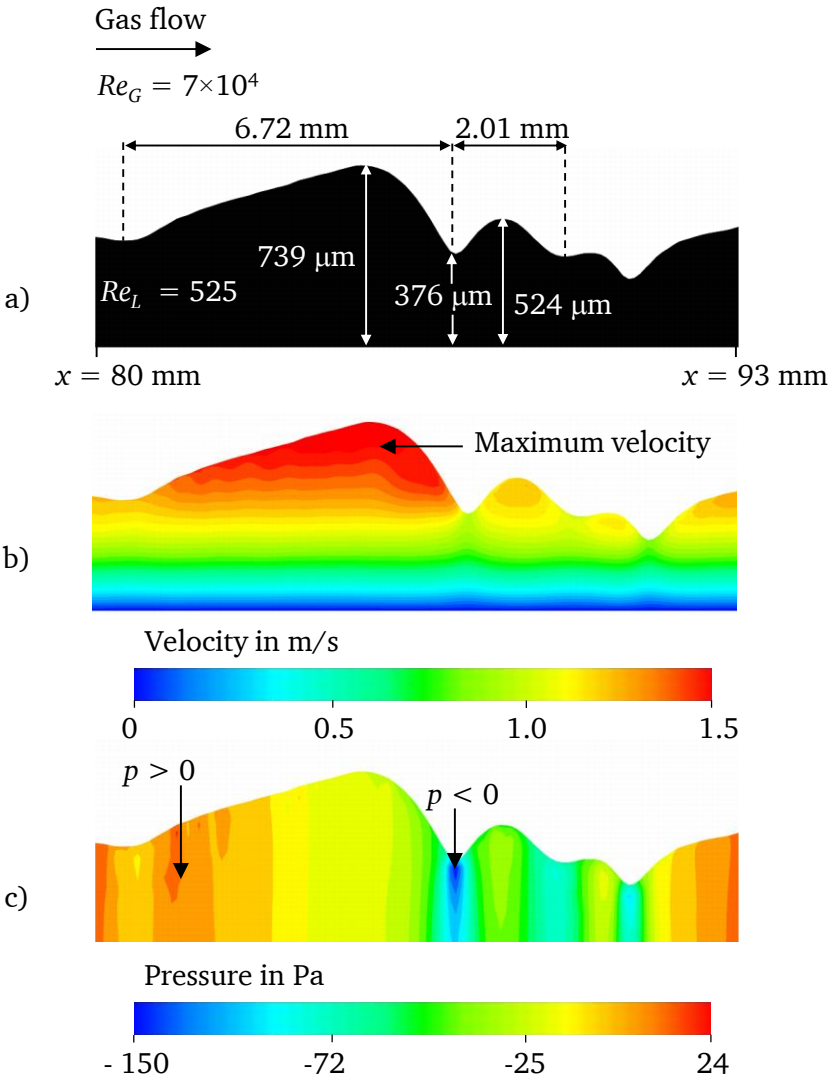

Figure 5.49: a) Liquid film volume fraction b) velocity magnitude distribution c) pressure distribution at $Re_L = 525$ and $Re_G = 7x10^4$

Figure 5.50 illustrates the secondary flow (re-circulation) and the mean velocity field in the gas phase at $Re_L = 525$ and $Re_G = 7\text{x}10^4$. The velocity iso-lines in the gas phase and the velocity distribution of gas phase (upper layer) are presented. The large amplitude waves develop at a higher gas velocity when sliding onto the accelerated wake of their predecessor wave, leading to elongated solitary waves forming. The iso-lines colored by the velocity magnitude help to visualize the flow of the gas around the liquid surface.

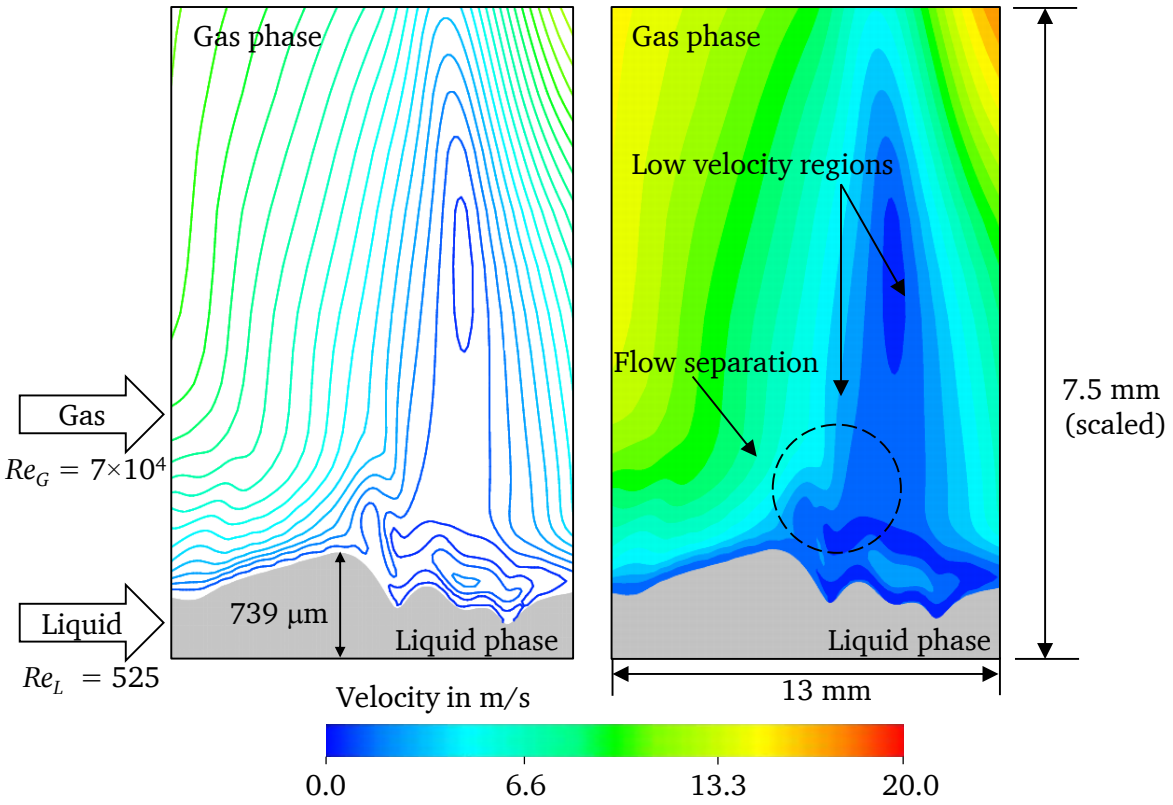

Figure 5.50: Velocity iso-lines (left) and velocity magnitude distribution (right) in the gas phase near the liquid film, showing the evolution of the flow separation for the backflow region (re-circulation zone) at $Re_L = 525$ and $Re_G = 7\text{x}10^4$. The gray color represents the liquid film, and the flow direction is from left to right

The re-circulation in the gas phase presented in Figure 5.50 provides a further insight into the behavior not only of the gas phase but also of the gas–liquid interface. It is observed from the velocity contour plot that the gas phase velocity varies in the middle of the interfacial wave, with the flow separating along the front region (wave trough region with ripples) of the same wave. In addition, the liquid phase acts as an obstacle for the gas phase, forcing the latter to move up towards the upper boundary, resulting in local secondary vortices being generated. Low velocity zones are present in the wave front region because of boundary layer separation effects. This produces a drag force on the interfacial wave in addition to the shear force. The interface is associated with the shape of individual liquid ripples (capillary waves), indicating that drag plays a significant role in the motion of the film. Since the ripples move very slowly ($u_L = 1$ m/s) relative to the air ($u_G > 10$ m/s), the interface could be assumed to exert disturbances on the gas side flow. Figure 5.50 clearly indicates a significant rise in the circulation with an increase of wave

protrusion into the gas boundary layer. As a result, the closed circulation region grows in the transverse direction. With further decreases in the height of the liquid film, the growing closed circulation transforms into a vortex [28]. In particular, the smaller preceding film height induces a more intense open vortex circulation zone at the solitary wave front region. This observation agrees well with previous experimental and numerical investigations by Brauner [19]. Although the result of Figure 5.50 corresponds to flow structures leading to gas backflow for a liquid film with a solitary wave, the same also holds true for sinusoidal waves. Recirculation effects continue downstream in the channel, and accordingly have a strong effect on the temperature field.

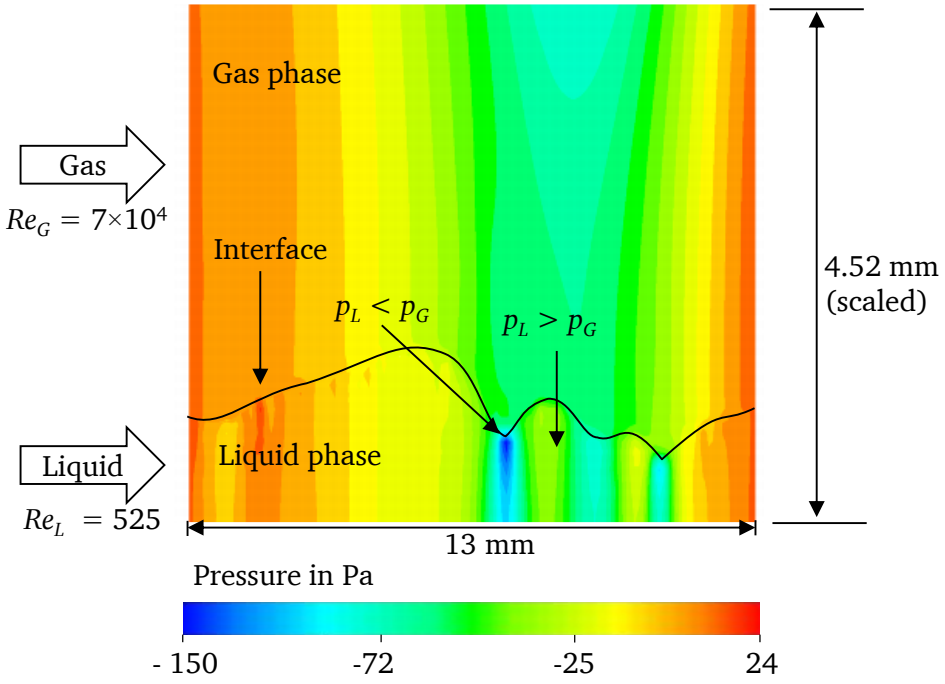

Figure 5.51: Pressure distribution in the gas (upper layer) and liquid phases (lower layer) at $Re_L = 525$ and $Re_G = 7\text{x}10^4$

Figure 5.51 shows the pressure distribution in the liquid film and in a small area surrounding the gas phase. It can be seen that the pressure first decreases in the axial direction continuously before reaching the lowest value in the liquid film at the low amplitude region. Further downstream, the pressure increases where the liquid pressure becomes higher than the gas pressure.

The main driving force in the wavy film is the stream-wise pressure gradient. The pressure in the solitary wave is a time periodic function as the wave progresses downstream. This phenomenon is a result of the interaction between the solitary and its preceding capillary wave. Such an interaction occurs when pressure decreases across the solitary wave front and is followed by an increase in pressure at the preceding capillary wave. The wave front of the capillary wave steepens, thus reducing the height of its preceding trough (see Figure 5.51). A second capillary wave is formed in front of the first capillary wave while the height of the preceding solitary wave increases. This occurs in order to conserve the displaced volume of liquid [28, 29, 78].

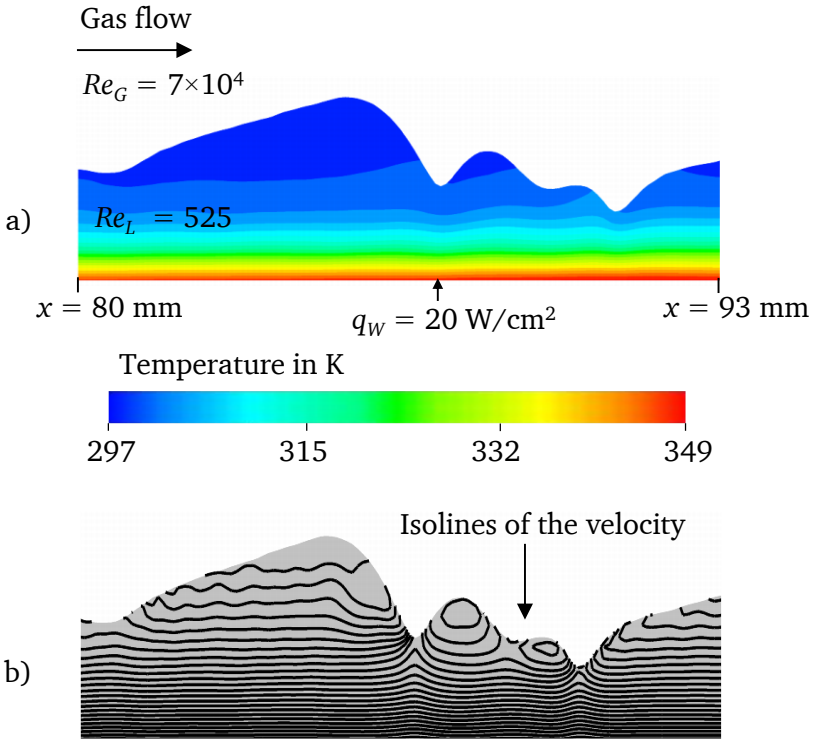

Figure 5.52: a) Temperature distribution and b) velocity iso-lines inside the liquid film at $Re_L = 525$ and $Re_G = 7\text{x}10^4$

Figure 5.52 describes the temperature and the corresponding velocity iso-lines in the wavy region of the liquid film. This figure is an example for the calculated temperature filling the wavy liquid film. The flow pattern for the heat flux of 20 W/cm^2 is shown in Figure 5.52. The fluid in the region near the wall is heated, with the heat flowing from the wall to the liquid. It can be seen that the temperature is higher near the wall and in the trailing part of the wave. The iso-lines of the film velocity field are much more evident for large and small amplitude waves, and an internal vortex can be observed (see Figure 5.52). This vortex in the wave region is responsible for enhancing the heat transfer flux in the trailing edge of the wave. Moreover, Figure 5.52(a) shows that the interface temperature is lowest on the crest of the large amplitude wave and highest on the crest of the smaller wave.

Figure 5.53 depicts the velocity, pressure, and temperature distribution along the interface of the wave. The data is sampled at the interface region to allow analyzing the influence of the waviness and the flow parameters on the heat transfer. In Figure 5.53, velocity, pressure, and temperature profiles are presented as a function of the horizontal position in the x-direction. A sharp increase from 298 K to 303 K on the small capillary wave (at 0.09 mm) is achieved. Simultaneously, at the same position of $x = 0.09$ mm, the velocity and pressure decrease to the minimum. This observation confirms that the waviness of the liquid film causes a strong variation in temperature, which leads to mixing and convection.

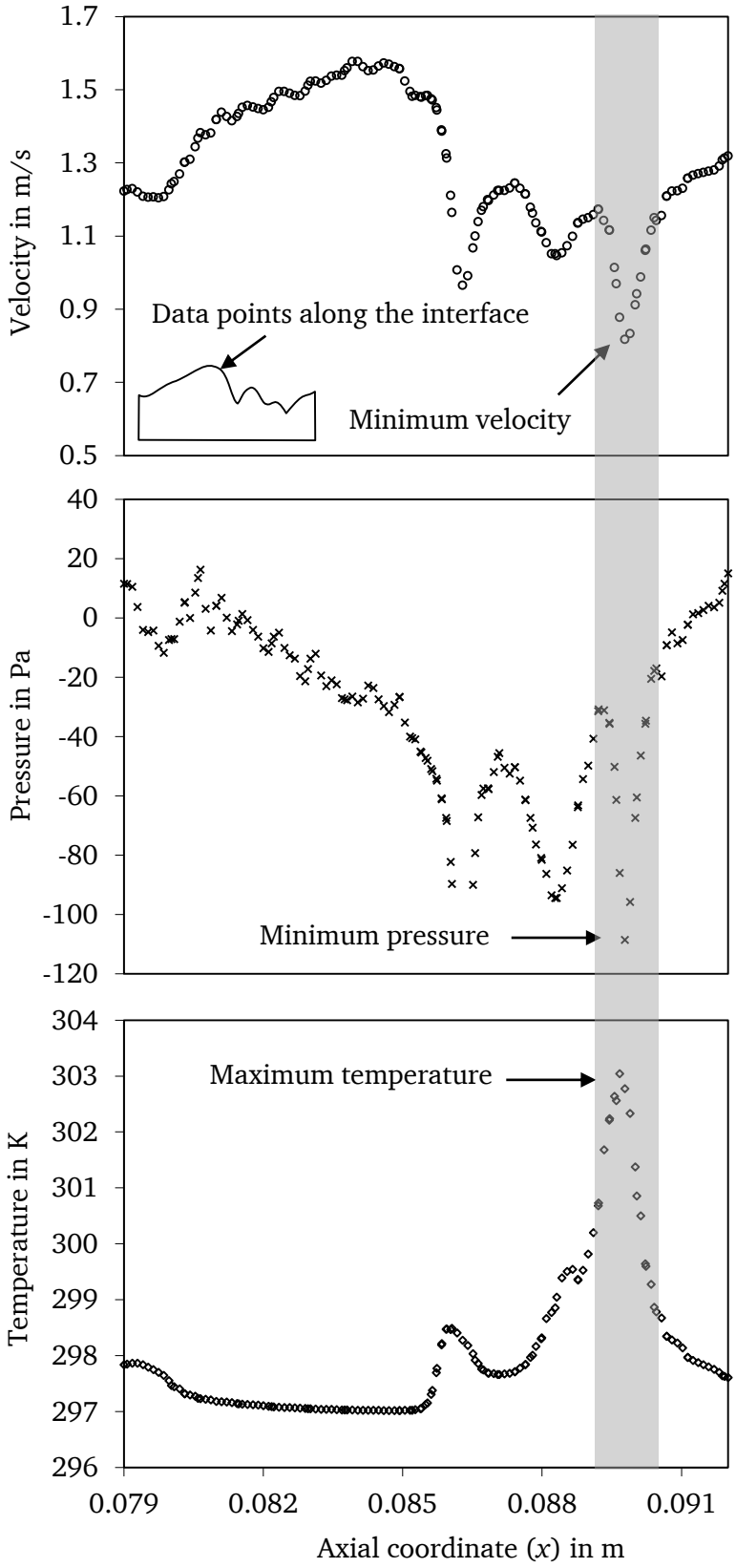

Figure 5.53: Velocity, pressure and temperature distribution along the interface of the wave at $Re_L = 525$ and $Re_G = 7\text{x}10^4$

Figure 5.54 shows the film thickness and shear stress distribution along the interface in the solitary wave. The film thickness h decreases with the interfacial shear τ strengthening, as shown in Figure 5.54. Clearly, the maximum value of the shear stress is located at the trough of the wavy film.

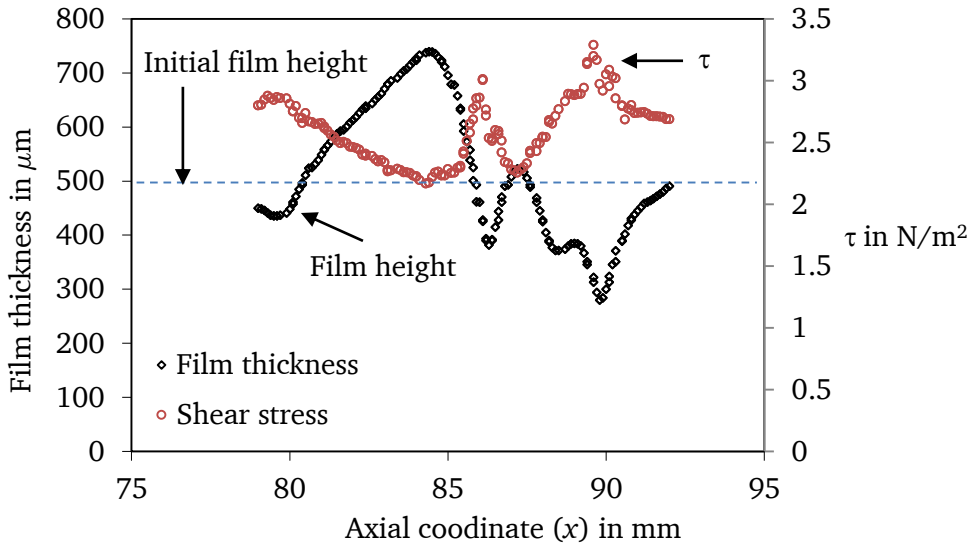

Figure 5.54: Computed liquid film thickness and shear stress distribution along the interface at $Re_L = 525$ and $Re_G = 7\text{x}10^4$

Figure 5.55 presents the liquid film shape, velocity, and pressure distribution inside a liquid film for a higher liquid Reynolds number of 650. At higher liquid flow rates, the film is characterized by consecutive streak-like waves with a high rate of wave interactions, inducing a capillary wave to form. The amplitudes of the large wave and capillary waves vary between 729 μm and 365 μm.

Gas-driven liquid films are found to develop interfacial waves with the effect of the gas shear force. Uniform sinusoidal waves were observed at a low range of gas Reynolds numbers while higher gas velocities resulted in the formation of solitary waves accompanied by capillary ripples. Pressure in the liquid ripples (capillary waves) demonstrate that the motion of liquid films is dominated by drag forces exerted by gas on interfacial disturbances transporting the bulk of the liquid film.

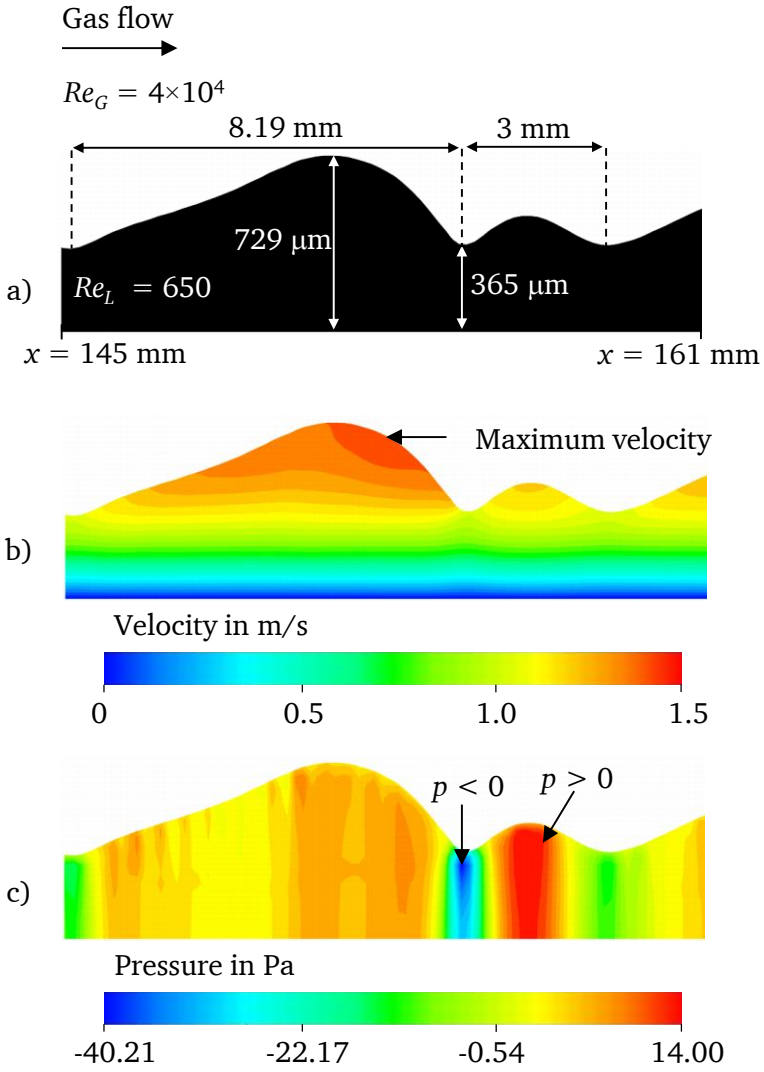

Figure 5.55: a) Liquid film profile b) velocity magnitude distribution c) pressure distribution inside the liquid film at $Re_L = 650$ and $Re_G = 10^4$

5.5.6 Ligaments formation

Figure 5.56 represents the pressure and velocity contours of a gas-liquid flow in a channel with $Re_L = 480$ and $Re_G = 7800$ at various time steps. In Figure 5.56, at 0.137 s, the velocity difference between the gas and the liquid, caused by shearing action by the air and developing into major disturbances, is clearly observed. These disturbances are produced due to the local pressure difference in the flow and lead to the momentum exchange and the formation of large amplitude waves. The liquid becomes highly unstable faster due to the increased gas velocity, causing dramatic changes in the liquid film's hydrodynamic structure. The pressure contours of the liquid film in Figure 5.56 indicate the drag forces exerted by the gas shear on the interface, dominating the momentum of the liquid film [102]. A low static pressure zone is indicated in this figure at 0.137 s, wherefore the wavy film propagates along the stream-wise direction.

Figure 5.56 illustrates the process in which the liquid film disintegrates into the gas phase at the time constant of 0.145 s. The momentum of the gas rises locally leading to unstable ligaments under the action of surface tension. The formation of the ligaments in the stream-wise direction occurs due to the balance of the shear and the surface tension force on the liquid film. The liquid film stretching is due to the shear force exerted by the external shear force in the axial direction. These liquid ligaments break into small drops due to the high relative velocities between the air and the liquid.

The large drops around the rim of the ligament are due to the low relative gas-liquid velocity. The aerodynamic forces resulting from the gas shear are smaller than the inertial and surface tension forces at low velocities, and therefore the ligament disintegrates into droplets. One reason for this detachment of droplets from the ligament rim is the pressure difference (see Figure 5.56). The ligament formation and subsequent detachment of droplets depends on shear forces acting on the liquid film, viscous forces in fluids, and surface tension. At 0.149 s, the ligament breaks up into droplets, and at an increased gas velocity, the droplets are entrained into the recirculation zone (Figure 5.56).

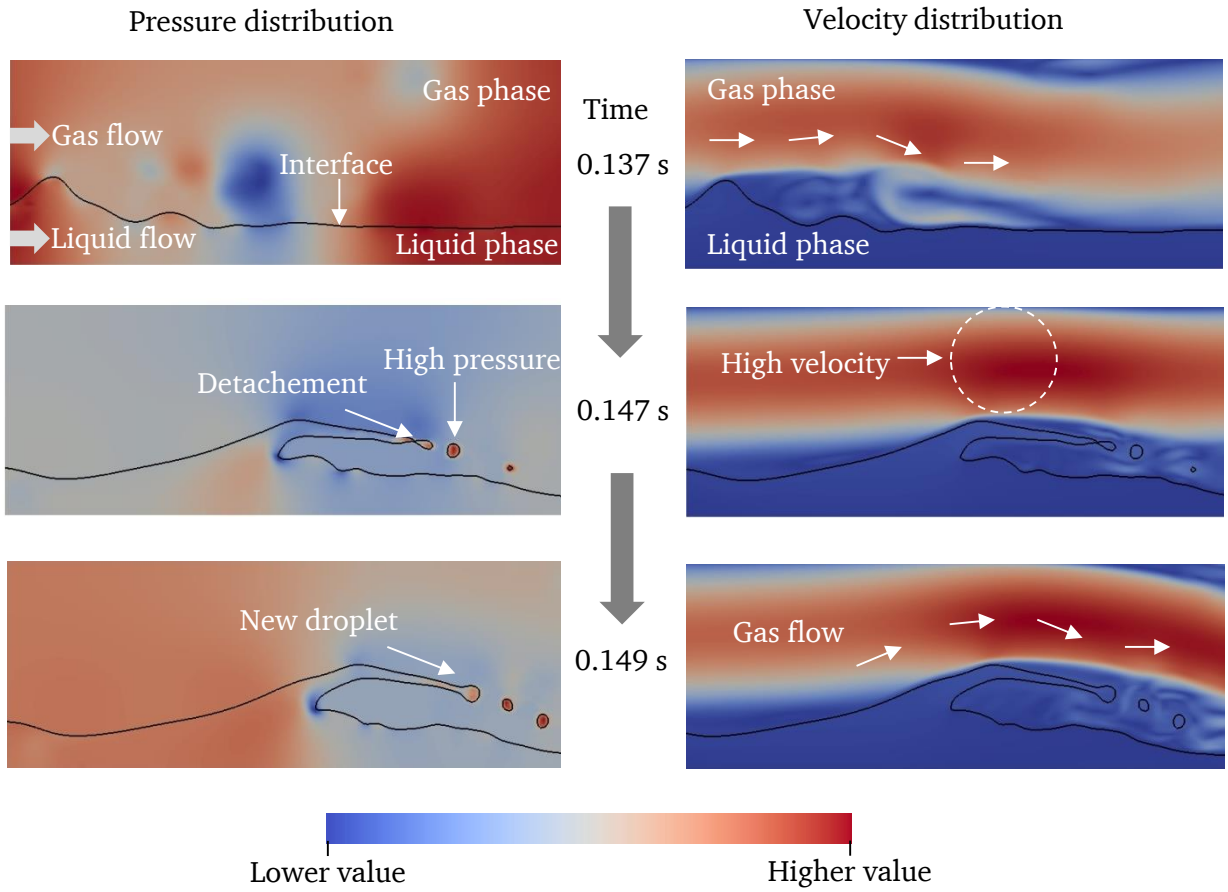

Figure 5.56: Propagation of waves and liquid entrainment in a gas-liquid flow at $Re_L = 480$ and $Re_G = 7800$ at $f = 25$ Hz. Pressure contours (left) and velocity contours (right), the black line indicates interface. The blue color is of lower value, and the red color indicates a higher value

6

Summary and Outlook

This research thesis aimed to describe the numerical work on the processes taking place in LPP chambers for modern gas turbine combustors. The study of gas-driven film flow is essential, since such flows are often encountered in many industrial processes. The scarcity of information on the wall liquid film's hydrodynamics and heat transfer, especially under the effect of turbulent gas flow is responsible for the limited success of the current numerical models. Therefore, a novel numerical methodology is required to study the wave structure, the effect of waves on the hydrodynamics and heat transfer at various flow conditions in gas-driven liquid films. The present study provides a procedure for simulating a convective heat transfer in a wavy liquid film with the effect of turbulent gas on a heated wall.

Summary and conclusions of the work

In the first step, the novel technology was the development of a computational platform in open source code for a liquid film driven by a gas. The numerical study was performed with an open source CFD code written in C++ within OpenFOAM. The procedure consisted of the modification of the open free source code to simulate the heat transfer in two-phase flows. This thesis presented the VOF technique for the numerical solution to study hydrodynamics and the heat transfer of shear-driven flow problems, with high density and viscosity ratios, which are dominant in the direction parallel to the interface. The numerical model was developed using said VOF method to capture the liquid-gas interface. This model was validated by comparing the numerical predictions for two-phase flows with derived analytical data, suggesting the suitable capability of the numerical methodology. The numerical method presented in this thesis was generic and is thus applicable to the study of gas-driven liquid film flows in all industrial applications.

In order to study the heat transfer in two-phase flows, an additional transport equation was implemented in the existing source code, thus modifying the code according to the requirement. Numerical simulations of hydrodynamics and heat transfer in a two-phase stratified water-air flow

along a heated planar wall were performed. The numerical model was validated by comparing it with the semi-analytical model from the literature.

Additionally, the influence of the gas shear on the interfacial processes was studied, and it was shown that the heat transfer was enhanced due to the presence of recirculation zones in the gas phase.

In the second step, three-dimensional simulations were performed to compare the simulation data with the results of the in-house measurements. The agreement between the numerically simulated and the measured data proved reasonable, which was a key result of the numerical investigations. The Low Reynolds number RANS model was employed for the simulation of turbulent gas flow. Furthermore, various flow parameters were varied, and the dynamic behavior of the flow was computed, providing important information on the dynamics of wavy film.

In the third step, a series of CFD simulations for a stratified co-current water-air flow in a straight two-dimensional channel was conducted for a parametric study. The main conclusions of the current work are summarized below:

- The VOF model of a turbulent two-phase flow with heat transfer is capable of not only simulating the movement of a fluid, but also revealing details of the internal processes involved in a two-phase flow.

- Numerical results show that the turbulence-like behavior of a liquid film depends on the degree of waviness and not purely on the liquid Reynolds number. The gas shear force on the liquid film also affects the velocities in the stream direction and intensifies the velocity fluctuations. Moreover, the more fluctuating and larger the interfacial waves are, the greater the fluctuation in velocity leading to a re-circulation in the gas phase. These large amplitude waves modify the flow structure completely in the flow domain. The interfacial shear at high gas Reynolds numbers also promotes interfacial waviness, which contributes significantly to the increased turbulence intensity in the interface region.

- Information on the wave film structure and its variation with the inlet flow conditions as well as the effect of waves on the hydrodynamics are also discussed. It is hypothesized that the gas-liquid interface interaction creates wavy structures contributing to the fluctuations and re-circulation.

- Results show that the wall temperature is influenced by the passage of large waves by increasing the gas and liquid flow rates. Recirculation effects of the surface waves in the interfacial region in the downstream region significantly influence the interfacial heat transfer. Gas Reynolds numbers $Re_G > 10000$ influence the heat transfer and the interfacial waviness. The heat transfer is intensified by increasing the gas and liquid Reynolds numbers. At high gas Reynolds numbers, interfacial wavy film leads to ligament formation, which in turn is dependent on the grid resolution.

- The information regarding the structure of large waves in the turbulent region and the mechanisms governing wave growth and wave interactions at the gas-liquid interface have been successfully investigated. A strong effect of the inlet flow parameters is found for the interfacial wave, as well as flow structures such as velocity profiles and the wave amplitude. The boundary layer develops across the liquid film at low liquid Reynolds numbers, while

in wavy-turbulent film, negative velocities due to the capillary waves lead to local mixing and turbulence at high gas Reynolds numbers.

- At higher gas Reynolds numbers, the film becomes more turbulent and wavy, leading to the occurrence of large disturbance waves. Co-current interfacial shear significantly affects the wave amplitude and liquid film thickness. A disturbance by a shear force of gas on the liquid surface at the inlet changes a smooth film surface into solitary waves with capillary ripples.

Recommendations for future work

The results of the current research demonstrate that the two-phase flow numerical technique is especially useful for studying the flow structures of wavy liquid films influenced by gas shear. The VOF model of turbulent heat transfer two-phase flow has a great potential for further development. In particular, it is desirable to establish a mathematical model that can evaluate turbulent mass transfer between two fluids. Hence, the following set of tasks are recommended for future investigations:

- To predict turbulent air and vapor composition in the evaporating liquid film, accurate evaporative models are required (see Figure 6.1). The formulation of these models could be extended from the modeling approaches developed by Kunkelmann and Stephan [77] (interface re-construction in VOF) as well as Shu [134] (coupled VOF and LS). A systematic extension of this formulation would allow for a mass transfer analysis at the gas-liquid interface.

- The current numerical study does not include the swirl flow of air, which is present in a real LPP vaporizer for modern gas turbine applications. The effect of the swirl on the heat and mass transfer at the gas-liquid interface will be of interest in further research. Liquid fuels are injected into LPP chambers, and therefore, further modeling and simulation of multi-species reaction, including reaction kinetics, is necessary.

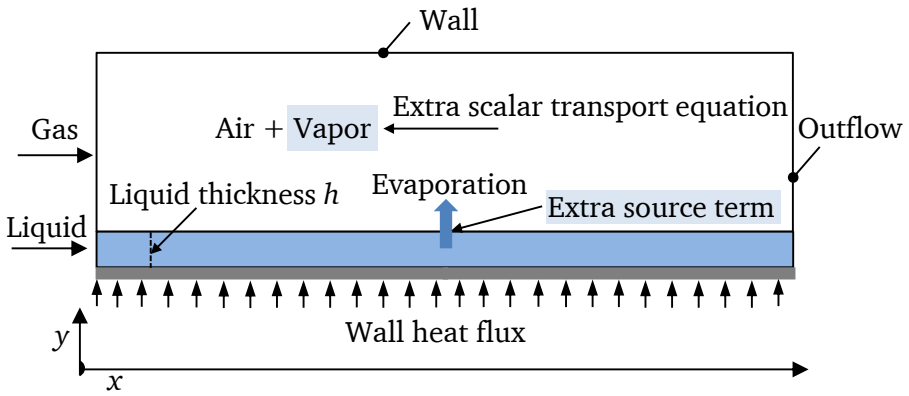

Figure 6.1: Schematic of evaporation model inclusion for future work

Bibliography

[1] P. Adomeit and U. Renz. Hydrodynamics of three-dimensional waves in laminar falling films. *International Journal of Multiphase Flow,* 26:1183-1208, 2000.

[2] M. Aigner and S. Wittig. Swirl and Counterswirl Effects in Prefilming Airblast Atomizers. *Journal of Engineering for Gas Turbines and Power-Transactions of the ASME,* 110:105-110, 1988.

[3] S. V. Alekseenko, V. A. Antipin, D. M. Markovich, and S. M. Kharlamov, An Experimental Study of the Evolution of Three-Dimensional Waves on a Falling Film, in *2nd International Berlin Workshop (IBW2) on Transport Phenomena with Moving Boundaries*, Berlin, Germany, 2003.

[4] P. An, J. Li, and J. D. Jackson. Study of the cooling of a uniformly heated vertical tube by an ascending flow of air and a falling water film. *International Journal of Heat and Fluid Flow,* 20:268-279, 1999.

[5] P. Andreussi, J. C. Asali, and T. J. Hanratty. Initiation of Roll Waves in Gas-Liquid Flows. *AIChE Journal,* 31:119-126, 1985.

[6] N. Andritsos and T. J. Hanratty. Influence of interfacial waves in stratified gas-liquid flows. *AIChE Journal,* 33:444-454, 1987.

[7] N. Ashgriz. *Handbook of Atomization and Sprays: Theory and Applications*, Springer, 2011, ISBN:9781441972644.

[8] A. Bar-Cohen, G. Sherwood, M. Hodes, and G. Solbreken. Gas-assisted evaporative cooling of high density electronic modules. *IEEE Transactions on Components, Packaging, and Manufacturing Technology, Part A,* 18:502-509, 1995.

[9] F. O. Bartz, R. Schmehl, R. Koch, and H. J. Bauer, An extension of dynamic droplet deformation models to secondary atomization, in *23rd European Conference on Liquid Atomization and Spray Systems, ILASS-Europe*, 2010.

[10] L. Bayvel and Z. Orzechowski. *Liquid Atomization (Combustion: An International)*, Taylor & Francis, 1993, ISBN:9780891169598.

[11] D. J. Benson. Computational methods in Lagrangian and Eulerian hydrocodes. *Computer Methods in Applied Mechanics and Engineering,* 99:235-394, 1992.

[12] E. Berberović. *Investigation of Free-surface Flow Associated with Drop Impact: Numerical Simulations and Theoretical Modeling*. Ph.D thesis, Technische Universität Darmstadt, Germany, 2010.

[13] E. Berberović, N. P. van Hinsberg, S. Jakirlić, I. V. Roisman, and C. Tropea. Drop impact onto a liquid layer of finite thickness: Dynamics of the cavity evolution. *Physical Review E,* 79(3):36306, 2009.

[14] R. B. Bird, W. E. Stewart, and E. N. Lightfoot. *Transport Phenomena*. Second edition, Wiley, 2001, ISBN:9780471410775.

[15] F. Birkhold, U. Meingast, P. Wassermann, and O. Deutschmann. *Analysis of the injection of urea-water-solution for automotive SCR DeNOx-systems: modeling of two-phase flow and spray/wall-interaction*. SAE Technical Paper No. 2006-01-0643, 2006.

[16] T. Boeck, J. Li, E. Lopez-Pages, P. Yecko, and S. Zaleski. Ligament formation in sheared liquid-gas layers. *Theoretical and Computational Fluid Dynamics,* 21:59-76, 2007.

[17] J. U. Brackbill, D. B. Kothe, and C. Zemach. A Continuum Method for Modeling Surface-Tension. *Journal of Computational Physics,* 100:335-354, 1992.

[18] H. Brauer. Turbulenz in mehrphasigen Strömungen. *Chemie Ingenieur Technik,* 51:934-948, 1979.

[19] N. Brauner. Modelling of wavy flow in turbulent free falling films. *International Journal of Multiphase Flow,* 15:505-520, 1989.

[20] M. Budakli. *Hydrodynamics and Heat Transfer in Gas-Driven Liquid Film Flows*. Ph.D thesis, Technische Universität Darmstadt, Germany, 2015.

[21] M. Budakli, T. Gambaryan-Roisman, and P. Stephan, Influence of Surface Topography on Heat Transfer in Shear-Driven Liquid Films, in *Journal of Physics: Conference Series 395*, 2012.

[22] G. Cerne, S. Petelin, and I. Tiselj. Coupling of the interface tracking and the two-fluid models for the simulation of incompressible two-phase flow. *Journal of Computational Physics,* 171:776-804, 2001.

[23] K. R. Chun and R. A. Seban. Heat Transfer to Evaporating Liquid Films. *Journal of Heat Transfer,* 93:391-396, 1971.

[24] C. T. Crowe, T. R. Troutt, and J. N. Chung. Numerical Models for Two-Phase Turbulent Flows. *Annual Review of Fluid Mechanics,* 28:11-43, 1996.

[25] J. C. Dallman, J. E. Laurinat, and T. J. Hanratty. Entrainment for horizontal annular gas-liquid flow. *International Journal of Multiphase Flow,* 10:677-689, 1984.

[26] E. J. Davis. Interfacial Shear Measurement for Two-Phase Gas-Liquid Flow by Means of Preston Tubes. *Industrial & Engineering Chemistry Fundamentals,* 8:153-159, 1969.

[27] E. J. Davis. Exact Solutions for a Class of Heat and Mass-Transfer Problems. *Canadian Journal of Chemical Engineering,* 51:562-572, 1973.

[28] G. F. Dietze, F. Al-Sibai, and R. Kneer. Experimental study of flow separation in laminar falling liquid films. *Journal of Fluid Mechanics,* 637:73-104, 2009.

[29] G. F. Dietze, A. Leefken, and R. Kneer. Investigation of the backflow phenomenon in falling liquid films. *Journal of Fluid Mechanics,* 595:435-459, 2008.

[30] J. A. Diez and L. Kondic. Computing three-dimensional thin film flows including contact lines. *Journal of Computational Physics,* 183:274-306, 2002.

[31] A. E. Dukler. The Role of Waves in Two Phase Flow: Some New Understandings. *Chemical Engineering Education,* 11:108-117, 1977.

[32] L. A. Dykhno and T. J. Hanratty. Use of the interchange model to predict entrainment in vertical annular flow. *Chemical Engineering Communications,* 141-142:207-235, 1996.

[33] J. Ebner, P. Schober, O. Schafer, R. Koch, and S. Wittig. Modelling of shear-driven liquid wall films: effect of accelerated air flow on the film flow propagation. *Progress in Computational Fluid Dynamics, an International Journal,* 4:183-190, 2004.

[34] A. Elsäßer, W. Samenfink, J. Ebner, K. Dullenkopf, and S. Wittig, Dynamics of Shear-driven Liquid Films, in *Proceedings of 7th International Conference on Laser Anemometry*, Karlsruhe, 1997.

[35] A. Elsässer, W. Samenfink, J. Ebner, K. Dullenkopf, and S. Wittig. *Effect of Variable Liquid Properties on the Flow Structure within Shear-Driven Wall Films* in *Laser Techniques Applied to Fluid Mechanics*, Springer, Berlin; Heidelberg, 545-564, 2000.

[36] D. Enright, R. Fedkiw, J. Ferziger, and I. Mitchell. A Hybrid Particle Level Set Method for Improved Interface Capturing. *Journal of Computational Physics,* 183:83-116, 2002.

[37] R. P. Fedkiw, T. Aslam, B. Merriman, and S. Osher. A non-oscillatory Eulerian approach to interfaces in multimaterial flows (the ghost fluid method). *Journal of Computational Physics,* 152:457-492, 1999.

[38] J. H. Ferziger and M. Peric . *Computational Methods for Fluid Dynamics*. Third edition, Springer, Berlin; Heidelberg, 2002, ISBN:3540420746.

[39] J. Franz. *Technische Verbrennung*, Springer-Verlag, London, 2007, ISBN:9783540343349.

[40] D. P. Frisk and E. J. Davis. The enhancement of heat transfer by waves in stratified gas-liquid flow. *International Journal of Heat and Mass Transfer,* 15:1537-1552, 1972.

[41] T. Funada, D. D. Joseph, and S. Yamashita. Stability of a liquid jet into incompressible gases and liquids. *International Journal of Multiphase Flow,* 30:1279-1310, 2004.

[42] H. Gao, H.-Y. Gu, and L.-J. Guo. Numerical study of stratified oil–water two-phase turbulent flow in a horizontal tube. *International Journal of Heat and Mass Transfer,* 46:749-754, 2003.

[43] P. H. Gaskell and A. K. C. Lau. Curvature-compensated convective transport: SMART, A new boundedness- preserving transport algorithm. *International Journal for Numerical Methods in Fluids,* 8:617-641, 1988.

[44] E. Y. Gatapova and O. A. Kabov. Shear-driven flows of locally heated liquid films. *International Journal of Heat and Mass Transfer,* 51:4797-4810, 2008.

[45] S. Gepperth, A. Müller, R. Koch, and H. Bauer, Ligament and droplet characteristics in prefilming airblast atomization, in *International Conference on Liquid Atomization and Spray Systems (ICLASS)*, Heidelberg, Germany, 2012.

[46] P. Gokulakrishnan, M. J. Ramotowski, G. Gaines, C. Fuller, R. Joklik, L. D. Eskin*, et al.* A Novel Low NOx Lean, Premixed, and Prevaporized Combustion System for Liquid Fuels. *Journal of Engineering for Gas Turbines and Power,* 130(5):051501, 2008.

[47] V. R. Gopala and B. G. M. van Wachem. Volume of fluid methods for immiscible-fluid and free-surface flows. *Chemical Engineering Journal,* 141:204-221, 2008.

[48] G. Gouesbet, A. Berlemont, and A. Picart. Dispersion of discrete particles by continuous turbulent motions. Extensive discussion of the Tchen' s theory, using a two - parameter family of Lagrangian correlation functions. *Physics of Fluids,* 27:827-837, 1984.

[49] T. J. Hanratty. Separated flow modelling and interfacial transport phenomena. *Applied Scientific Research,* 48:353-390, 1991.

[50] T. J. Hanratty and J. M. Engen. Interaction between a Turbulent Air Stream and a Moving Water Surface. *Aiche Journal,* 3:299-304, 1957.

[51] T. J. Hanratty and A. Hershman. Initiation of roll waves. *AIChE Journal,* 7:488-497, 1961.

[52] F. H. Harlow and J. E. Welch. Numerical Calculation of Time-Dependent Viscous Incompressible Flow of Fluid with Free Surface. *Physics of Fluids,* 8(12):2182, 1965.

[53] A. A. Hashmi, K. Dullenkopf, R. Koch, and H.-J. r. Bauer, CFD methods for shear driven liquid wall films, in *ASME Turbo Expo 2010: Power for Land, Sea, and Air*, Glasgow, UK, 2010.

[54] K. Helbig. *Messung zur Hydrodynamik und zum Wärmetransport bei der Filmverdampfung*. Ph.D thesis, Technische Universität Darmstadt, Germany, 2007.

[55] K. Helbig, A. Alexeev, T. Gambaryan-Roisman, and P. Stephan. Evaporation of Falling and Shear-Driven Thin Films on Smooth and Grooved Surfaces. *Flow, Turbulence and Combustion,* 75:85-104, 2005.

[56] M. Herrmann. Detailed Numerical Simulations of the Primary Atomization of a Turbulent Liquid Jet in Crossflow. *Journal of Engineering for Gas Turbines and Power-Transactions of the ASME,* 132(6):061506, 2010.

[57] M. Hestenes and E. Stiefel. Methods of Conjugate Gradients for Solving Linear Systems. *Journal of Research of the National Bureau of Standards,* 49:409-436, 1952.

[58] G. F. Hewitt and N. S. Hall-Taylor. *Annular Two-phase Flow*, Pergamon, 1970, ISBN:0080157971.

[59] J. Himmelsbach, B. Noll, and S. Wittig. Experimental and Numerical-Studies of Evaporating Wavy Fuel Films in Turbulent Air-Flow. *International Journal of Heat and Mass Transfer,* 37:1217-1226, 1994.

[60] J. O. Hinze. *Turbulence*. Second edition, McGraw-Hill, New York, 1975, ISBN:0070290377.

[61] C. W. Hirt and B. D. Nichols. Volume of Fluid (VOF) Method for the Dynamics of Free Boundaries. *Journal of Computational Physics,* 39:201-225, 1981.

[62] J. M. Hong, T. Shinar, M. J. Kang, and R. Fedkiw. On boundary condition capturing for multiphase interfaces. *Journal of Scientific Computing,* 31:99-125, 2007.

[63] M. Hong, A. Cartellier, and E. Hopfinger, Atomisation and mixing in coaxial injection, in *4th International Conference on Launcher Technology Space Launcher Liquid Propulsion*, 2002.

[64] M. Ishii and M. A. Grolmes. Inception criteria for droplet entrainment in two-phase concurrent film flow. *AIChE Journal,* 21:308-318, 1975.

[65] R. I. Issa. Solution of the implicitly discretised fluid flow equations by operator-splitting. *Journal of Computational Physics,* 62:40-65, 1986.

[66] R. I. Issa, B. Ahmadi-Befrui, K. R. Beshay, and A. D. Gosman. Solution of the implicitly discretised reacting flow equations by operator-splitting. *Journal of Computational Physics,* 93:388-410, 1991.

[67] H. Jasak. *Error analysis and estimation for the finite volume method with applications to fluid flows*. Ph.D thesis, Imperial College, University of London, UK, 1996.

[68] H. Jasak, H. G. Weller, and A. D. Gosman. High resolution NVD differencing scheme for arbitrarily unstructured meshes. *International Journal for Numerical Methods in Fluids,* 31:431-449, 1999.

[69] W. P. Jones and B. E. Launder. Prediction of Laminarization with a 2-Equation Model of Turbulence. *International Journal of Heat and Mass Transfer,* 15:301-314, 1972.

[70] D. D. Joseph, J. Belanger, and G. S. Beavers. Breakup of a liquid drop suddenly exposed to a high-speed airstream. *International Journal of Multiphase Flow,* 25:1263-1303, 1999.

[71] L. A. Jurman, K. Bruno, and M. J. McCready. Periodic and solitary waves on thin, horizontal, gas-sheared liquid films. *International Journal of Multiphase Flow,* 15:371-384, 1989.

[72] L. A. Jurman and M. J. Mccready. Study of Waves on Thin Liquid-Films Sheared by Turbulent Gas-Flows. *Physics of Fluids a-Fluid Dynamics,* 1:522-536, 1989.

[73] O. A. Kabov and E. A. Chinnov. Heat Transfer from a Local Heat Source to Subcooled Liquid Film. *High Temperature,* 39:703-713, 2001.

[74] O. A. Kabov, Y. V. Lyulin, I. V. Marchuk, and D. V. Zaitsev. Locally heated shear-driven liquid films in microchannels and minichannels. *International Journal of Heat and Fluid Flow,* 28:103-112, 2007.

[75] T. Kitagawa, K. Torii, and K. Nishino. Heat transfer of air-water dispersed flow in a vertical pipe. *Heat Transfer - Japanese Research,* 27:255-270, 1998.

[76] S. Kulankara and K. E. Herold. Theory of Heat/Mass Transfer Additives in Absorption Chillers. *HVAC&R Research,* 6:369-380, 2000.

[77] C. Kunkelmann and P. Stephan, Modification and extension of a standard volume-of-fluid solver for simulating boiling heat transfer, in *In Proceedings of the V European Conference on Computational Fluid Dynamics (ECCOMAS CFD2010)*, 2010.

[78] T. Kunugi and C. Kino. DNS of falling film structure and heat transfer via MARS method. *Computers & Structures,* 83:455-462, 2005.

[79] B. Lafaurie, C. Nardone, R. Scardovelli, S. Zaleski, and G. Zanetti. Modeling Merging and Fragmentation in Multiphase Flows with Surfer. *Journal of Computational Physics,* 113:134-147, 1994.

[80] D. Lakehal, M. Meier, and M. Fulgosi. Interface tracking towards the direct simulation of heat and mass transfer in multiphase flows. *International Journal of Heat and Fluid Flow,* 23:242-257, 2002.

[81] C. K. G. Lam and K. Bremhorst. A Modified Form of the k-ε Model for Predicting Wall Turbulence. *Journal of Fluids Engineering,* 103:456-460, 1981.

[82] H. Lan, M. Friedrich, B. F. Armaly, and J. A. Drallmeier. Simulation and measurement of 3D shear-driven thin liquid film flow in a duct. *International Journal of Heat and Fluid Flow,* 29:449-459, 2008.

[83] B. E. Launder. On the Computation of Convective Heat-Transfer in Complex Turbulent Flows. *Journal of Heat Transfer-Transactions of the ASME,* 110:1112-1128, 1988.

[84] B. E. Launder and D. B. Spalding. *Lectures in Mathematical Models of Turbulence*, Academic Press Inc. (Verlag), London; New York, 1972, ISBN:0124380506.

[85] B. E. Launder and D. B. Spalding. The numerical computation of turbulent flows. *Computer Methods in Applied Mechanics and Engineering,* 3:269-289, 1974.

[86] W. Lazik, T. Doerr, S. Bake, R. vd Bank, and L. Rackwitz, Development of lean-burn low-NOx combustion technology at Rolls-Royce Deutschland, in *ASME Turbo Expo 2008: Power for Land, Sea, and Air*, Berlin, Germany, 2008.

[87] A. H. Lefebvre. Airblast Atomization. *Progress in Energy and Combustion Science,* 6:233-261, 1980.

[88] A. H. Lefebvre. *Atomization and Sprays*, Hemisphere Pub. Corp., New York, 1989, ISBN:0891166033.

[89] A. H. Lefebvre. Twin-Fluid Atomization: Factors Influencing Mean Drop Size. *Atomization and Sprays,* 2:101-119, 1992.

[90] B. P. Leonard. A stable and accurate convective modelling procedure based on quadratic upstream interpolation. *Computer Methods in Applied Mechanics and Engineering,* 19:59-98, 1979.

[91] S. Leuthner. Messungen und Modellierungen zum Energie-und Stofftransport in Fallfilmen. *Fortschritt Berichte-VDI Reihe 3 Verfahrenstechnik,* 1999.

[92] P. A. Libby. *An Introduction To Turbulence*, Taylor & Francis, New York, 1996, ISBN:9781560321002.

[93] A. Lozano, F. Barreras, G. Hauke, and C. Dopazo. Longitudinal instabilities in an air-blasted liquid sheet. *Journal of Fluid Mechanics,* 437:143-173, 2001.

[94] A. Malhotra and S. S. Kang. Turbulent Prandtl Number in Circular Pipes. *International Journal of Heat and Mass Transfer,* 27:2158-2161, 1984.

[95] J. R. Marati, M. Budakli, T. Gambaryan-Roisman, and P. Stephan, Numerical and experimental investigation on shear-driven thin liquid film flows, in *Proceedings of the 6th International Berlin Workshop – IBW6 on Transport Phenomena with Moving Boundaries*, Berlin, Germany, 3:313-329, 2011.

[96] J. R. Marati, M. Budakli, T. Gambaryan-Roisman, and P. Stephan. Heat Transfer in Shear-Driven Thin Liquid Film Flows. *Computational Thermal Sciences,* 5:303-315, 2013.

[97] F. Mashayek and R. V. R. Pandya. Analytical description of particle/droplet-laden turbulent flows. *Progress in Energy and Combustion Science,* 29:329-378, 2003.

[98] S. Mckee, M. F. Tome, V. G. Ferreira, J. A. Cuminato, A. Castelo, F. S. Sousa*, et al.* The MAC method. *Computers & Fluids,* 37:907-930, 2008.

[99] T. Menard, S. Tanguy, and A. Berlemont. Coupling level set/VOF/ghost fluid methods: Validation and application to 3D simulation of the primary break-up of a liquid jet. *International Journal of Multiphase Flow,* 33:510-524, 2007.

[100] M. Miya, D. E. Woodmansee, and T. J. Hanratty. A model for roll waves in gas-liquid flow. *Chemical Engineering Science,* 26:1915-1931, 1971.

[101] A. Miyara. Numerical analysis on flow dynamics and heat transfer of falling liquid films with interfacial waves. *Heat and Mass Transfer,* 35:298-306, 1999.

[102] I. Mudawwar. Interfacial instabilities of air-driven liquid films. *International Communications in Heat and Mass Transfer,* 13:535-543, 1986.

[103] A. Müller, K. Dullenkopf, and H. J. Bauer, Application of an extended particle tracking method to analyze droplet wall interaction, in *14th international symposium on applications of laser techniques to fluid mechanics*, Lisbon, Portugal, 2008.

[104] M. Müller. Fast and robust tracking of fluid surfaces. in *Proceedings of the 2009 ACM SIGGRAPH/Eurographics Symposium on Computer Animation,* New Orleans, Louisiana, 2009.

[105] W. Nusselt. Die Oberflachen-Kondensation des Wasserdampfes. 2. *Verein. Deutsch. Ing,* 60:541-569, 1916.

[106] OpenCFD Ltd. http://www.opencfd.co.uk [Online].

[107] S. Osher and R. P. Fedkiw. Level Set Methods: An Overview and Some Recent Results. *Journal of Computational Physics,* 169:463-502, 2001.

[108] S. Osher and J. A. Sethian. Fronts Propagating with Curvature-Dependent Speed - Algorithms Based on Hamilton-Jacobi Formulations. *Journal of Computational Physics,* 79:12-49, 1988.

[109] M. G. Pai, O. Desjardins, and H. Pitsch. Detailed simulations of primary breakup of turbulent liquid jets in crossflow. *Center for Turbulence Research, Annual Research Briefs,* 451-466, 2008.

[110] L. Pan and T. J. Hanratty. Correlation of entrainment for annular flow in vertical pipes. *International Journal of Multiphase Flow,* 28:363-384, 2002.

[111] S. Patankar. *Numerical Heat Transfer and Fluid Flow*, Taylor & Francis, 1980, ISBN:9780891165224.

[112] V. C. Patel, W. Rodi, and G. Scheuerer. Turbulence Models for near-Wall and Low Reynolds-Number Flows - a Review. *AIAA Journal,* 23:1308-1319, 1985.

[113] C. A. Peng, L. A. Jurman, and M. J. McCready. Formation of solitary waves on gas-sheared liquid layers. *International Journal of Multiphase Flow,* 17:767-782, 1991.

[114] A. Plimon. Velocity Profiles in Shear Force Driven Wall Films. *Experiments in Fluids,* 11:339-340, 1991.

[115] S. B. Pope. *Turbulent Flows*, Cambridge University Press, Cambridge; New York, 2000, ISBN:0521591252.

[116] W. J. Rider and D. B. Kothe. Reconstructing volume tracking. *Journal of Computational Physics,* 141:112-152, 1998.

[117] W. Rodi. *Turbulent models and their application in hydraulics - a state of the art review*. Habilitation thesis Habilitation thesis, University of Karlsruhe, Germany, 1980.

[118] W. Rodi and N. N. Mansour. Low-Reynolds-Number Kappa-Epsilon Modeling with the Aid of Direct Simulation Data. *Journal of Fluid Mechanics,* 250:509-529, 1993.

[119] H. Rosskamp, A. Elsäßer, W. Samenfink, J. Meisl, M. Willmann, and S. Wittig, An enhanced model for predicting the heat transfer to wavy shear-driven liquid wall films, in *Third International Conference on Multiphase Flow, ICMF*, 98:8-12, 1998.

[120] H. Rosskamp, M. Willmann, and S. Wittig. Heat up and evaporation of shear driven liquid wall films in hot turbulent air flow. *International Journal of Heat and Fluid Flow,* 19:167-172, 1998.

[121] K. Rup and M. Soczówka. An improved low Reynolds number k-ε model for heat transfer calculations. *Forschung im Ingenieurwesen,* 65:225-235, 2000.

[122] H. Rusche. *Computational Fluid Dynamics of Dispersed {Two-Phase} Flows at High Phase Fractions*. Ph.D thesis, Imperial College, University of London, UK, 2002.

[123] W. Samenfink, A. Elsäßer, S. Wittig, and K. Dullenkopf, Internal Transport Mechanisms of Shear-Driven Liquid Films, in *Proceedings of the Eighth International Symposium on Applications of Laser Techniques to Fluid Mechanics*, 8-11, 1996.

[124] T. Sattelmayer, K. H. Sill, and S. Wittig. Nonintrusive Optical Measurement Technique for Wavy Liquid-Films - Determination of Film Thickness and Wave Structure. *Technisches Messen,* 54:155-160, 1987.

[125] T. Sattelmayer and S. Wittig. Internal Flow Effects in Prefilming Airblast Atomizers - Mechanisms of Atomization and Droplet Spectra. *Journal of Engineering for Gas Turbines and Power-Transactions of the Asme,* 108:465-472, 1986.

[126] R. Scardovelli and S. Zaleski. Direct numerical simulation of free-surface and interfacial flow. *Annual Review of Fluid Mechanics,* 31:567-603, 1999.

[127] R. Schmehl, H. Rosskamp, M. Willmann, and S. Wittig. CFD analysis of spray propagation and evaporation including wall film formation and spray/film interactions. *International Journal of Heat and Fluid Flow,* 20:520-529, 1999.

[128] P. Schober. *Berührungsfreie Erfassung beschleunigter schubspannungsgetriebener Kraftstoffwandfilme unter Druckeinfluss*, Logos-Verlag, 2009, ISBN:9783832522810.

[129] P. Schober, J. Ebner, O. Schäfer, and S. Wittig, Experimental study on the effect of a strong negative pressure gradient on a shear-driven liquid fuel film, in *Proceedings of 9th ICLASS*, Sorrento, Italy, 2003.

[130] J. A. Sethian. *Level Set Methods and Fast Marching Methods: Evolving interfaces in computational geometry, fluid mechanics, computer vision, and materials science*. Second revised edition, Cambridge university press, 1999, ISBN:0521645573.

[131] J. A. Sethian. Evolution, implementation, and application of level set and fast marching methods for advancing fronts. *Journal of Computational Physics,* 169:503-555, 2001.

[132] J. A. Sethian and P. Smereka. Level set methods for fluid interfaces. *Annual Review of Fluid Mechanics,* 35:341-372, 2003.

[133] J. A. Shmerler and I. Mudawar. Local Heat-Transfer Coefficient in Wavy Free-Falling Turbulent Liquid-Films Undergoing Uniform Sensible Heating. *International Journal of Heat and Mass Transfer,* 31:67-77, 1988.

[134] B. Shu. *Numerische Simulation des Blasensieden mit Volume-Of-Fluid- und Level-Set-Methode*. Ph.D thesis, Technische Universität Darmstadt, Germany, 2009.

[135] D. W. Stanton and C. J. Rutland. Multi-dimensional modeling of thin liquid films and spray wall interactions resulting from impinging sprays. *International Journal of Heat and Mass Transfer,* 41:3037-3054, 1998.

[136] M. Sussman and E. G. Puckett. A coupled level set and volume-of-fluid method for computing 3D and axisymmetric incompressible two-phase flows. *Journal of Computational Physics,* 162:301-337, 2000.

[137] M. Sussman, P. Smereka, and S. Osher. A Level Set Approach for Computing Solutions to Incompressible 2-Phase Flow. *Journal of Computational Physics,* 114:146-159, 1994.

[138] M. Sussman, K. M. Smith, M. Y. Hussaini, M. Ohta, and R. Zhi-Wei. A sharp interface method for incompressible two-phase flows. *Journal of Computational Physics,* 221:469-505, 2007.

[139] G. Tryggvason, R. Scardovelli, and S. Zaleski. *Direct Numerical Simulations of Gas–Liquid Multiphase Flows*, Cambridge University Press, 2011, ISBN:0521782406.

[140] D. Turney and S. Banerjee. Transport phenomena at interfaces between turbulent fluids. *AIChE Journal,* 54:344-349, 2008.

[141] O. Ubbink. *Numerical prediction of two fluid systems with sharp interfaces*. Ph.D thesis, Imperial College, University of London, 1997.

[142] O. Ubbink and R. I. Issa. A method for capturing sharp fluid interfaces on arbitrary meshes. *Journal of Computational Physics,* 153:26-50, 1999.

[143] P. Valluri, L. Ó. Naraigh, H. Ding, and P. D. M. Spelt. Linear and nonlinear spatio-temporal instability in laminar two-layer flows. *Journal of Fluid Mechanics,* 656:458-480, 2010.

[144] P. Valluri, P. D. M. Spelt, C. J. Lawrence, and G. F. Hewitt. Numerical simulation of the onset of slug initiation in laminar horizontal channel flow. *International Journal of Multiphase Flow,* 34:206-225, 2008.

[145] S. P. van der Pijl, A. Segal, C. Vuik, and P. Wesseling. A mass-conserving Level-Set method for modelling of multi-phase flows. *International Journal for Numerical Methods in Fluids,* 47:339-361, 2005.

[146] H. van der Vorst. Bi-CGSTAB: A Fast and Smoothly Converging Variant of Bi-CG for the Solution of Nonsymmetric Linear Systems. *SIAM Journal on Scientific and Statistical Computing,* 13:631-644, 1992.

[147] C. M. Varga, J. C. Lasheras, and E. J. Hopfinger. Initial breakup of a small-diameter liquid jet by a high-speed gas stream. *Journal of Fluid Mechanics,* 497:405-434, 2003.

[148] H. K. Versteeg and W. Malalasekera. *An introduction to Computational Fluid Dynamics: The finite volume method*. Second edition, Pearson Education Ltd., England; New York, 2007, ISBN:9780131274983.

[149] T. Waclawczyk and T. Koronowicz. Comparison of CICSAM and HRIC high-resolution schemes for interface capturing. *Journal of Theoretical and Applied Mechanics,* 46:325-345, 2008.

[150] X. L. Wang, C. J. Liu, X. G. Yuan, and K. T. Yu. Computational fluid dynamics simulation of three-dimensional liquid flow and mass transfer on distillation column trays. *Industrial & Engineering Chemistry Research,* 43:2556-2567, 2004.

[151] F. M. White. *Fluid Mechanics*. Fourth edition, McGraw-Hill, 1999, ISBN:9780070697164.

[152] D. C. Wilcox. *Turbulence Modeling for CFD*. Third edition, DCW Industries, California, 2006, ISBN:9781928729082.

[153] S. Wittig, A. Elsäßer, W. Samenfink, J. Ebner, and K. Dullenkopf. Velocity profiles in shear-driven liquid films: LDV-measurements. *8th International Symposium on Applications of Laser Techniques to Fluid Mechanics,* 6-11, 1996.

[154] S. Wittig, J. Himmelsbach, B. Noll, H. J. Feld, and W. Samenfink. Motion and Evaporation of Shear-Driven Liquid Films in Turbulent Gases. *Journal of Engineering for Gas Turbines and Power,* 114:395-400, 1992.

[155] P. Yecko and S. Zaleski. Transient growth in two-phase mixing layers. *Journal of Fluid Mechanics,* 528:43-52, 2005.

[156] C.-S. Yih. Instability due to viscosity stratification. *Journal of Fluid Mechanics,* 27:337-352, 1967.

Appendix

MATLAB Code

The following MATLAB code to compute liquid film height and velocity profile:

```
%%%%%%%%%%%%%%%%%%%%%%%%%%%%%%%%%%%%%%%%%%%%%%%%%%%%%%%%
function Velocity_Profile
clc
format long
H=0.002; % height of the channel

ReL=8.5;muL=0.001;roL=998;mL=ReL*muL; % water inlet and fluid properties
ReG=534;muG=0.000018;roG=1.23;mG=ReG*muG; % air inlet and fluid properties

% for finding h
function y=Eq(h)
C=((H^2-h^2)*muL+h^2*muG)/((H-h)*muL+h*muG);
M=((H)^3)/3-H^3-(C*(H)^2)/2+C*H^2-(h^3)/3+h*H^2+(C*h^2)/2-C*H*h;
y=(6*(M)/(2*h^3-3*(C)*h^2))-((mG*muG*roL)/(roG*mL*muL));
end
h=fzero(@Eq,.000000001)

%  for finding C and M
C=((H^2-h^2)*muL+h^2*muG)/((H-h)*muL+h*muG);
M=((H)^3)/3-H^3-(C*(H)^2)/2+C*H^2-(h^3)/3+h*H^2+(C*h^2)/2-C*H*h;

dpdxL=12*mL*muL/(roL*(2*h^3-3*C*h^2)) %liquid pressure gradient
dpdxG=2*mG*muG/(roG*M) % gas pressure gradient
%  for plotting graph
y=0:0.0000001:H;
Ug=(mG/(roG*M))*(y.^2-H.^2-C.*(y-H));
Ul=(6*mL/(roL.*(2.*h.^3-3.*C.*h.^2))).*(y.^2-C.*y);
U=Ul.*(y<=h)+Ug.*(y>h);
g=plot(U,y);
xlabel('Velocity (m/s)');ylabel('Inlet (m)');

%%%%%%%%%%%%%%%%%%%%%%%%%%%%%%%%%%%%%%%%%%%%%%%%%%%%%%%%
```

Papers and Poster Publications

Journal and conference papers

J. R. Marati, M. Budakli, T. Gambaryan-Roisman and P. Stephan. Heat transfer in shear-driven thin liquid film flows. *Computational Thermal Sciences,* 5:303-315, 2013.
DOI: 10.1615/ComputThermalScien.2013006073

P. Stephan, T. Gambaryan-Roisman, M. Budakli and **J. R. Marati**. Experimental and numerical investigation of shear-driven film flow and film evaporation. *Flow and Combustion in Advanced Gas Turbine Combustors, Series of fluid mechanics and its applications*, 102:29-54, 2013.

J. R. Marati, M. Budakli, T. Gambaryan-Roisman and P. Stephan. Heat transfer in shear-driven thin liquid film flow*, in Proceedings of CHT-12, ICHMT International Symposium on Advances in Computational Heat Transfer*, Bath, England, 2012.
http://www.dl.begellhouse.com/jp/references/1bb331655c289a0a,636c91ea5ddcad95,14d685a863d6b410.html

J. R. Marati, M. Budakli, T. Gambaryan-Roisman and P. Stephan. Numerical and experimental investigation on shear-driven thin liquid film flows, in *Proceedings of the 6th International Berlin Workshop-IBW6 on Transport Phenomena with Moving Boundaries*, Berlin, Germany, 3:313-329, 2011.

Poster presentations

J. R. Marati, M. Budakli, T. Gambaryan-Roisman, P. Stephan. *7th International OpenFOAM Workshop-2012*, Darmstadt. June 25-28, 2012.

M. Budakli, **J. R. Marati**, T. Gambaryan-Roisman, P. Stephan. Experimentelle und numerische Untersuchung der Hydrodynamik und der Wärmeübertragung von scherkraftgetriebenen Flüssigkeitsfilmen auf beheizten Wänden, *Jahrestreffen der Fachgruppe Wärme- und Stoffübertragung*, Weimar. 2012.

M. Budakli, **J. R. Marati**, T. Gambaryan-Roisman, P. Stephan. *International Workshop on 'Near Wall Reactive Flows' organized by Collaborative Research Center SFB568 "Flow and Combustion in the Future Gas Turbine Combustion Chambers*. November 18-19, 2010.